Copper complexes of polyazacryptands.

Thesis

UNRESTRICTED

COPPER COMPLEXES OF POLYAZACRYPTANDS

A Thesis

By

QIN LU

Submitted to the Research Degree Center of

The Open University

for the degree of

Doctor of Philosophy

May 1999

Major Subject: Inorganic Chemistry

DATE OF SUBMISSION: 20 APRIL 1999
DATE OF AWARD: 25 AUGUST 1999

ProQuest LLC.
789 East Eisenhower Parkway
P.O. Box 1346
Ann Arbor, MI 48106 – 1346

ABSTRACT

Dicopper complexes of **L1-L5**, which are obtained from [2+3] condensation of tris-(2-aminoethyl)amine with a series of dialdehydes, have been synthesized. X-ray structure determination has been carried on $[Cu_2\mathbf{L1}][O_3SCF_3]_2$, $[Cu_2\mathbf{L2}][BF_4]_2$, $[Cu_2\mathbf{L4}][ClO_4]_2$, and $[Cu_2(\mathbf{L5\text{-}3H})]ClO_4$. ^1H NMR spectra of dicopper(I) complexes of **L1-L5** indicate that all the ligands adopt a convergent conformation upon encapsulating a pair of Cu(I) ions. Cyclic voltammetry studies reveal that dicopper(I) complexes in this series are stable either thermodynamically or kinetically under aerobic conditions. Dicopper(II) complexes are hydrolytically sensitive and ring-opening reactions occur followed by the hydrolytic attack on the imino C=N double bond(s).

Octaamino cryptands **RL1-RL5** have been synthesized through hydrogenation of **L1-L5** with $NaBH_4$. They are good hosts for a pair of Cu(II) ions whereas their dicopper(I) complexes are air-sensitive. Three type of bridging ligands, OH^-, im^-, and N_3^-, are incorporated into the dicopper(II) cryptates and their structural, spectroscopic, and magnetic properties have been investigated. Variable temperature magnetic susceptibility studies combined with X-ray crystallography and EPR spectroscopy demonstrate the effect of unusually large bridge angle, such as collinear Cu-O(H)-Cu or Cu-N=N=N-Cu linkage, on the magnetic exchange between the two Cu(II) ions in the bridged dicopper(II) cryptates.

ACKNOWLEDGMENTS

I would like to thank my supervisor, Dr. J. Nelson, for providing me the opportunity to pursue this research project, and for her great advice, encouragement and understanding throughout the project.

I am deeply grateful to Dr. C. J. Harding for his help in magnetic studies and his hospitality during my stay in Milton Keynes; to Drs. V. McKee, M. G. B. Drew, and J. F. Malone for solving the crystal structures.

I thank the School of Chemistry at Queen University of Belfast for the technical assistance from its staff and for letting me use the facilities.

I so appreciate my friendship with Drs. G. Morgan, D. J. Marrs and N. Martin, and many others at Queen's. They made my two-year stay in Belfast a very pleasant experience.

Dearest thanks to my mother and father and sister, for their unconditional love, and support throughout my life.

CONTENTS

LIST OF FIGURES

system (tetragonal) in the absorptive and first-derivative form, (c) is the first-derivative form for a rhombic system.

Figure A6.3 Hyperfine splitting of the $m_s = -1/2 \rightarrow +1/2$ transition due to interaction with nuclear spin I = 3/2. The four resulting transitions are equally spaced.

CHAPTER 1 INTRODUCTION

1.1 The general chemistry of copper[1]

Copper is widely distributed in nature as the metal, in sulfides, arsenides, chlorides, carbonates, and so on. Copper has a single electron outside the filled 3*d* shell but has essentially nothing in common with the alkalis except formal stoichiometries in the +1 oxidation state. The filled *d* shell is much less effective than is a noble gas shell in shielding the *s* electron from the nuclear charge, so that the first ionization enthalpy of Cu is higher than those of the alkalis. Since the electrons of the *d* shell are also involved in metallic bonding, the heat of sublimation and the melting point of Cu are also much higher than those of the alkalis. These factors are responsible for the more noble character of copper, and the effect is to make its compounds more covalent and to give them higher lattice energies.

The oxidation states and stereochemistry of Cu are summarized in Table 1.1.

1.1.1 The chemistry of copper(I), d^{10}

Cu(I) (d^{10}) compounds are diamagnetic and, except where color results from the anion or charge-transfer bands, colorless.

Table 1.1 Oxidation states and stereochemistry of copper

Oxidation State	Coordination number	Geometry	Examples
Cu(I), d^{10}	2	Linear	Cu_2O, KCuO, $CuCl_2^-$
	3	Planar	$K[Cu(CN)_2]$. $[Cu(SPMe_3)_3]ClO_4$
	4[a]	Tetrahedral	CuI, $[Cu(CN)_4]^{3-}$, $[Cu(MeCN)_4]^+$
	4	Distorted planar	CuL[c]
	5	*sp*	[CuLCO][c]
	6	Octahedral	$\{(Ph_2MeP)_3ReH_5\}_2Cu^+$[d]
Cu(II), d^9	3	Trigonal planar	$Cu_2(\mu\text{-}Br)_2Br_2$
	4[a,b]	Tetrahedral (distorted)	(N-Isopropylsalicylaldiminato)$_2$Cu
	4[a,b]	Square	CuO, $[Cu(py)_4]^{2+}$, $(NH_4)_2[CuCl_4]$
	6[a,b]	Distorted octahedral	K_2CuF_4, K_2[CuEDTA], $CuCl_2$
	5	*tbp*	$[Cu(bipy)_2I]^+$, $[CuCl_5]^{2-}$, $[Cu_2Cl_8]^{4-}$
	5	*sp*	$[Cu(DMGH)_2]_2$(s), $[Cu(NH_3)_5]^{2+}$[e]
	6	Octahedral	$K_2Pb[Cu(NO_2)_6]$
	7	Pentagonal bipyramidal	$[Cu(H_2O)_2(dps)]^{2+}$[f]
	8	Distorted dodecahedron	$Ca[Cu(CO_2Me)_4]\cdot 6H_2O$
Cu(III), d^8	4	Square	$KCuO_2$, $CuBr_2(S_2CNBu_2)$
	6	Octahedral	K_3CuF_6

[a]Most common states.

[b]These three cases are often not sharply distinguished.

[c]L = a macrocyclic N_4 anionic ligand.

[d]Copper coordinated to six H atoms in $Re(\mu\text{-}H)_3Cu$ system.

[e]In $K[Cu(NH_3)_5](PF_6)_3$.

[f]dps = 2,6-diacetylpyridine bis(semicarbazone).

The relative stabilities of Cu(I) and Cu(II) states are indicated by the following potential data:

$$Cu(I) + e = Cu \qquad E^0 = 0.52\ V$$

$$Cu(II) + e = Cu(I) \qquad E^0 = 0.153\ V$$

therefore

$$Cu + Cu(II) = 2Cu(I) \qquad E^0 = -0.37\ V$$

$$K = [Cu(II)]/[Cu(I)] \approx 10^6$$

The relative stabilities of Cu(I) and Cu(II) in aqueous solutions depend very strongly on the nature of anions or other ligands present and vary considerably with solvent.

The equilibrium $2Cu(I) \rightleftharpoons Cu + Cu(II)$ can readily be displaced in either direction. Thus with CN^-, I^- and Me_2S, Cu(II) reacts to give the Cu(I) compound; with anions that cannot give covalent bonds, (e.g., ClO_4^- and SO_4^{2-}) or with complexing agents that have their greater affinity for Cu(II), the Cu(II) state is favored.

An excellent illustration of how the stability of Cu(I) relative to Cu(II) may be affected by solvent is acetonitrile. The Cu(I) ion is very effectively solvated by MeCN and the Cu(I) halides have relatively high solubilities, versus negligible solubilities in H_2O. Cu(I) is more stable than Cu(II) in MeCN and the latter is, in fact, a comparatively powerfully oxidizing agent. The tetrahedral ion $[Cu(MeCN)_4]^+$ can be isolated in salts with large anions (e.g. ClO_4^-, PF_6^-, $CF_3SO_3^-$, and BF_4^-).

Copper (I) complexes are usually obtained by (a) direct interaction with Cu(I) salts, (b) reduction of corresponding Cu(II) compounds, or (c) reduction of Cu(II) in the presence of or by ligands. The stoichiometries of the compounds give little clue to their structures, which can be very complicated, and the copper atom can be two-, three-, or four- coordinate, or exist in infinite chains.

1.1.2 The chemistry of copper(II), d^9

Most Cu(I) compounds are easily oxidized to Cu(II) compounds, but further oxidation to Cu(III) is more difficult. The d^9 configuration makes Cu(II) subject to Jahn-Teller distortion if placed in an environment of cubic (i.e., regular octahedral or tetrahedral) symmetry, and this has a profound effect on all its stereochemistry. When six-coordinated, the "octahedron" is severely distorted. The typical distortion is elongated along one of the fourfold axis, so that there is planar array of four short Cu-L bonds and two *trans* long ones (Figure 1.1a).

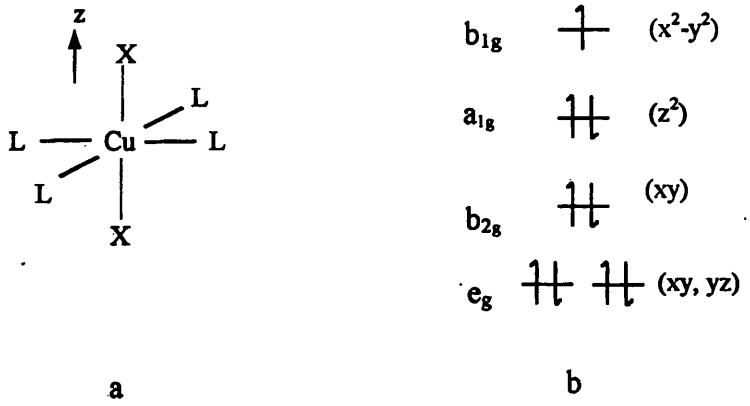

Figure 1.1 Tetragonal site geometry (a), and associated *d* orbital splitting (b).

This co-ordination geometry indicates a splitting in the *d* orbitals that is shown in Figure 1.1b. In the limit, of course, the elongation leads to a situation indistinguishable from square planar co-ordination. Thus the cases of tetragonally distorted octahedral co-ordination and square planar co-ordination cannot be sharply differentiated.

Because of the relatively low symmetry (i.e. less than cubic) of the environments in which the Cu(II) ion is characteristically found, detailed interpretations of the spectra and magnetic properties are somewhat complicated, even though one is dealing with the

equivalent of a one-electron case. A normal cupric complex is expected to have a tetragonal geometry with a $d_{x^2-y^2}$ ground state[2]. This ground state doublet splits linearly in a magnetic field, as shown in Figure 1.2a, by an amount $g\beta H$ where β is the Bohr magneton (= 4.6686 x 10^{-5} cm^{-1}/gauss), H is the external magnetic field, and the g factor is the quantity of experimental interest. An important feature of transition metal systems is that the g factor may deviate from 2.0023 and be anisotropic, that is have different values for the magnetic field oriented along ($g_{//}$) and perpendicular ($g_{\perp}$) to the molecular z direction in Figure 1.1a. These orientations correspond to EPR turning points (i. e., extrema) which dominate the orientation-averaged spectrum associated with a frozen solution or powdered cupric complex as show in Figure 1.2b. Additional features in this EPR spectrum derive from the copper nuclear spin of 3/2 which interacts with the electron spin producing a hyperfine splitting of the EPR signal into $2I+1 = 4$ allowed ($\Delta m_I = 0$, $\Delta m_s = 1$) transitions. From the spectrum in Figure 1.2b the hyperfine coupling constant (A) is also anisotropic with $A_{//}$ being quite large and $g_{//}$ is greater than $g_{\perp}$ which is greater than 2.0023, as required by ligand-field theory for a $d_{x^2-y^2}$ ground state. Weak ligand-field excited states ($\varepsilon < 50$ M^{-1} cm^{-1}) are expected in the 550 - 800 nm region and intense ligand-to-metal charge-transfer transitions dominate the higher energy region (the energy being dependent on the valence ionization energy of the specific ligand). There should be both σ- and π- charge-transfer transitions with σ at higher energy with greater intensity due to its greater overlap with the $d_{x^2-y^2}$ orbital. Virtually all complexes are blue or green. Exceptions are generally caused by strong UV bands (charge-transfer- bands) tailing off into the blue end of the visible spectrum, thus causing

the complexes to appear red or brown. The blue or green colors are due to the presence of the absorption bands in the region of 550-800 nm.

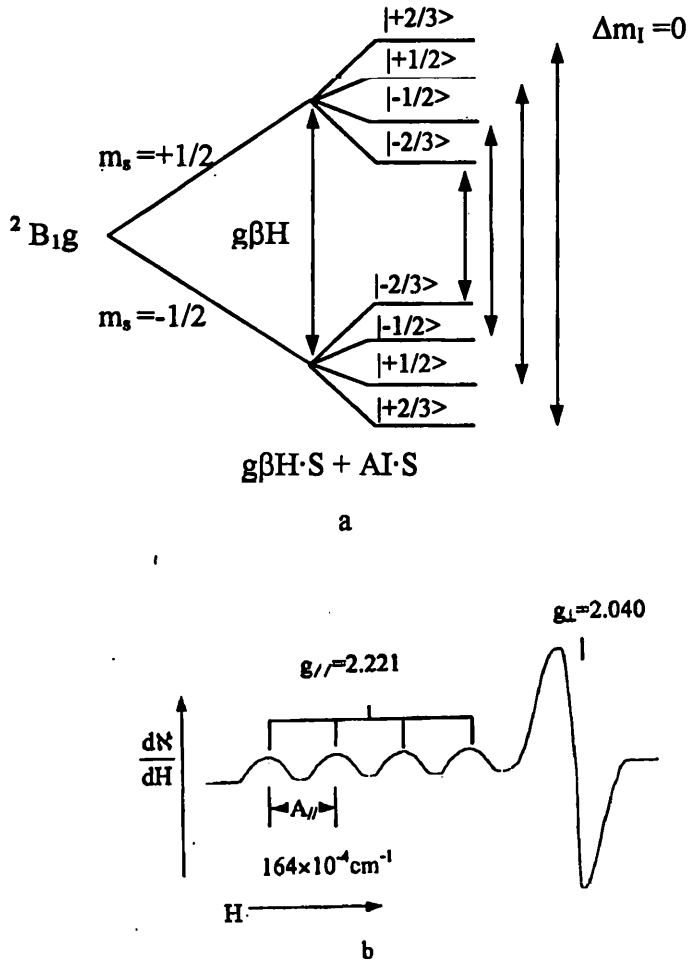

Figure 1.2 Ligand -field theory and ground-state electronic properties of normal cupric complexes: (a) $^2B_{1g}$ ground-state Zeeman splitting and hyperfine splitting diagram; (b) EPR spectrum of the $2B_{1g}$ ground state.

1.2. The structure and function of copper proteins

The critical role of copper in biological systems has been recognized for a long time. Copper is an essential component for living systems, although excess intake causes

symptoms such as Wilson's disease. Numerous copper-containing proteins are now known and can be categorized based on their functions as follows:

1. Electron-transfer carrier: plastocyanin, azurin, pseudoazurin, amicyanin, stellacyanin, and cucumber basic blue.

2. Dioxygen carrier: hemocyanin.

3.Oxygenation: tyrosinase, dopamineβ-hydroxylase, phenylalanine hydroxylase, peptidylglycine α- amidating monooxygenase.

4. Oxidation: amine oxidase, ceruloplasmin, ascorbate oxidase, laccase, cytochrome c oxidase.

5. Reduction: nitrite reductase, nitrous reductase.

6. Disproportionation: superoxide dismutase.

Based on structural features and spectroscopic properties, the active sites of copper proteins can be classified more precisely using Kitajima's nomenclature.[3] The definitions are as follows:

Type I. Mononuclear copper having a trigonal basal plane with an N_2S ligand set (S denotes thiolate sulfur from cysteine); exhibits unusual spectroscopic properties: (1) a strong absorption band at ~ 600 nm, (2) a small $A_{//}$ value of < 70 G, and (3) a high reduction potential (generally > 250 mV).

Type II. Mononuclear copper site exhibiting a normal EPR spectrum. This type, however, can be divided into the following three classes:

Type IIA: The ligand donors come from ordinary protein residues, such as histidine imidazole, cysteine thiolate, and water (or hydroxide).

Type IIB: The ligand donors include unusual protein side chains.

Type IIC: The copper is bridged to another metal ion, forming a hetero-dinuclear metal site.

Type III. EPR-silent dinuclear copper site that binds dioxygen as peroxide and exhibits unusual physicochemical characteristics: (1) diamagnetism, (2) two characteristic absorption bands at 350 and 580 nm, and (3) a low O-O vibration stretching frequency (~ 750 cm^{-1}).

Type IV. Trinuclear copper site having a isosceles triangle shape; two copper ions are strongly magnetically coupled.

Except for type II copper sites, which exhibit only the usual spectroscopic features, the structures and properties of other types of copper sites are noteworthy not only from the biological but also the inorganic point of view.

1.2.1 Blue copper proteins (Type I Copper)

Ubiquitous in nature, blue copper proteins function as rapid, long-range electron-transfer centres in biological systems. Blue copper proteins containing a single metal active site most notably include plastocyanin, azurin, amicyanin, stellacyanin, and cucumber basic blue. In addition, the blue copper centre is found in multicopper proteins such as ascorbate oxidase, laccase, and ceruloplasmin.

The active site structure of oxidized poplar plastocyanin (*Populus nigra*) has been defined by Freeman et al.[4] and serves as a useful geometric prototype of the blue copper centre (Figure 1.3). In the plastocyanin active site, the copper ion is at the centre of a C_{3v} elongated pseudotetrahedral co-ordination sphere. The Cu ion is ~ 0.36 Å above the NNS plane of the three equatorial ligands, two histidine (His) residues at 1.92 Å and 2.04 Å, and a cysteine (Cys) residue at 2.07 Å. Bound axially to the Cu ion,

appoximately along the trigonal (z) axis, is a methionine (Met) amino acid at an unusual long bond length of 2.82 Å. Ligand-field calculations,[6,7] have identified the Cu $3d_{x^2-y^2}$ as the half-occupied ground-state orbital oriented approximately in the NNS equatorial plane. These studies also demonstrate that the g_z direction of the site is ~ 5° off the Cu – S (Met) bond. The crystal structures reported for other blue copper proteins, including algal plastocyanin,[8] several azurins,[9-12] nitrite reductase[13-15] and ascorbate oxidase,[16] all exhibit a highly conserved active site geometry similar to that of poplar plastocyanin.

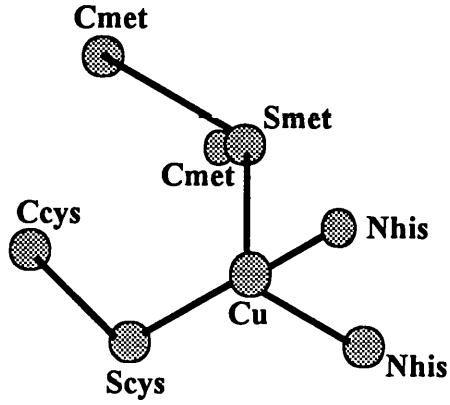

Figure 1.3 The active site structure of oxidized poplar plasotocyanin

The geometry of the blue copper site gives rise to unique spectroscopic features in the EPR and absorption spectra.[17-26] Most notably, an unusual small parallel hyperfine splitting is observed in the EPR spectrum (~65 x 10^{-4} cm^{-1} for plastocyanin) relative to that of normal Cu(II) systems (~ 170 x 10^{-4} cm^{-1}), and an exceptionally intense low-energy band is observed in the absorption spectrum at 600–630 nm ($\varepsilon \approx 5000$ cm^{-1}) that is not found in the spectra of normal Cu(II) complexes. The small EPR hyperfine splitting has been ascribed to the extremely high covalency of the oxidized Cu $3d_{x^2-y^2}$

HOMO,[27] which from X-ray absorption spectroscopy (XAS) at the S K-edge[28] and Cu L-edge[29] contains ~38% S character and only ~ 40% Cu character. From low-temperature MCD, the intense 600 nm "blue band" in the oxidized blue copper electron absorption spectrum has been attributed to a strong S (Cys) p to Cu $3d_{x^2-y^2}$ π charge transfer (CT) transition,[30] while the Cys σ charge transfer at higher energy is much weaker. The blue copper absorption spectrum is in sharp contrast to the spectra of normal Cu(II) systems which exhibit weak low-energy π CT bands and higher energy, intense σ CT transitions. The strong π interaction of S (Cys) with the Cu ion orients the Cu $3d_{x^2-y^2}$ orbital so that the Cu – S (Cys) bond axis bisects the lobes of this Cu *d* orbital. This results in the inverted π/σ intensity patterns in the absorption spectrum and provides a favorable super-exchange pathway for electron transfer through the cysteine residue. The reduction potentials of blue copper proteins are generally quite high (200 – 780 mV), favoring the reduced oxidation state. The high potentials of these proteins have been ascribed to the approximately T_d geometry of the oxidized state and the presence of the soft thioether and thiolate sulfur ligands[31-34]. In the X-ray crystal structure of reduced poplar plastocyanin the Cu – Met bond length is 2.9 Å, the Cu – Cys bond length is 2.10 Å, and the Cu –His bonds are 2.25 and 2.12 Å. In addition to the general contraction of the bonds on oxidation, a small angular distortion is also observed, wherein the Cu ion is shifted slightly toward the NNS equatorial plane. The relatively small distortion of the site on oxidation has been attributed to an entactic or rack state of the protein imposing the reduced Cu(I) geometry on the oxidized site.[35-38]

1.2.2 Coupled dinuclear copper proteins (Type II Copper)

Hemocyanin is a ubiquitous dioxygen carrier for invertebrates, containing a dinuclear copper site to which dioxygen is bound as peroxide.[2,22,39] A resonance Raman exploration with mixed labelled dioxygen established that the peroxide co-ordination is symmetrical.[40,41] Whereas the two Cu ions are divalent in the dioxygen binding state (so-called oxyhemocyanin), oxyhemocyanin is EPR silent and in fact, diamagnetic at room temperature, due to an enormously strong antiferromagnetic coupling ($-2J > 600$ cm^{-1}) between the two cupric ions.[42,43] Furthermore, instead of *d-d* bands normally observed at 600 – 700 nm for cupric complexes, oxyhemocyanin exhibits two intense bands at ~ 350 nm ($\varepsilon \sim 20{,}000$) and ~ 580 nm ($\varepsilon \sim 1000$), both attributed to $O_2^{2-} \rightarrow$Cu(II) LMCT transitions. Other intriguing features of oxyhemocyanin associated with the Cu(II)–O_2^{2-}–Cu(II) choromophore include the abnormally low $\nu_{(O\text{-}O)}$ frequency (~ 750 cm^{-1}) and a characteristic band at ~ 450 nm detected only in the CD spectrum.

X-ray structures of the deoxyhemocyanin from P. interruptus and from L. polyphemus have been reported[43,44]. In P. interruptus deoxyhemocyanin, each cuprous ion is surrounded by three histidyl nitrogen atoms from the protein chains, with a Cu···Cu separation of 3.54 Å. The co-ordination geometries of the two cuprous ions closely resemble each other; each consists of two short Cu–N bonds and a third distinctly elongated Cu–N bond. This feature is schematically indicated in Figure 1.4(a). It is noteworthy that the four nitrogen atoms and two cuprous ions proximately sit approximately on the same plane and the two apical nitrogen atoms relate to each other in a trans configuration. The dinuclear copper site in L. polyphemus deoxyhemocyanin, however, has structural features distinctive from those found in P. interruptus

deoxyhemo-cyanin. The Cu···Cu separation of 4.61 Å is much longer, and the coordination environment around each Cu is nearly trigonal planar with Cu–N ligand distances between 1.9 and 2.16 Å. The schematic diagram of the copper site is presented Figure 1.4(b). The 2.4 Å resolution structure of oxyhemocyanin from L polyphemus recently reported by Magnus et. al. reveals that the peroxide is bridged

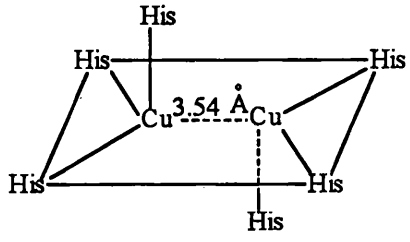

(a)

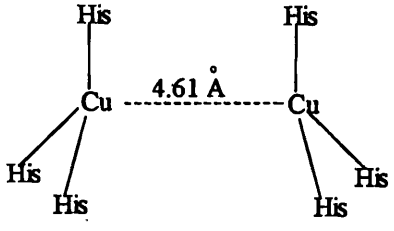

(b)

Figure 1.4 Schematic representation of the dinuclear copper site in deoxyhemocyanin: (a) P. interruptus; (b) L. polyphemus

between the two cupric ions in planar μ–η^2:η^2 co-ordination mode (Figure 1.5).[45] The overall structural features of the $N_3Cu(O_2)CuN_3$ chromophore including the Cu···Cu separation of 3.6 Å and the O–O distance of 1.4 Å in L. polyphemus oxyhemocyanin are very similar to those found in Kitajima's model complex $[Cu[HB(3,5iPr_2pz)_3]]_2(O_2)$.[46]

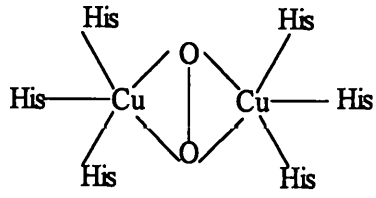

Figure 1.5 Schematic showing of the co-planar geometry in the oxygen binding site of L. polyphemus.

Charge-transfer and related spectral data provide direct probes of peroxide-metal bonds. In oxyhemocyanin, the intense O_2^{2-} π_σ^* $\rightarrow$ Cu charge-transfer reflects an extremely strong σ donor interaction which results from the fact that the μ-η^2:η^2 bridging peroxide in Figure 1.5 has two σ donor interactions with each copper in the dimer. This is complemented by the π acceptor interaction present only in the μ-η^2:η^2 bridged structure (Figure 1.6). Together these provide a very strong peroxide-dinuclear cupric bonding interaction which stabilises the oxyhemocyanin site from the loss of peroxide.

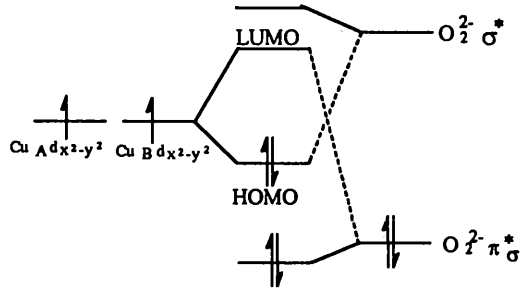

Fig. 1.6 Energy-level diagram for μ-η^2:η^2 peroxide-bridging geometry[47].

Tyrosinase is a monooxygenase that catalyses the oxidation of phenol to *o*-benzoquinone. Spectral studies on oxytyrosinase have shown that the active site in this

dinuclear copper enzyme is extremely similar to hemocyanin and has the same oxy intermediate[2]. The electronic structure described for oxyhemocyanin is thus also appropriate for oxytyrosinase and can make an important contribution to the activation of oxygen for the hydroxylation of phenolic substrates by this enzyme (Figure 1.7)[48]. The strong σ–donor interaction leads to a less negative peroxide, while the π acceptor interaction shifts electron density into the π^* orbital on peroxide which generally weakens the O–O bond and activates it for cleavage. A major difference between hemocyanin and tyrosinase is that the active site in tyrosinase is highly accessible to the substrate which coordinates directly to the copper centre.[49]

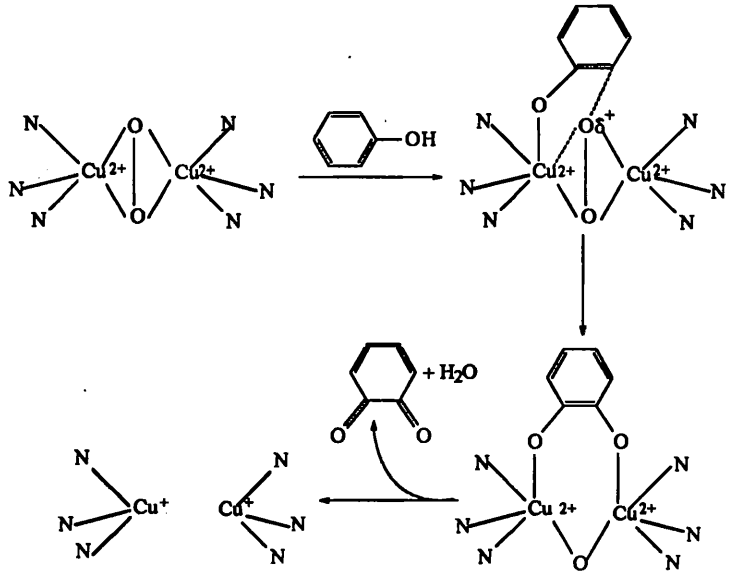

Figure 1.7 Proposed mechanism for oxygen activation in tyrosinase.

1.2.3 Multicopper oxidases (Type IV Copper)

The multicopper oxidases use at least four copper ions, which are grouped into three types based on their spectral properties, to couple four one-electron oxidations of substrate to the four-electron reduction of dioxygen to water[50]. Two of the copper centres form an antiferromagnetically coupled pair that is referred to as a type 3 centre. The type 1 centre is a blue copper site, and the type 2 copper is "normal" in the sense of having a tetragonal Cu(II) EPR spectrum ($g_{//} > g_{\perp} > 2.00$, $A_{//} > 140 \times 10^{-4}$ cm^{-1}) and weak ligand field absorption features in the visible spectrum[51]. Laccase is the simplest of the multicopper oxidases and contains one of the each type of centre for a total of four copper ions in the native enzyme[2,22,52-55].

The X-ray crystal structure of ascorbate oxidase from zucchini squash (cucurbita pepo medulosa) at 1.9 Å resolution has been determined by Messerschmidt et. al.,[16] and is believed to be a prototype for all the blue oxidases. Ascorbate oxidase consists of two identical subunits each of molecular weight 70,000 (552 amino acids). The four Cu atoms in one subunit are well separated from those in the other, and there are no cross-interactions. Each monomer folds into three β–barrel type domains which provide the co-ordination environment for the Cu atoms. The co-ordination and proximity of the Cu atoms to each other in the oxidised form are indicated in Figure 1.8. The type 1 Cu is in a plastocyanin like domain. A novel feature is the proximity of the normal type 2 and the dinuclear type 3 coppers giving a trinuclear site. The average Cu···Cu distance in the trinuclear copper site of ascorbate oxidase is 3.74 Å. The shortest distance between the type 1 copper centre and the trinuclear copper centre is 12.2 Å.

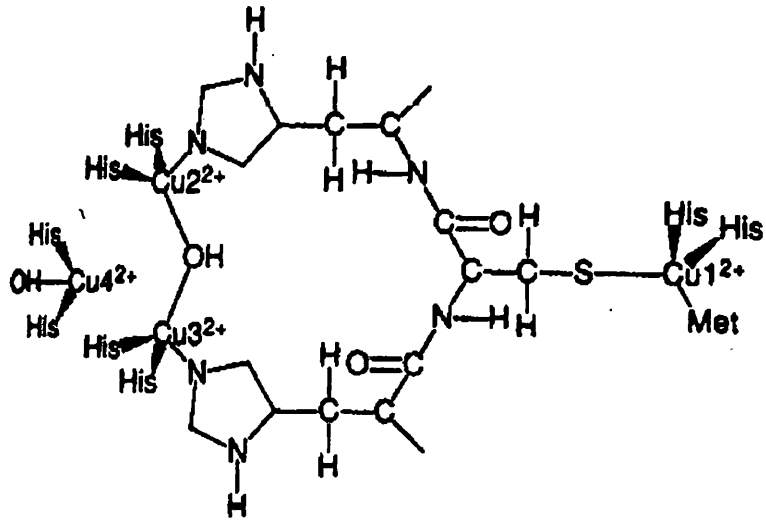

Figure 1.8 The location of the four Cu atoms in fully oxidized ascorbate oxidase from the X-ray crystal structure coordinates of the zucchini squash enzyme[56].

The X ray crystal structure of the reduced form of ascorbate oxidase[57] shows that the geometry at the type 1 copper centre remains much the same compared with the oxidized form. The structural changes are considerable at the trinuclear copper site. Thus on reduction the bridging OH is released and the two coppers Cu2 and Cu3 move toward their respective histidines and become three co-ordinated, a preferred stereo-chemistry for Cu(I). The Cu···Cu distances increase from an average of 3.7 to 5.1 Å for Cu2 –Cu3, 4.4 Å for Cu2–Cu4, and 4.1 Å for Cu3–Cu4.

The X-ray crystal structure of the peroxide form of ascorbate oxidase at 2.6 Å resolution[59] reveals that the geometry at the type 1 copper centre is not changed compared with that of the oxidised form. As in the reduced form, the structural changes are remarkable at the trinuclear copper centre. The bridging OH is absent, the peroxide

binds terminally to the Cu2 as hydroperoxide, and the Cu···Cu distances increase from an average of 3.7 Å to 4.8 Å for Cu2–Cu3 and 4.5 Å for Cu2–Cu4. The Cu3–Cu4 distance remains at 3.7Å.

Based on the X-ray crystal structure determinations of ascorbate oxidase and its fully reduced and peroxide derivatives, and spectroscopic studies, a proposed catalytic mechanism is given by Messerschmidt et. al.[57] and presented in Figure 1.9. It is believed that this scheme is also valid in principle for laccase due to the close similarities of both blue oxidases.

The catalytic cycle starts from the resting form (Figure 1.9a), in which all four copper ions are oxidised and Cu2 and Cu3 are bridged by an OH^-. Cu2 and Cu3 are most likely the spin-coupled type 3 pair of coppers and Cu4 is the type 2 copper. The first step is the reduction of the type 1 copper Cu1 by the reducing substrate in a one-electron transfer step (Figure 1.9b). The electrons are transferred through the protein to either Cu2 or Cu3. Electron transfer may be through-bond or through-space, or a combination of both. The fully reduced enzyme requires four electrons to be transferred (Figure 1.9c). The hydroxyl bridge between the copper pair has been released and the distance from Cu2 to Cu3 has been increased to about 5.1 Å. At this stage, dioxygen may bind to the enzyme at Cu2, probably in the manner shown in the peroxide derivative described previously. A transfer of two electrons from the copper pair to dioxygen leads to the formation of a hydroperoxide intermediate (Figure 1.9d). A third electron may be transferred from Cu1 to the hydroperoxide intermediate, and a fourth electron from the type 1 copper to Cu2. The O–O bond is broken at this stage and the first water molecule released. (Figure 1.9e). The EPR spectrum indicates that the type 1 copper has been

reoxidized and that the EPR signals of the oxygen radical intermediate and type 1 copper are present. The Cu2 is in the reduced state, whereas the oxidised copper atoms Cu3 and Cu4 may be spin coupled and EPR silent. The reduced Cu2 may facilitate O–O bond breakage and release of water. The catalytic cycle is continued by a further reduction of the type 1 copper centre by the reducing substrate. The fourth electron may be transferred to the oxygen radical intermediate from copper atom Cu2 and the second water molecule released (Figure 1.9f). In the case of only four electron equivalents, the reaction may lead to the resting form and the second water may remain bound as the bridging ligand between Cu2 and Cu3, concomitant with a substantial rearrangement within the trinuclear copper site and its coordinating ligands. If the turnover is continued, this will not occur and the trinuclear copper site may maintain a structure very close to that found in the fully reduced form. Only minor rearrangements will take place at the trinuclear copper site during the catalytic cycle, a prerequisite for facile electron transfer reactions. The four protons required for the formation of two water molecules from oxygen may be supplied from bulk water through the dioxygen channel via the water molecules bound in the vicinity of Cu2 and Cu3.

1.3 Macrobicyclic ligands cryptands and dinuclear macrobicyclic complexes cryptates [58,59]

Compared to macrocycles, which have a two dimensional framework, cryptands are three dimensional in structure (Figure 1.12) and contain an intramolecular cavity (or"crypt")[60,61].

Cryptands form inclusion complexes, the cryptates, in which the substrate is located inside the cavity. Comparision between macrocycles and macrobicycles

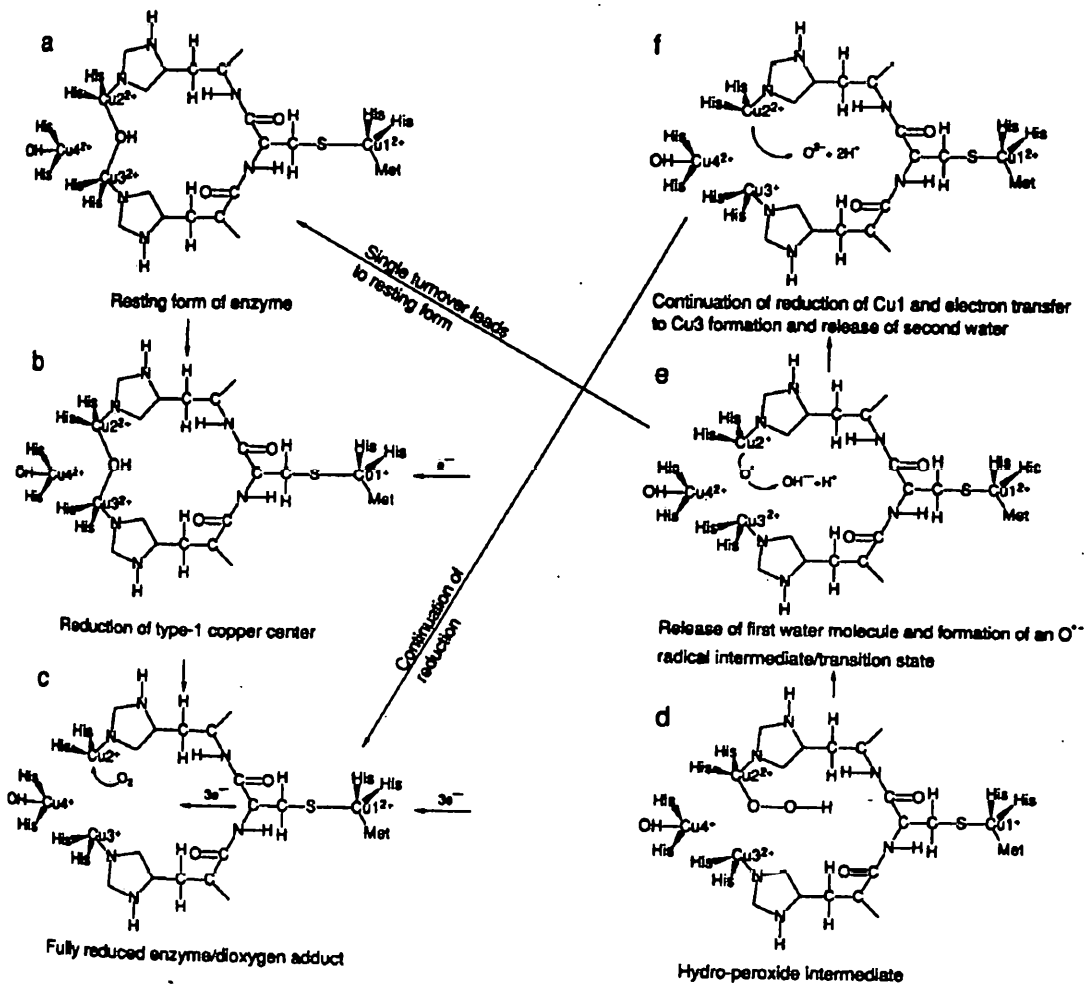

Figure 1.9 Proposed catalytic mechanism of ascorbate oxidase.

illustrates the quantitative just as much as qualitative differences in properties between these two types of ligands. These are reflected in synthetic strategies, conformational properties and structures as well as in the physical, structural, complexing, and chemical properties.

Figure 1.10 Two dimensional structure of a macrocycle, and three dimensional structure of a macrobicycle or cryptand, together with representations of their complexes.

1.3.1 Synthesis

Several synthetic strategies can be envisaged (Fig. 1.11): (a) stepwise, (b) tripode coupling, (c) single capping, (d) double capping, (e) internal template, (f) external template.

(a)

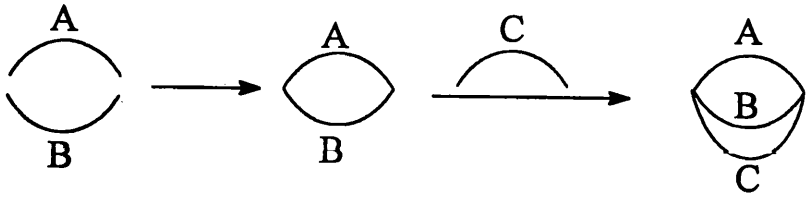

(b)

(c)

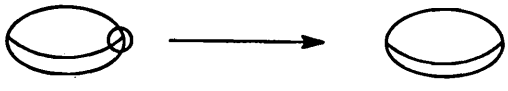

Figure 1.11 (continued)

(d)

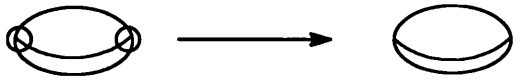

(e)

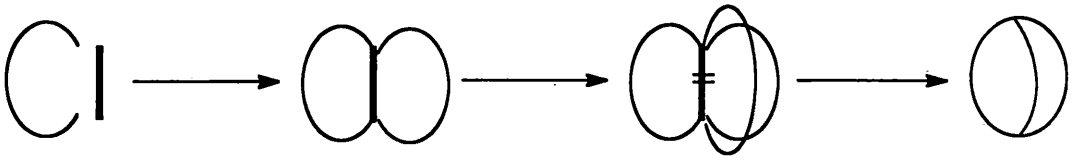

(f)

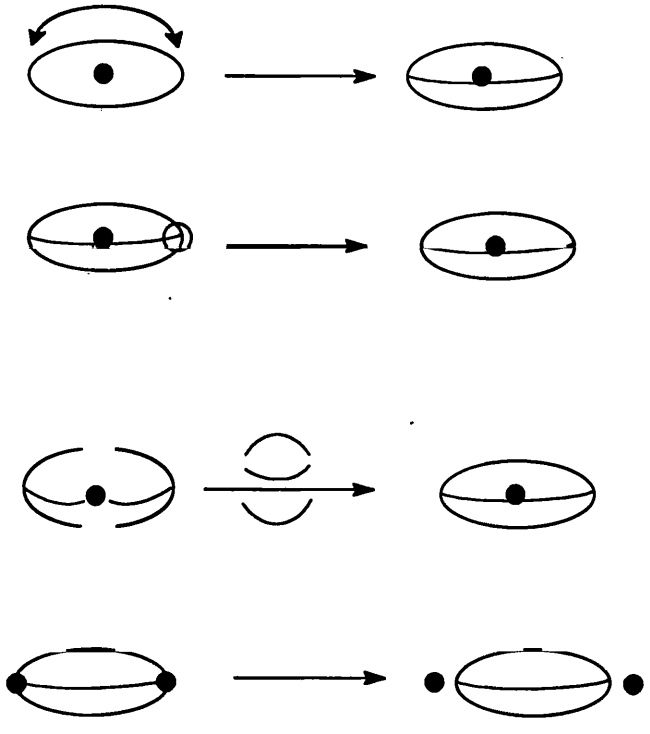

Fig. 1.11 Synthetic strategies for cryptands: (a) stepwise, (b) tripode coupling, (c) single capping, (d) double capping, (e) internal template, (f) external template.

Although critical evaluation of these synthetic strategies is difficult without further specifying the chemical nature of the system under study, it is possible to formulate some simple rules:

- Efficient synthesis generally requires the use of high dilution conditions to minimize the formation of oligomers and polymers;
- The cyclization steps should be very fast in order to maintain high dilution conditions (low stationary concentration) throughout the reaction;
- Rigid components considerably increase the yield. They reduce the number of conformational degrees of freedom thus increasing the probability of a favourable conformation and hence also the cyclization rate;
- The chains undergoing condensation should have similar lengths;
- Use of templates increases the cyclization yield by keeping the chains together during the reaction;
- Both the reactants and the products should be stable under the reaction conditions since high dilution requires slow addition of the reactants and a long reaction time.

1.3.2 Coordination chemistry of polyazacryptands[62]

The early cryptands, developed by Lehn and co-workers[61, 63, 64] were derived from diazacrown ethers by adding a third polyether strand. The value of these polyoxo-cryptands is their propensity to coordinate Group I cations and other main group cations. In general, complexation of transition metal ions and heavy main group cations is not efficiently achieved with polyoxocryptands. On the other hand, polyazacryptands containing sp^2- or sp^3-N donors are much better equipped to coordinate transition metal ions and many main group 3-14 cations[65, 66]. In addition to their ability to complex

cations, polyazacryptands form a series of positively-charged species in solution, that can bind anions through electrostatic attractive forces and hydrogen bonds. Many polyazacryptands can encapsulate a pair of cations and the resultant dinuclear cryptates act as metalloreceptors, hosting bridging anions in "cascade fashion".

Potential applications of polyazacryptands arise directly from their coordination properties. The relatively high thermodynamic and kinetic stabilities deriving from the "cryptate effect" (where stability constants, K can be as much as 10^5 times high as in analogous macrocyclic complexes) can lead to applications in detoxification or environmental remediation via sequestration of harmful cations; in medical treatments via transport of cations for imaging purposes; or in hydrometallurgy for extraction of precious metals from mine waste water or other low concentration aqueous sources. Many cations with redox behavior appropriate to catalysis of important biochemical processes are strongly coordinated by polyazacryptands. Rapid electron transfer can be assured within a rigid cage where geometry is predetermined by the ligand; the cation is thus prevented from relaxing toward its preferred geometry in either redox state. The combination of kinetic stability toward decomplexation, and coordination geometry invariant upon redox exchange makes these cryptates potentially valuable as redox reagents.

Following the development of a facile synthetic route[67, 68] to polyazacryptands, we have successfully synthesized a series of hexaimino cryptands **L1-L5** and their reduced forms, octaamino cryptands **RL1-RL5** (Scheme 1). In the following chapters the synthesis of the dicopper(I)/(II) complexes of these cryptands, their redox behavior, structural, spectroscopic, and magnetic properties, and their reactivities in catalytic

oxidation reactions will be discussed. The hexaimino cryptands **L1-L5** are good hosts for a pair of Cu(I) ions due to the presence of the softer sp^2-N donors, and the rigidity of the ligands which can impose a trigonal or distorted tetrahedral coordination geometry favored by the Cu(I) oxidation state. On the other hand, the octaamino cryptands **RL1-RL5** show good coordination properties for a pair of Cu(II) ions, in view of the replacement of the softer sp^2-N donors with the harder sp^3-N donors and the increased flexibility of the ligands upon the reduction of C=N bonds in the hexaimino cryptands.

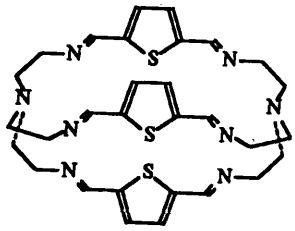

L1

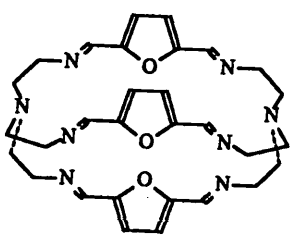

L2

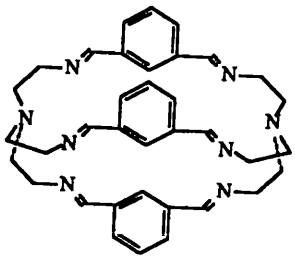

L3

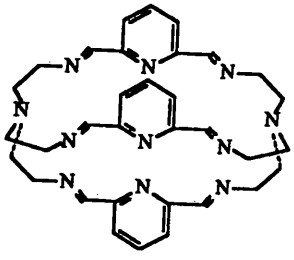

L4

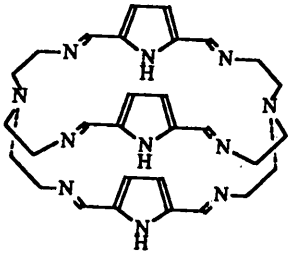

L5

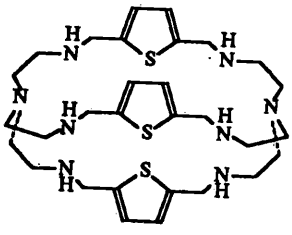

RL1

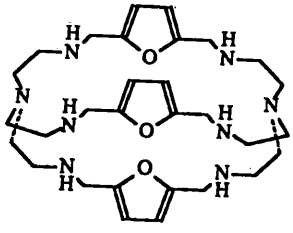

RL2

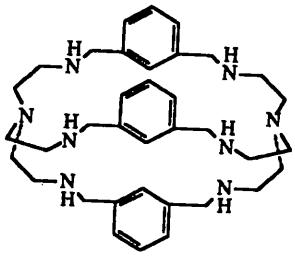

RL3

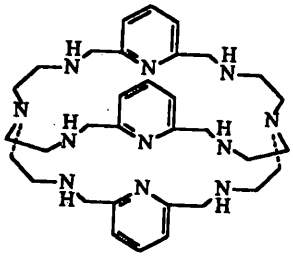

RL4

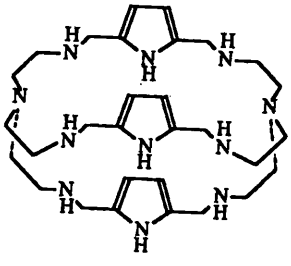

RL5

Scheme 1

CHAPTER 2 EXPERIMENTAL

2.1. Preparations

1,4,11,14,17,24,29,36-octaaza-39,40,41-trithiopentacyclo[12.12.12.$1^{6,9}$.$1^{19,22}$. $1^{31,34}$]-hentetraconta-4,6,8,10,17,19,21,23,29,31,33,35-dodecaene (**L1**), 1,4,11,14,17,24,29,36-octaaza-39,40,41-trithiopentacyclo[12.12.12.$1^{6,9}$.$1^{19,22}$. $1^{31,34}$]-hentetraconta-6,8,19,21,31,33 -hexaene (**RL1**), and their copper(I)/(II) complexes.

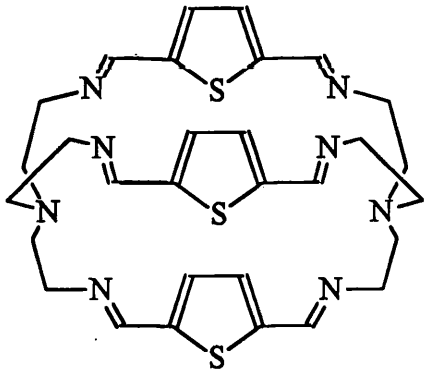

L1

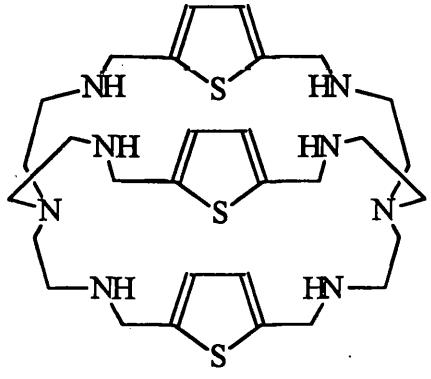

RL1

2,5-Diformyl Thiophene.[69]

Step 1: Preparation of 2,5-bis(chloromethyl)thiophene

A stream of dry hydrogen chloride gas was passed through a stirred solution of 37% formaldehyde (2 mol) and 10 M hydrochloric acid (36 ml) allowing the temperature to rise to 50-60 °C. After 2 hours the solution was saturated with HCl. The mixture was cooled to 30 °C and thiophene (0.6 mol) was added dropwise with stirring. After 20 minutes, the oily layer was siphoned off and washed with cold water (5×35 ml) and

refrigerated overnight. The solid mass was allowed to warm to room temperature. It was then filtered under vacuum, washed with toluene and dried in vacuum to yield the light brown solid, 2,5-bis(chloromethyl)thiophene in 75% yield. This was used in the next stage without further purification.

Sept 2: Preparation of pyridine adduct

The 2,5-bis(chloromethyl)thiophene (63 g), pyridine (74 ml) and ethanol (70 ml) were warmed gently on a water bath. After 20 minutes a white solid appeared. Heating was continued for 30 minutes and then the precipitate was collected, washed with ether and recrystallised from ethanol to give the pyridine adduct in 96% yield.

Sept 3: Preparation of nitroso adduct

The pyridine adduct (61 g) was dissolved in ethanol (1000 ml) together with p-nitroso-N,N-dimethlyaniline (50 g). A solution of sodium hydroxide (13 g) in water (300 ml) was added while the mixture was being ice cooled. After stirring for 2 hours, the mixture was diluted with water (600 ml) and allowed to stand overnight. The red precipitate was collected and recrystallized from ethanol to give the nitroso adduct in 70% yield.

Step 4: Preparation of 2,5-diformylthiophene

The nitroso adduct (50 g) was added to ice cold 2 M hydrochloric acid (1000 ml) and the brownish solution was stirred for 30 minutes during which time a yellow precipitate was formed. The mixture was allowed to stand for 2 hours at room temperature. The solid was collected, washed with cold water, dried and recrystallized from ether to give pale yellow 2,5-diformylthiophene in 80% yield.

$[Ag_2L1][O_3SCF_3]_2$. 2,5-Diformylthiophene (0.003 mol) was dissolved in methanol (100 ml) and filtered into a solution of silver nitrate (0.002 mol) in methanol (100 ml). A solution of 0.002 mol tren (tris-(2-aminoethyl)amine) in methanol was added dropwise over 1 hr before black silver powder was filtered off to leave a clear yellow solution. FAB mass spectrum (m/z, ion, relative %): 969, $[Ag_2L1(O_3SCF_3)]^+$, 67; 711, $[AgL1]^{2+}$, 100. Anal. Calc. for $C_{32}H_{36}Ag_2F_6N_8O_6S_5$: C, 34.20; H, 3.20; N, 10.40. Found: C, 34.35; H, 3.25; N, 10.10.

$[Cu_2L1][BF_4]_2$. 2,5-Diformylthiophene (0.003 mol) was dissolved in ethanol (50ml) at room temperature and then tren (0.002 mol) in ethanol (10 ml) was added dropwise. After bubbling N_2 through the solution for 10 min $[Cu(MeCN)_4][BF_4]$ (0.002mol) in deoxygenated acetonitrile (30 ml) was added. The volume was reduced under N_2 until an orange solid precipitated in 59% yield. FAB mass spectrum (m/z, ion, relative %): 819, $[Cu_2L1(BF_4)]^+$, 32; 732 $[Cu_2L1]^{2+}$, 70; 667 $[CuL1]^+$, 20. Anal. Calc. for $C_{30}H_{36}Cu_2B_2F_8N_8S_3$: C, 39.80; H, 4.00; N, 12.40. Found: C, 39.50; H, 3.95; N, 12.40.

$[Cu_2L1][O_3SCF_3]_2$ suitable for X-ray crystallography was obtained by transmetallation of $[Ag_2L1][O_3SCF_3]_2$ with $[Cu(MeCN)_4][O_3SCF_3]$ followed by recrystallisation from acetonitrile-ethanol mixture.

RL1. $[Ag_2L1][O_3SCF_3]_2$ (0.0036 mol) was brought to reflux in methanol (300 ml) before 0.036 mol solid $NaBH_4$ was added in small portions. The resulting suspension was refluxed for 4 hr. On cooling the precipitate was filtered off and the solution was reduced to dryness on a rotary evaporator. The residue was dissolved in 60 ml strong NaOH solution (4 g in 60 ml H_2O) and then was extracted with chloroform (6 × 60 ml). The combined extract was washed with water (4 × 15 ml) and dried with

anhydrous Na_2SO_4 until cloudiness of the washed extract disappeared. The chloroform solution was reduced to dryness, leaving an oil that was then dissolved in methanol (100 ml). On filtering off the small amount of white insoluble material and removing the solvent a waxy solid of **RL1** was obtained in 60% yield. Mass spectrum: m/z = 616 (parent ion).

$[Cu_2$**RL1**$][ClO_4]_2$. **RL1** (0.0005 mol) was dissolved in deoxygenated ethanol (30 ml) and $[Cu(MeCN_4)][ClO_4]$ (0.001 mol) in deoxygenated acetonitrile (30 ml) was added. The mixture was heated at 40 °C under argon. On reducing the volume by bubbling Ar, $[Cu_2$**RL1**$][ClO_4]_2$ was obtained as a very pale green solid in 47% yield. It is reasonably stable in air over a period of months, but goes green in solution within minutes unless an inert atmosphere is provided. Anal. Calc. for $C_{30}H_{42}Cu_2Cl_2N_8O_8S_3$: C, 38.20; H, 5.10; N, 11.90. Found: C, 38.00; H, 5.15; N, 11.45.

$[Cu_2$**RL1**$(OH)][ClO_4]_3 \cdot H_2O$. **RL1** (0.0005 mol) was dissolved in ethanol (30 ml) at 50 °C and $Cu(ClO_4)_2 \cdot 6H_2O$ (0.001 mol) in acetonitrile (20 ml) was added. The mixture was stirred for 30 min at 50 °C in the presence of pyrazole (0.0005 mol) as base. On reducing the volume, bright green microcrystals of product with ν_{OH} at 3571 cm^{-1} were obtained in 55% yield. Anal. Calc. for $C_{30}H_{45}Cu_2Cl_3N_8O_{14}S_3$: C, 33.45; H, 4.75; N, 10.40. Found: C, 33.45; H, 4.50; N, 10.50.

$[Cu_2$**RL1**$(im)][O_3SCF_3]_3$. This complex was synthesised in a similar way as $[Cu_2$**RL1**$(OH)][ClO_4]_3 \cdot H_2O$ except that imidazole (0.0005 mol) was used to replace pyrazole. Greenish blue needles which lacked ν_{OH} infrared absorption were obtained in

53% yield. Anal. Calc. for $C_{36}H_{45}Cu_2F_9N_{10}O_9S_6$: C, 34.50; H, 3.90; N, 11.20. Found: C, 34.30; H, 4.00; N, 11.20.

$[Cu_2\mathbf{RL1}(N_3)][ClO_4]_3$. **RL1** (0.0005 mol) in methanol (30 ml) and $Cu(ClO_4)_2 \cdot 6H_2O$ (0.001 mol) in acetonitrile (20 ml) were mixed before NaN_3 (0.0005 mol) dissolved in minimum (*ca.* 0.1 ml) of water was added. The green solution changed colour to brown from which gold brown microcrystals of product were isolated in 57% yield. Anal. Calc. for $C_{30}H_{42}Cu_2Cl_{13}N_{11}O_{12}S_3$: C, 33.20; H, 4.45; N, 14.20. Found: C, 33.25; H, 4.35; N, 14.15.

1,4,11,14,17,24,29,36-octaaza-39,40,41-trioxapentacyclo[12.12.12.$1^{6,9}$.$1^{19,22}$.$1^{31,34}$]-hentetraconta-4,6,8,10,17,19,21,23,29,31,33,35-dodecaene (**L2**), 1,4,11,14,17,24,29,36-octaaza-39,40,41-trioxapentacyclo[12.12.12.$1^{6,9}$.$1^{19,22}$.$1^{31,34}$]-hentetraconta-6,8,19,21,31,33 -hexaene (**RL2**), and their copper(I)/(II) complexes.

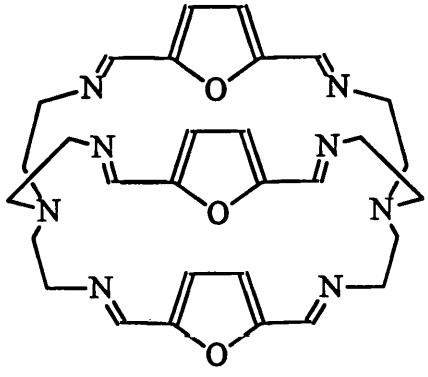

L2

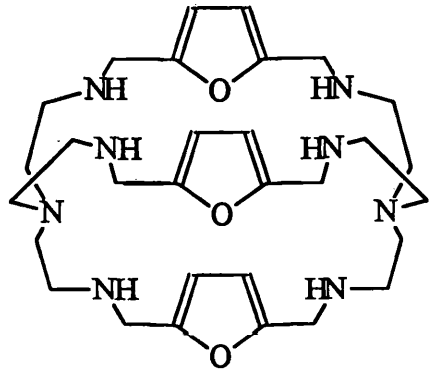

RL2

2,5-Diformylfuran

This compound was prepared by modifications of an existing preparation[67]. 2,5-Dimethanol furan (27.5 g) was added to a suspension of freshly activated manganese dioxide (150 g) in toluene (750 ml). The mixture was stirred and refluxed for six hours during which time the solution changed colour from deep orange/brown to yellow. On cooling, the solution was filtered to remove the manganese dioxide and the filtrate was reduced to dryness on the rotary evaporator. The raw product was recrystallised from 1:1 chloroform/carbon tetrachloride. During recystallisation a small quantity of charcoal was added to remove the impurities. The clean product of 2,5-diformylfuran was obtained in 45% yield.

L2. A solution of tren (0.002 mol) in 40 ml methanol was stirred at 30-40 °C as a solution of 2,5-diformylfuran (0.003 mol) in 40 ml methanol was slowly added. The

mixture was stirred at room temperature for an hour and the volume was reduced to 20 ml before an equal volume of acetonitrile was added. The resulting solution was left to evaporate in air and transparent cubic crystals were isolated in 62% yield. ^{1}H NMR ($CDCl_3$): 7.09 (s, 6H); 7,73 (s, 4H); 3.53 (br s, 12H); 2.74 (br s, 12H).

$[Cu_2L2]X_2 \cdot nH_2O$ (X = ClO_4^-, n = 2; X = BF_4^-, n = 0). **L2** (0.0004 mol) was dissolved in 30 ml deoxygenated methylene chloride and a solution of $Cu(MeCN)_4X$ (0.0008 mol) in deoxygenated actonitrile (20ml) and ethanol (20ml) was added. The volume of the solution was reduced to ~ 20ml in a rotary evaporator. Red crystals suitable for X-ray study were obtained the next day in about 80% yield.

$[Cu_2L2][ClO_4]_2 \cdot 2H_2O$. ^{1}H NMR ($CD_3CN$): 7.10 (s, 6H); 8.22 (s, 6H); 3.42 (m, 6H); 3.23 (d, 6H); 3.12 (d, 6H); 2.67 (t, 6H). Anal. Calc. for $C_{30}H_{40}Cu_2Cl_2N_8O_{13}$: C, 39.2; H, 4.00; N, 12.2. Found: C, 39.8; H, 4.4; N, 12.2.

$[Cu_2L2][BF_4]_2$. Anal. Calc. for $C_{30}H_{36}Cu_2B_2F_8N_8O_3$: C, 42.0; H, 4.20; N, 13.1. Found: C, 41.7; H, 4.20; N, 12.9.

$[Cu_2L2(OH)]X_3 \cdot mCH_3CN \cdot nH_2O$ (X = ClO_4^-, m = 0, n = 2; X = PF_6^-, m = 1, n = 1). 0.0005 mol **L2** was dissolved in 30 ml methylene chloride and to this solution 0.001 mol CuX_2 in 30 ml ethanol was added. This resulted in a rapid precipitation of yellow-green solid that slowly turned green on filtration in air. Quick recrystallisation in acetonitrile/ethanol gave emerald green small crystals. Yield 60-70%.

$[Cu_2L2(OH)][ClO_4]_3 \cdot 2H_2O$. Anal. Calc. for $C_{30}H_{41}Cu_2Cl_3N_8O_{18}$: C, 34.8; H, 4.00; N, 10.8. Found: C, 34.9; H, 4.10; N, 10.9.

$[Cu_2L2(OH)][PF_6]_3 \cdot MeCN \cdot H_2O$. Anal. Calc. for $C_{32}H_{42}Cu_2F_{18}N_9O_5P_3$: C, 32.2; H, 3.30; N, 10.5. Found: C, 32.3; H, 3.40; N, 10.6%.

$[Cu_2L2(im)][ClO_4]_3 \cdot H_2O$. To a solution of 0.0005 mol **L2** in 30 ml CH_2Cl_2 was added 0.0006 mol imidazole in 10 ml ethanol and 0.0011 mol $Cu(ClO_4)_2 \cdot 6H_2O$ in 30 ml ethanol. A grey-blue solid was isolated in 77 % yield. Anal. Calc. for $C_{33}H_{41}Cu_2Cl_3N_{10}O_{16}$: C, 37.1; H, 3.80; N, 13.1. Found: C, 36.2; H, 3.70; N, 13.3%.

$[Cu_2L2'(im)][ClO_4]_3 \cdot 2H_2O$. This dark-blue dicopper(II) complex of the dipendant amine macrocycle was obtained in an attempt to purify the crude $[Cu_2L2(im)][ClO_4]_3$ product by recrystallisation from 1:1 acetonitrile/ethanol. Anal. Calc. for $C_{27}H_{36}Cu_2Cl_3N_{10}O_{14}$: C, 32.5; H, 4.30; N, 14.0. Found: C, 32.6; H, 4.10; N, 13.5%.

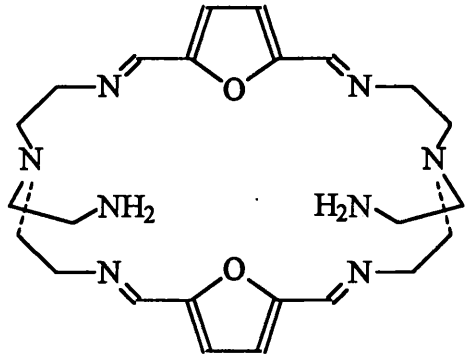

L2'

RL2. This ligand was prepared in the same way as was described for **RL1**. Yield 72%. ^1H NMR (CD_3CN): 6.08 (s, 6H); 3.70 (s, 6H); 2.57 (s, 24H).

$[Cu_2RL2(OH)]X_3 \cdot nMeCN \cdot mH_2O$ (X = ClO_4^-, n = 1, m = 0; X = $O_3SCF_3^-$, n = 0, m = 1). 0.0005 mol **RL2** was dissolved in 40 ml ethanol before 0.0005 mol pyrazole in 10 ml ethanol and 0.001 mol CuX_2 in 30 ml acetonitrile were added. The solution was stirred at room temperature for one hour and green crystals were collected after 24 hours

$[Cu_2$**RL2**$(OH)][ClO_4]_3 \cdot$MeCN. Anal. Calc. for $C_{32}H_{46}Cu_2Cl_3N_9O_{16}$: C, 36.5; H, 4.90; N, 12.0. Found: C, 36.4; H, 5.00; N, 11.9%.

$[Cu_2$**RL2**$(OH)][O_3SCF_3]_3 \cdot H_2O$. Anal. Calc. for $C_{33}H_{45}Cu_2F_9N_8O_{14}S_3$: C, 33.7; H, 4.40; N, 9.50. Found: C, 33.8; H, 4.40; N, 9.30%.

$[Cu_2$**RL2**$(im)][ClO_4]_3 \cdot H_2O$. 0.0005 mol **RL2** and 0.0005 mol imidazole were dissolved in 50 ml ethanol and to this solution was added 0.001 mol $Cu(ClO_4)_2 \cdot 6H_2O$ in 30 ml acetonitrile. The mixture was stirred for one hour and left overnight. Blue crystals were collected in 63% yield. Anal. Calc. for $C_{33}H_{47}Cu_2Cl_3N_{10}O_{16}$: C, 36.7; H, 4.90; N, 13.0. Found: C, 36.4; H, 4.50; N, 12.8%.

$[Cu_2$**RL2**$(N_3)][O_3SCF_3]_3$. 0.0005 mol **RL2** was dissolved in 60 ml 1:1 ethanol-acetonitrile before adding 0.001 mol $Cu(O_3SCF_3)_2$ in 20 ml ethanol and 0.0005 mol NaN_3 in 1 ml H_2O. Brown crystals precipitated in half an hour. Yield 59%. Anal. Calc. for $C_{33}H_{42}Cu_2F_9N_{11}O_{12}S_3$: C, 33.4; H, 4.00; N, 13.0. Found: C, 33.6; H, 3.90; N, 12.7%.

$[Cu_2$**RL2**$][ClO_4]_2$.0.0005 mol **RL2** was dissolved in 80 ml deoxygenated 2:1 ethanol/acetonitrile before 0.001 mmol $Cu(MeCN)_4ClO_4$ was added in solid form. Ar was bubbled through the solution until plenty of white solid appeared. This product was separated under Ar and slowly oxidised in air. Yield 72%. Anal. Calc. for $C_{30}H_{42}Cu_2Cl_2N_8O_{11}$: C, 40.3; H, 5.40; N, 12.5. Found: C, 40.8; H, 5.20; N, 12.6%.

$[Cu_2$**RL2**$(CO)_2][BF_4]_2$. 0.0005 mol **RL2** was dissolved in deoxgenated 80 ml 2:1 ethanol/acetonitrile and the resulting solution was saturated with CO at room temperature before 0.001 mol $Cu(MeCN)_4BF_4$ was added in solid form. CO was bubbled through the solution until there was a copious precipitate. After filtering under a CO

atmosphere, the pale green product was obtained in 31% yield. Anal. Calc. for $C_{32}H_{42}Cu_2B_2F_8O_5$: C, 41.5; H, 5.2; N, 12.1. Found: C, 41.2; H, 5.3; N, 12.5%.

1,4,12,15,18,26,31,39-octaazapentacyclo[13.13.13.$1^{6,10}$.$1^{20,24}$. $1^{33,37}$]-tetratetraconta-4,6(7),8,10(42),11,18,20(21),22,24(43),25,31,33(34),35,37(44),39-pentadecaene(**L3**),

1,4,12,15,18,26,31,39-octaazapentacyclo[13.13.13.$1^{6,10}$.$1^{20,24}$. $1^{33,37}$]-tetratetraconta-6(7),8,10(42),20(21),22,24(43),33(34),35,37(44)-nonaene (**RL3**), and their copper(I)/(II) complexes.

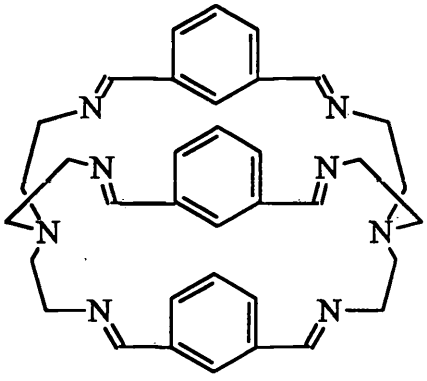

L3

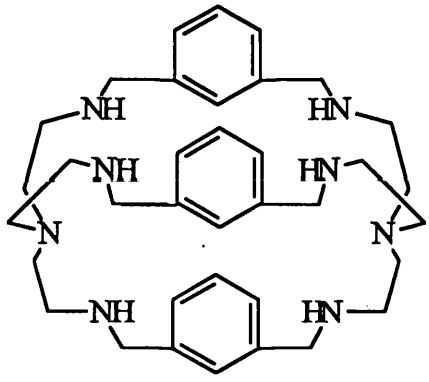

RL3

L3. Isophthalaldehyde (0.003 mol) was dissolved in 150 ml methanol before tren (0.002 mmol) was added in concentrated form. The mixture was stirred at 40 °C for one hour. Fine white crystals were obtained on cooling. Yield 87%. ^{1}H NMR (CD_2Cl_2): 5.3 (s, 3H); 8.14 (d, 6H); 7.52 (t, 6H), 7.49 (s 6H), 3.75 (m, 6H), 3.19 (t, 6H), 2.87 (t, 6H), 2.62 (q, 6H).

[Cu_2**L3**]$X_2 \cdot nH_2O$ ($X = ClO_4^-$, $n = 2$; $X = BF_4^-$, $n = 5$). Isophthalaldehyde (0.003 mol) was dissolved in 50 ml ethanol before tren (0.002 mol) was added in concentrated form. The solution was stirred and deoxygenated for half an hour and was added 0.002 mol $Cu(MeCN)_4X$ in 30 ml deoxygenated acetonitrile. Nitrogen was bubbled through the

solution until there was a copious precipitate. Yellow microcrystals were obtained in 50-60% yield.

$[Cu_2L3][ClO_4]_2 \cdot 2H_2O$. Anal. Calc. for $C_{36}H_{46}Cu_2Cl_2N_8O_{10}$: C, 45.6; H, 4.9; N, 11.8. Found: C, 44.6; H, 5.2; N, 11.4%.

$[Cu_2L3][BF_4]_2 \cdot 3H_2O$. Anal. Calc. for $C_{36}H_{48}Cu_2B_2F_8N_8O_3$: C, 43.9; H, 5.1; N, 11.9. Found: C, 43.8; H, 4.6; N, 11.5%.

$[Cu_2L3(OH)][ClO_4]_3 \cdot 3H_2O$. 0.0005 mol **L3** was dissolved in 30 ml methylene chloride before 0.001 mol $Cu(ClO_4)_2 \cdot 6H_2O$ in 40 ml ethanol was added. This produced a grass-green precipitate immediately. The solid was separated by suction and was recrystallized rapidly from 1:1 acetonitrile/ethanol. A bright green microcystalline product was isolated in 43% yield. Anal. Calc. for $C_{36}H_{49}Cu_2Cl_3N_8O_{16}$: C, 39.5; H, 5.6; N, 10.2. Found: C, 39.6; H, 5.5; N, 10.1%.

$[Cu_2L3'(OH)][ClO_4]_3 \cdot 2H_2O$. If the preparation of $[Cu_2L3(OH)][ClO_4]_3$ was carried out in acetonitrile instead of ethanol, the precipitation of green powder was avoided, and the reaction mixture turned blue within an hour or so. Slow evaporation of the blue reaction mixture gave thin blue crystals. Yield 34%. Anal. Calc. for $C_{28}H_{35}Cu_2Cl_3N_8O_{15}$: C, 34.8; H, 4.60; N, 11.6. Found: C, 35.2; H, 4.60; N, 11.6%.

$[Cu_2L3"OH)][O_3SCF_3][BPh_4]_2 \cdot 2H_2O$. To a solution of 0.0002 mol **L3** in 80 ml ethanol was added 0.0004 mol $Cu(CF_3SO_3)_2$ in 20 ml acetonitrile, and the volume of solution was reduced to ~50 ml before being cooled in ice. Then 0.0005 mol $NaBPh_4$ in 10 ml ethanol was added and the solution was slowly evaporated to yield blue-green crystals in 30% yield. Anal. Calc. for $C_{89}H_{97}Cu_2B_2F_3N_8O_8S$: C, 65.9; H, 5.70; N, 7.10. Found: C, 64.8; H, 5.60; N, 7.00%.

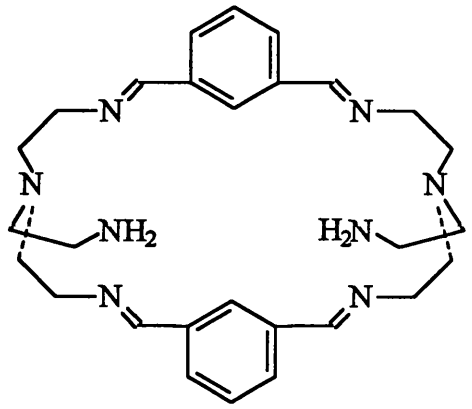

L3'

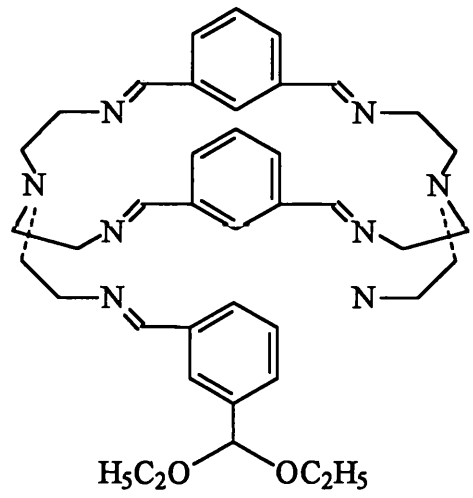

L3"

$[Cu_2L3(N_3)][O_3SCF_3]_3 \cdot 2H_2O$. 0.0005 mol **L3** dissolved in 30 ml ethanol was added to a solution containing 0.001 mol of $Cu(O_3SCF_3)_2$ in 30 ml acetonitrile and then 0.0005 mol of NaN_3 in 1 ml water was added to the above mixture. On evaporation of the solvent small golden crystals were obtained in 65% yield. Anal. Calc. for $C_{39}H_{46}Cu_2F_9N_{11}O_{11}S_3$: C, 37.5; H, 3.7; N, 12.3. Found: C, 37.3; H, 3.7; N, 12.3

RL3. This ligand was prepared in the same way as that described for **RL1** in 80% yield. ^1H NMR (CD_2Cl_2): 7.09 (s, 3H); 7.20 (m, 6H); 7.20 (m, 3H), 3.62 (s, 12H), 2.59 (m, 12H), 2.45 (m, 12H).

$[Cu_2$ **RL3**$][ClO_4]_2 \cdot H_2O$. To a deoxygenated solution of 0.0005 mol **RL3** in 50 ml ethanol was added 0.001 mol $Cu(MeCN)_4ClO_4$ in 30 ml deoxygenated acetonitrile. Ar was bubbled through the solution until plenty of white solid appeared. This product was filtered under Ar and collected in 52% yield. Anal. Calc. for $C_{36}H_{50}Cu_2Cl_2N_8O_9$: C, 45.9; H, 5.8; N, 11.9. Found: C, 46.1; H, 5.7; N, 12.0%.

$[Cu_2$**RL3**$(OH)][ClO_4]_3 \cdot 3H_2O$. To a solution of 0.0005 mol **RL3** in 30 ml ethanol was added a solution of 0.001 mol $Cu(ClO_4)_2 \cdot 6H_2O$ in 30 ml acetonitrile and a solution of 0.0005 mol pyrazole in 10 ml ethanol. The resulting mixture was stirred for one hour and left in air. Dark-green crystals were collected after two days. Yield 57%. Anal. Calc. for $C_{36}H_{55}Cu_2Cl_3N_8O_{16}$: C, 39.5; H, 5.6; N, 10.2. Found: C, 39.6; H, 5.5; N, 10.1%.

$[Cu_2$**RL3**$(N_3)][CF_3SO_3]_3 \cdot H_2O$. To a solution of 0.0005 mol **RL3** in 20 ml ethanol and 30 ml acetonitrile was added 0.001 mol $Cu(O_3SCF_3)_2$ in 30 ml ethanol and 0.0005 mol NaN_3 in 1 ml H_2O. The resulting solution was reduced to low volume and green crystals were obtained in 47% yield. Anal. Calc. for $C_{39}H_{50}Cu_2F_9N_{11}O_{10}S_3$: C, 38.0; H, 4.5; N, 12.5. Found: C, 37.9; H, 4.3; N, 12.3%.

$[Cu_2$**RL3**$(im)][ClO_4]_3$. 0.001 mol $Cu(ClO_4)_2 \cdot 6H_2O$ in 30 ml acetonitrile was added into a solution containing 0.0005 mol **RL3** and 0.0005 mol imidazole in 30 ml ethanol, whereupon a dark blue color developed. On standing, dark blue crystals were collected in 54% yield. Anal. Calc. for $C_{39}H_{45}Cu_2Cl_3N_{10}O_{12}$: C, 40.9; H, 5.5; N, 12.3. Found: C, 41.1; H, 5.2; N, 12.0%.

1,4,12,15,18,26,31,39,42,43,44-undecaazapentacyclo[13.13.13.$1^{6,10}$.$1^{20,24}$. $1^{33,37}$]-tetratetraconta4,6(7),8,10(42),11,18,20(21),22,24(43),25,31,33(34),35, 37(44),39-pentadecaene (**L4**),

1,4,12,15,18,26,31,39,42,43,44-undecaazapentacyclo[13.13.13.$1^{6,10}$.$1^{20,24}$. $1^{33,37}$]-tetratetraconta-6(7),8,10(42),20(21)22,24(43),33(34),35,37(44)-nonaene (**RL4**), and their copper(I)/(II) complexes.

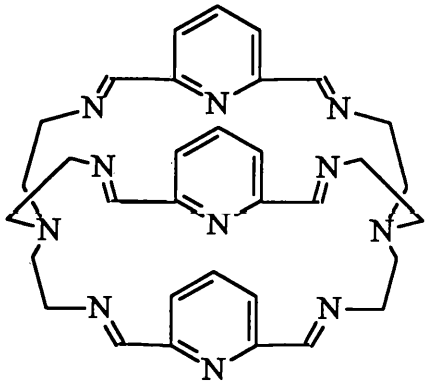

L4

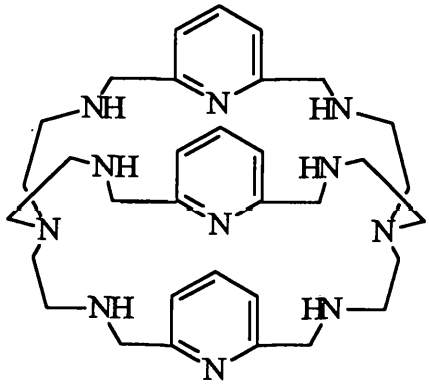

RL4

2,6-Diformyl Pyridine[71]

2,6-Dimethanol pyridine (19 g) and selenium dioxide (15 g) were dissolved in dioxan (300 ml) and the mixture was refluxed for four hours. The solution was filtered and evaporated to dryness to give the crude product of 2,6-diformyl pyridine. The creamy solid was obtained after recrystallisation from a chloroform/petroleum ether (40 – 60 °C) mixed solvent. Yield 77%.

L4. 0.003 mol 2,6-diformylpyridine was dissolved in 100 ml methanol before 0.002 mol tren in 30 ml methanol was added. The resulting solution was stirred for one hour at room temperature and then was filtered. The filtrate was evaporated to 15 ml and left in the freezer. The white crystalline product was obtained after several hours. Yield

67%. ^{1}H NMR ($CDCl_3$): 8.11 (tr, 3H); 7.81 (d, 6H); 7.59 (s, 6H), 3.57 (br s, 12H), 2.87 (s, 12H).

$[Cu_2L4]X_2 \cdot nCH_2Cl_2$ ($X = ClO_4^-$, $n = 2$; $X = BF_4^-$, $n = 0$). 0.0005 mol **L4** was dissolved in 30 ml deoxgenated CH_2Cl_2 at 30 °C. and a solution of 0.001 mol $Cu(MeCN)_4X$ in 10 ml deoxygenated acetonitrile was added with stirring. Black crystals were deposited on standing. Yield 54%.

$[Cu_2L4][ClO_4]_2 \cdot 2CH_2Cl_2$. . Anal. Calc. for $C_{35}H_{43}Cu_2Cl_6N_{11}O_8$: C, 38.7; H, 4.0; N, 14.2. Found: C, 38.7; H, 3.6; N, 14.2%.

$[Cu_2L4][BF_4]_2$. Anal. Calc. for $C_{33}H_{39}Cu_2B_2F_8N_{11}$: C, 44.5; H, 4.4; N, 17.3. Found: C, 44.7; H, 4.3; N, 16.9%.

$[Cu_2L4][BF_4]_3 \cdot 4H_2O$. 0.0003 mol $[Cu_2L4](BF_4)_2$ in 5 ml MeCN was treated with 0.0003 mol $FcBF_4$ and the solution was evaporated quickly to dryness. The brown product was thoroughly washed with $CHCl_3$ to remove ferrocene. Yield 80%. Anal. Calc. for $C_{33}H_{47}Cu_2B_3F_{12}N_{11}O_4$: C, 38.1; H, 4.5; N, 14.8. Found: C, 37.8; H, 4.4; N, 14.3%.

RL4. This ligand was prepared by the same method used in the preparation of **RL1**. ^{1}H NMR (CDCN): 7.05 (tr, 3H); 7.47 (d, 6H); 3.86 (s, 12H), 2.62 (q, 24H).

$[Cu_2RL4][ClO_4]_4 \cdot 4H_2O$. To a solution of 0.0005 mol **RL4** in 50 ml ethanol was added a solution of 0.001 mol $Cu(ClO_4)_2 \cdot 6H_2O$ in 30 ml acetonitrile. The mixture was stirred for half an hour and was left standing. The bright blue powder was collected next day in 77% yield. Blue microcrystals were obtained by recrystallisation from 1:1 ethanol/acetonitrile Anal. Calc. for $C_{33}H_{53}Cu_2Cl_4N_{11}O_{20}$: C, 33.2; H, 4.4; N, 12.9. Found: C, 33.0; H, 4.4; N, 12.7%.

$[Cu_2$**RL4**$(N_3)][ClO_4]_3 \cdot 3H_2O$. 0.0005 mol **RL4** was dissolved in 50 ml ethanol before 0.001 mol $Cu(ClO_4)_2 \cdot 6H_2O$ in 30 ml acetonitrile and 0.0005 mol NaN_3 in 1 ml H_2O were added. The mixture was stirred for half an hour and left for standing. Green crystals were obtained in 40% yield. Anal. Calc. for $C_{33}H_{51}Cu_2Cl_3N_{14}O_{15}$: C, 35.3; H, 5.1; N, 17.5. Found: C, 35.1; H, 4.8; N, 17.2%.

1,4,11,14,17,24,29,36,39,30,41-undecaazapentacyclo[12.12.12.$1^{6,9}$.$1^{19,22}$.$1^{31,34}$]-hentetraconta 4,6,8,10,17,19,21,23,29,31,33,35-dodecaene (**L5**), 1,4,11,14,17,24,29,36,39,40,41-undecaazapentacyclo[12.12.12.$1^{6,9}$.$1^{19,22}$. $1^{31,34}$]-hentetraconta 6,8,19,21,31,33 -hexaene (**RL5**), and their copper(I)/(II) complexes.

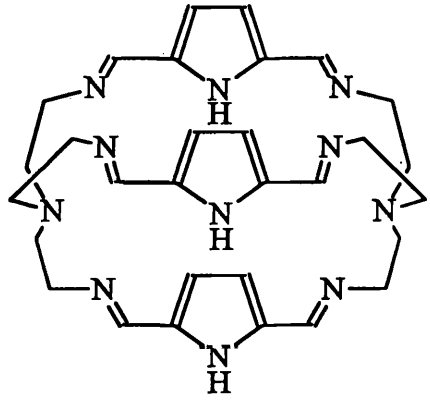

L5

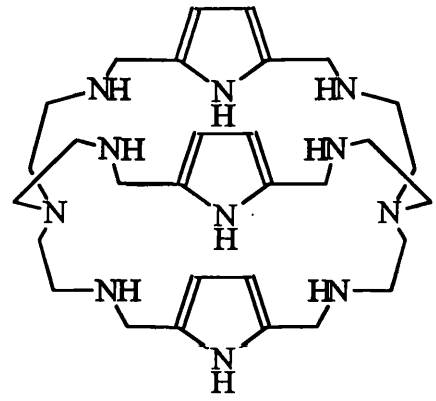

RL5

2,5- Diformyl Pyrrole[72]

Step 1: Preparation of pyrrole-2-carboxaldehyde

DMF (36 g, 0.50 mol) was maintained at 10-20 °C with an ice-water bath while being mechanically stirred. Phosphorous oxychoride (76g, 0.50 mol) was added over 15 minutes. On addition the mixture was stirred at room temperature for 15 minutes. The ice bath was reused and 1,2-dichloroethane (112ml) was added. When T=5 °C a solution of pyrrole (30 g, 0.45 mol) in 1,2-dichloroethane (112 ml) was added to the stirred cooled mixture over one hour. The mixture was then refluxed for 15 minutes (HCl evolved). After cooling to 25-30 °C, sodium acetate (336 g, 2.46 mol) in 490 ml H_2O was added cautiously at first (to destroy unused $POCl_3$) and then as quickly as possible.

The two phases were stirred vigorously and refluxed for 15 minutes. On cooling, the organic layer was separated from the aqueous layer, which was then extracted with 3 × 230 ml diethylether. Saturated Na_2CO_3 solution (45 ml) was added carefully (CO_2 evolved) to the organic layer, which was then separated and washed twice with water before being left overnight over anhydrous Na_2CO_3. The solvent was removed under reduced pressure and the residual oil was cooled on ice bath and scratched to crystallise golden brown pyrrole 2-carboxaldehyde (yield: 92%).

Step 2: Preparation of ethyl α-cyano-2-pyrrole-acrylate.

A solution of pyrrole-2-carboxaldehyde (63 g, 0.66 mol), ethyl cyanoacetate (106.1 g, 0.33 mol) and diethylamine (4.7 g, 0.07 mol) in 830 ml of toluene (dried 24 hours over $CaCl_2$) was refluxed for one hour in a Dean-Stark water separator. After cooling ethyl α-cyano-2-pyrrole-acrylate, an orange-brown coloured powder, was filtered and washed with 50-70° petroleum ether and air-dried (yield: 87%).

Step 3: Preparation of ethyl α-cyano-5-formyl-2-pyrrole-acrylate.

DMF (34.1 g) and phosphorous oxychoride (70.8 g) were combined as in Step.1. After stirring at room temperature for 15 minutes 1,2-dichloroethane (215 ml) was added. The flask was then cooled in an ice-water bath (~ 5°C) before a suspension of ethyl α-cyano-2-pyrrole-acrylate (72.7 g) in 320 ml 1,2-dichloroethane was added over 30 minutes. The resulting suspension was refluxed for 15 minutes and cooled to 25-30 °C. Aqueous 4 M sodium acetate (195 g in 590 ml H_2O) was added over 5 minutes to the vigorously stirred mixture which was then refluxed for another 15 minutes. The resulting brown solution was cooled and then left overnight at room temperature. The

brown ethyl α-cyano-5-formyl-2-pyrrole-acrylate was collected by filtration the following day (yield: 77%).

Sept 4: Preparation of 2,5-diformyl pyrrole

Ethyl α-cyano-5-formyl-2-pyrrole-acrylate (42.5 g) was refluxed in 3M aqueous NaOH (780 ml) for 2 hours. The brown solution was allowed to cool to below 20 °C and then slowly acidified with 2 M H_2SO_4 to pH 4.5. Extraction with 780 ml of ethylacetate gave an orange solution. The small amount of black surface layer was removed by decantation. The ethylacetate was evaporated under reduced pressure to leave orange brown 2,5-diformyl pyrrole in 75% yield. Decolourisation with charcoal was followed by recrystallisation from toluene to give a light brown product.

$[Cu_2L5][BF_4]_2$. 0.003 mol 2,5-diformyl pyrrole was dissolved in 50 ml ethanol at 30 °C before 0.003 mol tren in 20 ml ethanol was added. After bubbling N_2 through the mixture for 30 minutes 0.002 mol $Cu(MeCN)_4BF_4$ in 30 ml deoxygenated MeCN was added. An orange precipitate was isolated in 60% yield. Anal. Calc. for $C_{30}H_{39}Cu_2B_2F_8N_{11}$: C, 42.2; H, 4.6; N, 18.0. Found: C, 42.6; H, 4.3; N, 18.1%.

$[Cu_2(L5\text{-}H)][BF_4]_2 \cdot H_2O$. To a suspension of 0.001 mol $[Cu_2L5][BF_4]_2$ in 400 ml 3:1 acetonitrile/ethanol was added 0.001 mol $FcBF_4$ in solid form. The mixture was refluxed for one hour during which time all solids were dissolved. The resulting solution was filtered and evaporated to dryness. The yellow-green product was thoroughly washed with $CHCl_3$ to remove ferrocene. Yield 53%. Anal. Calc. for $C_{30}H_{40}Cu_2B_2F_8N_{11}O$: C, 41.3; H, 4.5; N, 17.7. Found: C, 41.0; H, 4.3; N, 17.5%.

$[Cu_2(L5\text{-}3H)][ClO_4] \cdot H_2O$. 0.002 mol $AgClO_4$ in 20 ml ethanol was added into a suspension of 0.001 mol $[Cu_2L5][BF_4]_2$ in 300 ml acetonitrile. The mixture was refluxed

for one hour during which time the cloudiness disappeared and a silver mirror formed. The solution was filtered and the volume was reduced to 25 ml. An equal volume of ethanol was added and the resulting solution was kept in the freezer. Black crystals were collected next day in 50% yield. Anal. Calc for $C_{30}H_{38}Cu_2ClN_{11}O_5$: C, 45.3; H, 4.8; N, 19.3. Found: C, 45.2; H, 4.4; N, 19.4%.

$[Cu_2(\mathbf{L5\text{-}3H})][BF_4]$. This product was obtained from the air-oxidation of $[Cu_2\mathbf{L5}][BF_4]_2$, which was left in air for over one month. Anal. Calc. for $C_{30}H_{36}Cu_2BF_4N_{11}$: C, 46.9; H, 5.1; N, 20.1. Found: C, 46.9; H, 4.6; N, 20.0%.

RL5. This ligand was prepared by the same method used in the preparation of **RL1**. ^{1}H NMR (CDCN): 7.05 (tr, 3H); 7.47 (d, 6H); 3.86 (s, 12H), 2.62 (q, 24H).

$[Cu_2\mathbf{RL5}(OH)][ClO_4]_3 \cdot H_2O$. 0.0005 mol **RL5** was dissolved in 30 ml ethanol before 0.001 mol $Cu(ClO_4)_2 \cdot 6H_2O$ in 20 ml acetonitrile was added. The solution was stirred at 50 °C for 30 minutes and left in air for 24 hours. The pale green powder was collected in 61% yield. Anal. Calc. for $C_{30}H_{48}Cu_2Cl_3N_{11}O_{14}$: C, 35.1; H, 5.3; N, 15.0. Found: C, 35.2; H, 5.2; N, 15.0%.

$[Cu_2\mathbf{RL5}(N_3)][ClO_4]_3 \cdot 4H_2O$. 0.0005 mol **RL5** and 0.001 mol $Cu(ClO_4)_2 \cdot 6H_2O$ were dissolved in 50 ml 1:1 ethanol/acetonitrile. To this solution was added 0.0005 mol NaN_3 in 1 ml H_2O. A brown powder was isolated after one hour in 67% yield. . Anal. Calc. for $C_{30}H_{53}Cu_2Cl_3N_{14}O_{16}$: C, 32.6; H, 5.3; N, 17.7. Found: C, 32.6; H, 4.8; N, 17.5%.

2.2. Crystallography

$[Cu_2\mathbf{L1}][O_3SCF_3]_2$. Crystal Data. $C_{32}H_{36}Cu_2F_6N_8O_6S_5$, M = 1030.07, orange plate, crystal dimensions 0.9 × 0.42 × 0.12 mm, orthorhombic, space group *Pcca*, *a* =

28.464(5), b = 15.616(4), c = 18. 459(2) Å, U = 8205(3) Å^3, μ = 1.372 mm^{-1}, Dc = 1.67 g cm^{-3}, Z = 8, F(000) =4192.

Data were collected at 133 K on a Siemens P4 four-circle diffractometer with graphite-monochromated Mo-Kα radiation (λ = 0.71073 Å). By using 1.4° φ scan at 7° min^{-1}, 4593 unique reflections were collected in the range of 4 < 2θ < 45°. Unit-cell parameters were determined by non-linear least-squares refinement of 40 accurately centred reflections (10 < 2θ < 25°). The data were corrected for Lorentz-polarisation effects and an empirical absorption correction was applied based on φ-scan data (T_{max} = 1.00, T_{min} = 0.821).

The structure was solved by direct methods[73] which revealed most of the non-hydrogen atoms and the remaining atoms were located from Fourier-difference maps. All non-hydrogen atoms were refined with anisotropic atomic displacement parameters. Hydrogen atoms were inserted at calculated positions using a riding model with common, fixed isotropic thermal parameters. All the data were used for refinement of 533 parameters on F2 which converged with $wR2$ = 0.2078, goodness of fit = 0.970 (all data) and conventional R1 = 0.0726 [for I > 2σ(I)]. The final difference map showed no significant residual electron density except for two peaks of ca. 1.8 e Å^{-3} close to Cu(1) which are dependent on the parameters used for the (thin plate) absorption correction[74]. All programs used on the structure refinement are contained in the SHELXL 93[75] package. Final atomic coordinates are given in Table 2.1.

Table 2.1 Atomic coordinates ($\times 10^4$) for complex $[Cu_2L1][O_3SCF_3]_2$

	x	y	z
Cu1	6707(4)	5453(7)	1313(5)
N1	5843(4)	5920(6)	1325(4)
C1	5857(4)	6819(7)	1401(6)
C2	6301(4)	7209(7)	1028(6)
N11	6719(3)	6849(7)	1325(4)
C3	6968(4)	7379(8)	1714(6)
C4	7423(4)	7137(7)	2057(6)
C5	7689(4)	7639(8)	2492(6)
C6	8105(5)	7247(8)	2730(6)
C7	8148(4)	6441(7)	2445(6)
S1	7680(10)	6163(2)	1898(15)
C8	8521(4)	5863(8)	2608(6)
N12	8595(3)	5130(6)	2313(5)
C9	8992(4)	4600(8)	2564(6)
C10	9364(4)	4529(8)	1957(6)
C11	5654(4)	5616(8)	640(6)
C12	5884(4)	4798(8)	392(7)
N13	6399(3)	4897(6)	305(6)
C13	6583(4)	4858(7)	333(6)
C14	7064(4)	4942(7)	485(6)
S2	7500	5000	161(2)
Cu2	6657(4)	169(6)	11491(5)
N2	9220(4)	-357(7)	1150(6)
C21	9390(4)	214(8)	576(7)
C22	9046(4)	208(9)	-83(7)
N21	8578(3)	509(7)	139(6)
C23	8409(4)	1161(8)	235(7)
C24	7974(4)	1570(7)	80(6)
C25	7844(4)	2317(8)	380(6)
C26	7396(5)	2614(8)	139(6)
C27	7184(4)	2044(8)	341(6)
S3	7548(11)	1179(2)	503(15)
C28	6739(4)	2167(8)	695(7)
N22	6539(3)	1604(7)	1072(5)
C29	6067(4)	1803(8)	1358(7)
C30	5688(5)	1254(8)	1018(8)
C31	9382(5)	-89(10)	1868(7)
C32	9080(5)	648(9)	2150(8)
N23	8582(4)	395(7)	2202(6)
C33	8385(5)	399(8)	2834(7)
C34	7924(5)	203(7)	2993(6)
C35	7736(5)	118(9)	3665(6)

(continued)

C15	7250(5)	4970(9)	1157(6)
S4	7500	0000	2334(2)
C40	4459(6)	7420(9)	1101(8)
F41	4563(4)	7336(7)	430(6)
F42	4688(3)	8079(7)	1342(7)
F43	4599(3)	6737(6)	1458(5)
S40	3814(12)	7560(2)	1210(2)
O41	3757(3)	7622(6)	1976(4)
O42	3622(3)	6801(5)	891(5)
O43	3720(3)	8330(5)	825(4)
C50	4757(6)	3254(13)	1405(10)
F51	4852(4)	3936(9)	876(8)
F52	5154(3)	2926(9)	1518(8)
F53	4627(3)	3683(6)	1987(5)
S50	4302(12)	2599(3)	1032(2)
O51	3925(3)	3192(6)	913(4)
O52	4509(3)	2254(7)	396(5)
O53	4216(4)	2026(7)	1613(5)

$[Cu_2L2][BF_4]_2$. Crystal data. $C_{30}H_{36}Cu_2B_2F_8N_8O_3$, M = 857.39, red block, crystal dimensions 0.52 × 0.22 × 0.20 mm, monoclinic, space group $P2_1/c$, a = 11.776(3), b = 22.375(6), c = 13.449(4) Å, β = 97.20 °, U = 3529(2) Å^3, μ = 1.29 mm^{-1}, Dc = 1.614 g cm^{-3}, Z = 4, F(000) = 1760.

Data were collected at 198 K on a Nicolet R3m four-circle diffractometer with graphite-monochromated Mo-Kα radiation. By using 1.6° φ scan at 4.88° min^{-1}, 4871 unique reflections were collected in the range of 4 < 2θ < 45°. Of these, 4610 were unique and 3280 reflections having F > 6σ (F) were used in the refinement. Unit-cell parameters were determined by non-linear least-squares refinement of 25 accurately centred reflections (4 < 2θ < 33°). The data were corrected for Lorentz-polarisation effects and an empirical absorption correction was applied based on φ-scan data (T_{max} = 1.00, T_{min} = 0.821).

The structure was solved by direct methods that revealed all the non-hydrogen atoms. It was refined by full-matrix least-squares techniques. All the non-hydrogen atoms were refined with anisotropic atomic displacement parameters. Hydrogen atoms were inserted at calculated positions, using a riding model with common, fixed isotropic thermal parameters. The refinement, in 482 parameters, converged with R = 0.035 and R' = 0.043. The function minimised in the refinement was $\Sigma w(Fo\text{-}Fc)^2$ where w = $[\sigma^2(Fo) + 0.0006\,Fo^2]^{-1}$. The final difference map showed no residual electron density greater than ± 0.5 e $Å^{-3}$. All programs used in data reduction, structure solution and refinement are contained in the SHELXTL-PC package[76]. Final coordinates are given in Table 2.2.

Table 2.2 Atomic coordinates (× 10^4) for complex $[Cu_2L2][BF_4]_2$

	x	y	z
Cu1	6959(1)	9845(1)	2240(1)
Cu2	8360(1)	11294(1)	832(1)
N1	6290(3)	8990(2)	3051(3)
N2	9082(3)	12118(2)	-39(3)
C1	5981(4)	9249(2)	3976(3)
C2	6745(4)	9785(2)	4299(3)
N3	6631(5)	10241(2)	3494(3)
C3	6220(4)	10741(2)	3720(3)
C4	5943(4)	11235(2)	3048(3)
C5	5256(4)	11712(2)	3161(4)
C6	5171(4)	12032(2)	2257(4)
C7	5829(4)	11746(2)	1651(2)
O1	6312(3)	11243(1)	2121(3)
C8	6082(4)	11911(2)	671(3)
N4	6895(3)	11681(2)	244(3)
C9	7068(4)	11952(2)	-725(3)
C10	8045(4)	12402(2)	-559(3)
C11	5314(4)	8782(2)	2358(3)
C12	4823(4)	9303(2)	1709(3)
N5	5753(3)	9560(2)	1191(3)
C13	5758(4)	9407(2)	275(3)
C14	6607(4)	9566(2)	-347(3)

(continued)

C15	6781(4)	9346(2)	-1250(3)
C16	7767(4)	9627(2)	-1512(3)
C17	8128(4)	10014(2)	-766(3)
O2	7431(3)	9985(1)	-26(2)
C18	9078(4)	10424(2)	-690(3)
N6	9280(3)	10845(2)	-56(3)
C19	10272(3)	11231(2)	-212(4)
C20	9812(3)	11816(2)	-691(3)
C21	7271(3)	8579(2)	3177(3)
C22	8076(3)	8709(2)	2397(3)
N7	8404(3)	9348(2)	2468(3)
C23	9373(4)	9458(2)	2985(3)
C24	9834(4)	10040(2)	3220(3)
C25	10716(4)	10191(2)	3909(3)
C26	10807(4)	10821(2)	3886(3)
C27	9985(4)	11013(2)	3165(3)
O3	9362(3)	10543(1)	2739(2)
C28	9786(4)	11610(2)	2799(3)
N8	9152(3)	11757(2)	1991(3)
C29	9150(5)	12397(2)	1720(3)
C30	9693(4)	12476(2)	761(3)
B1	7530(5)	3833(3)	1378(5)
F1	6797(3)	3357(1)	1187(3)
F2	8250(3)	3864(1)	637(2)
F3	6921(3)	4361(1)	1385(2)
F4	8200(3)	3762(2)	2283(2)
B2	3013(6)	2471(3)	4651(5)
F5	2756(3)	2979(2)	5125(3)
F6	2064(3)	2114(2)	4505(3)
F7	3336(4)	2622(2)	3726(3)
F8	3906(3)	2163(1)	5172(2)
O4	2125(8)	1858(4)	2125(6)

$[Cu_2$**RL2**$(OH)][O_3SCF_3]_3 \cdot H_2O$. Crystal data. $C_{33}H_{51}Cu_2F_9N_8O_{14}S_3$, M = 1178.13, green block, crystal dimensions 0.56 × 0.42 × 0.30 mm, monoclinic, space group $P2_1/n$, a = 12.434(3), b = 16.919(4), c = 22.300(4) Å, β = 92.23°, U = 4688(2) Å^3, μ = 1.147 mm^{-1}, Dc = 1.669 g cm^{-3}, Z = 4, F(000) = 2416.

Data were collected at 143 K on a Siemens P4 four-circle diffractometer with graphite-monochromated Mo-Kα radiation. Unit-cell parameters were determined by non-linear least-squares refinement of 27 accurately centred reflections ($18 < 2\theta < 25°$). By using a 2° φ scan at 5° min^{-1}, 7273 reflection were collected in the range of $4 < 2\theta < 47°$. 6914 unique reflections were used in the refinement.

The structure was solved by direct methods[76] which revealed most of the non-hydrogen atoms. The remaining atoms were located from Fourier-difference maps. The solvated water molecule was disordered and this was modelled with 50% occupancy of each of the two sites. All non-hydrogen atoms, other than those in the disordered water molecule, were assigned anisotropic thermal parameters. Hydrogen atoms were inserted at calculated positions with common fixed isotropic thermal parameters except for those on the water molecule and the central hydroxo bridge, which were not included. All the data were used for refinement on F^2 which converged with $wR2 = 0.168$ (all data), goodness of fit = 1.065 and conventional R1 = 0.0596 [$I > 2\sigma(I)$] for 611 parameters. The function minimised in the refinement was $wR2 = \{\Sigma[w\,(Fo^2-Fc^2)^2]/\,\Sigma(wFo^2)\}^{1/2}$, where $w = [\sigma^2(Fo^2) + (0.078\,P^2+15\,P)^2]^{-1}$ and $P = 1/3[\,\max(0, Fo^2) + 2/3\,Fc^2$. The final difference map showed no significant residual electron density. All programs used in the structure refinement are contained in the SHELXL 93[78] package. Final coordinates are given in Table 2.3.

Table 2.3 Atomic coordinates (× 10^4) for complex $[Cu_2RL2(OH)][O_3SCF_3]_3$

	x	y	z
Cu1	3987(1)	8322(1)	1692(1)
Cu2	3805(1)	8282(1)	3434(1)
O1	3918(4)	8244(3)	2565(2)

(continued)

N1	4094(4)	8368(3)	766(2)
N2	686(5)	8299(3)	4359(2)
C1	4759(5)	7683(4)	569(3)
C2	5637(5)	7495(4)	1050(3)
N3	5122(4)	7351(3)	1630(2)
C3	4748(7)	6520(4)	1691(3)
C4	4396(8)	6328(4)	2302(3)
C5	4854(8)	5909(4)	2768(3)
C6	4129(8)	5955(4)	3243(3)
C7	3284(8)	6392(4)	3058(3)
O2	3410(4)	6624(3)	2463(2)
C8	2328(6)	6705(4)	3358(3)
N4	2336(4)	7579(3)	3450(2)
C9	1880(6)	7810(4)	4032(3)
C10	2768(6)	7786(4)	4518(3)
C11	4601(5)	9139(4)	609(3)
C12	4315(5)	9767(4)	1063(3)
N5	4691(4)	9478(3)	1669(2)
C13	5881(5)	9631(4)	1770(3)
C14	6412(5)	9042(4)	2167(3)
C15	7215(6)	8523(4)	2089(3)
C16	7337(6)	8068(5)	2626(3)
C17	6590(6)	8341(4)	3004(3)
O3	6017(3)	8957(3)	2735(2)
C18	6305(6)	8117(5)	3620(3)
N6	5277(5)	7660(3)	3645(2)
C19	5158(7)	7341(4)	4259(3)
C20	4708(6)	7992(4)	4649(3)
C21	2983(5)	8308(4)	481(3)
C22	2328(5)	7755(4)	856(3)
N7	2339(4)	8063(3)	1485(2)
C23	1526(5)	8701(4)	1531(3)
C24	1403(5)	8987(4)	2149(3)
C25	630(6)	8902(4)	2550(4)
C26	1000(6)	9297(4)	3084(3)
C27	1985(5)	9595(4)	2987(3)
O4	2239(3)	9422(2)	2401(2)
C28	2786(5)	10018(4)	3361(3)
N8	3781(4)	9537(3)	3512(2)
C29	4162(5)	9676(4)	4149(3)
C30	3513(6)	9142(4)	4543(2)
S1	7744(2)	9382(1)	208(1)
O5	7333(5)	8656(4)	412(3)
O6	7102(5)	10048(3)	435(3)

(continued)

O7	8008(4)	9477(4)	-405(2)
C31	9025(10)	9515(9)	615(4)
F1	9631(5)	8868(5)	412(3)
F2	9442(5)	10222(5)	530(3)
F3	8853(5)	9471(6)	1214(2)
S2	-10(2)	6517(1)	2124(1)
O8	727(5)	6821(4)	1712(4)
O9	-336(5)	7058(4)	2586(3)
O10	237(4)	5731(3)	2325(2)
C32	-1231(8)	6394(6)	1656(4)
F4	-2044(4)	6157(4)	1985(3)
F5	-1118(4)	5839(4)	1235(2)
F6	-1532(5)	7065(4)	1390(3)
S3	7042(1)	4070(1)	166(1)
O11	6781(5)	3306(3)	415(2)
O12	6592(4)	4215(3)	-435(2)
O13	8145(3)	4313(3)	267(2)
C33	6296(6)	4753(5)	627(3)
F7	5250(4)	4605(4)	605(2)
F8	6445(4)	5502(3)	465(2)
F9	6633(4)	4687(3)	1213(2)
O14	5752(6)	2045(5)	1126(3)
O15	7776(8)	1269(6)	1323(5)

$[Cu_2$**L3"**$(OH)][BPh_4]_2[O_3S\,CF_3]\cdot H_2O\cdot 0.5EtOH$. Crystal data. $C_{90}H_{96}Cu_2B_2F_3N_8O_6S$, M = 1623.54, blue-green hexagonal plate, crystal dimensions 0.7 × 0.4 × 0.06 mm, monoclinic, space group $P2_1/a$, a = 17.1866(11), b = 17.505(8), c = 26.348(11) Å, β = 91.48(4)°. U = 8235(7) Å^3, Dc = 1.309 g cm^{-3}, Z = 4, F(000) = 3404.

Data were collected at 193 K on a Nicolet R3m four-circle diffractometer with graphite-monochromated Mo-Kα radiation. By using a 1.8° φ scan at 4.2° min^{-1}, 10215 reflections were collected in the range $4 < 2\theta < 50°$ and 9850 unique reflections were used in the refinement. The data were of poor quality, with only 4087 reflections having $I > 2\sigma(I)$. An empirical absorption correction was applied (T_{max} = 0.967, T_{min} = 0.602)

and the structure was solved by direct methods[76] which revealed most of the structure of the cation and the BPh_4^- anions. The triflate anion was severely disordered and was inserted with constrained geometry and there was some residual electron density in this region. The ethanol solvate molecule was also disordered about a centre of symmetry. Hydrogen atoms were inserted at calculated positions on the cation and BPh_4^- anions. The non-hydrogen atoms of the cation were refined with anisotropic atomic displacement parameters, except for the carbons of the acetal groups. All the data were used for refinement on F^2 which converged with conventional $R1 = \Sigma || Fo | - | Fc || / \Sigma | Fo | = 0.119$, $wR2 = \{\Sigma[w(Fo^2 - Fc^2)^2] / \Sigma[w\text{-}(Fo^2)^2]\}^{1/2} = 0.275$, $[I > 2\sigma(I)]$, $w = [\sigma^2(Fo^2) + (aP)^2]^{-1}$ where $P = 1/3[\max(0, Fo^2) = 2/3Fc^2]$, goodness of fit = 0.978 for 155 parameters. All programs used in the structure refinement are contained in the SHELXL 93 package[78]. Final coordinates are given in Table 2.4.

Table 2.4 Atomic coordinates ($\times 10^4$) for complex $[Cu_2L3"(OH)][BPh_4]_2[O_3SCF_3]\cdot H_2O\cdot 0.5EtOH$

	x	y	z
Cu1	1877(1)	366(1)	1819(1)
Cu2	2878(1)	23(1)	3129(1)
O1	2306(5)	300(5)	2503(4)
N1	3205(7)	-50(8)	3909(5)
N2	1287(6)	760(6)	1182(4)
C1	4022(9)	-291(10)	3934(7)
C2	4167(8)	-896(10)	3543(6)
N3	3991(7)	-628(7)	3027(5)
C3	4375(9)	-877(10)	2664(7)
C4	4289(8)	-654(8)	2145(7)
C5	4675(9)	-1063(10)	1796(8)
C6	4652(9)	-858(9)	1284(7)
C7	4226(8)	-221(9)	1116(6)

(Continued)

C8	3798(8)	170(7)	1471(6)
C9	3831(7)	-47(8)	1978(6)
C10	3348(8)	806(8)	1297(6)
N4	2726(6)	996(6)	1498(4)
C11	2318(7)	1681(7)	1270(6)
C12	1722(8)	1362(8)	929(6)
C13	2745(9)	-621(10)	4161(5)
C14	2032(9)	-795(9)	3836(5)
N5	2298(6)	-947(7)	3311(5)
C15	2335(7)	-1645(8)	3169(5)
C16	2626(8)	-1855(8)	2666(6)
C17	3081(8)	-2488(8)	2627(6)
C18	3316(10)	-2714(9)	2163(7)
C19	3120(10)	-2308(9)	1727(6)
C20	2659(7)	-1672(7)	1774(5)
C21	2415(8)	-1445(7)	2244(5)
C22	2400(8)	-1272(9)	1301(5)
N6	2072(5)	-640(6)	1290(4)
C23	1806(7)	-374(7)	778(5)
C24	1122(7)	125(7)	830(5)
C25	3110(10)	743(11)	4097(8)
C26	3409(12)	1344(11)	3736(8)
N7	3149(9)	1133(7)	3192(5)
C27	609(7)	1102(7)	1409(5)
C28	244(7)	551(7)	1756(5)
N8	829(6)	216(6)	2087(4)
C29	653(9)	-59(9)	2500(6)
C30	-120(10)	-110(10)	2755(6)
C31	-77(11)	-197(12)	3282(8)
C32	-770(14)	-190(14)	3553(9)
C33	-1444(11)	-146(11)	3295(8)
C34	-1469(10)	-110(10)	2790(7)
C35	-807(9)	-119(9)	2528(7)
C36	-2252(13)	56(9)	2564(8)
O2	-2300(9)	-437(9)	2154(6)
C37	-3110(14)	-379(14)	1851(10)
C38	-3123(18)	-1086(18)	1559(12)
O3	-2209(10)	772(10)	2293(7)
C39	-2359(17)	1500(16)	2632(12)
C40	-1622(27)	1867(28)	2720(21)
B1	369(8)	-2512(8)	-37(5)
C41	-383(7)	-2866(7)	-305(5)
C42	-411(9)	-3012(8)	-825(6)

(continued)

C43	-1019(9)	-3364(8)	-1086(6)
C44	-1631(9)	-3547(8)	-815(6)
C45	-1663(8)	-3408(8)	-332(6)
C46	-1024(7)	-3072(7)	-62(5)
C47	218(7)	-2181(6)	551(5)
C48	-425(7)	-1730(6)	631(5)
C51	577(8)	-1983(7)	1445(5)
C52	681(8)	-2301(7)	958(5)
C53	996(6)	-3215(6)	36(4)
C54	1762(7)	-3088(7)	95(5)
C55	2265(8)	-3688(8)	202(5)
C56	2023(9)	-4394(8)	261(6)
C57	1274(7)	-4569(8)	215(5)
C58	784(7)	-3973(7)	90(5)
C59	718(7)	-1816(7)	-374(5)
C60	655(7)	-1041(6)	-253(5)
C61	947(7)	-468(7)	-551(5)
C62	1312(7)	-629(7)	-980(5)
C63	1396(8)	-1379(8)	-1111(6)
C64	1125(7)	-1959(7)	-809(5)
B2	3426(10)	1460(10)	5718(7)
C65	3257(9)	535(9)	5808(6)
C66	3698(11)	63(11)	6138(7)
C67	3549(12)	-725(12)	6201(8)
C68	2943(12)	-1052(13)	5944(8)
C69	2538(12)	-628(12)	5612(8)
C70	2679(11)	159(10)	5546(8)
C71	2581(8)	1852(8)	5623(6)
C72	2317(9)	2168(9)	5159(6)
C73	1615(10)	2486(10)	5101(7)
C74	1139(10)	2507(9)	5496(6)
C75	1347(9)	2185(8)	5945(7)
C76	2076(8)	1874(8)	6009(6)
C77	3786(9)	1847(8)	6256(6)
C78	3581(8)	1585(8)	6746(6)
C79	3867(8)	1973(8)	7189(6)
C80	4338(10)	2581(9)	7154(7)
C81	4564(9)	2843(9)	6700(6)
C82	4293(8)	2467(8)	6251(6)
C83	3990(8)	1602(8)	5267(5)
C84	4495(8)	1046(9)	5103(6)
C85	4991(8)	1168(8)	4717(6)
C86	4997(9)	1846(9)	4483(6)
C87	4545(9)	2439(9)	4607(6)

(continued)

C88	4042(9)	2292(9)	5005(6)
S1	1013(17)	2073(8)	2831(8)
O4	1705(14)	1848(14)	2582(9)
O5	228(24)	1713(32)	2706(19)
O6	902(21)	2937(18)	2954(13)
C89	1184(14)	1699(14)	3423(9)
F1	1240(11)	928(11)	3417(8)
F2	1588(17)	2058(16)	3762(11)
F3	347(17)	1790(17)	3679(11)
O7	454(19)	-496(19)	4816(13)
C90	-217(19)	-726(18)	4981(13)
C91	684(22)	318(23)	4820(15)
O8	4678(25)	1546(25)	2598(17)
C91B	-684(22)	-318(23)	5180(13)
C90B	217(19)	726(18)	5019(12)
O7B	-454(19)	496(19)	5184(13)

$[Cu_2$**RL3**(im)$][ClO_4]_3$. Crystal data. $C_{39}H_{57}Cu_2Cl_3N_{10}O_{12}$, M = 1091.40, dark-blue hexagonal prism, monoclinic, space group $P2_1/c$, a = 15.280(8), b = 20.099(12), c = 18.016(11) Å, β = 112.22(4)°, U = 5121(75) Å^3, Z = 4, Dc = 1.415 g m^{-3}, μ = 10.5 cm^{-1}, F(000) = 2264.

The crystals were structurally unstable unless sealed in capillaries or with varnish. Data were collected on a Siemens P3/V2000 diffractometer, with graphite-monochromated Mo-Kα radiation . 4799 unique reflections were used in the refinement. The structure was solved by direct methods[76] and the refinement [78] converged with $R1$ = 0.15, goodness of fit = 1.01 for 3052 reflections with $Fo > 4\sigma(Fo)$. Final coordinates are given in Table 2.5.

Table 2.5 Atomic coordinates (× 10^4) for complex $[Cu_2$**L3**(im)$][ClO_4]_3$

	x	y	z
Cu1	6057(2)	2597(1)	5807(1)
Cu2	2021(2)	1885(1)	4955(2)

(continued)

Cl1	2236(4)	-530(3)	6473(4)
Cl2	6433(8)	4221(5)	3787(4)
Cl3	678(6)	1864(6)	2148(5)
O1	2028(17)	-1194(7)	6471(14)
O2	1736(17)	-182(12)	6840(14)
O3	1974(15)	-312(11)	5697(9)
O4	3181(10)	-430(12)	6882(13)
O5	7145(16)	4477(13)	4436(11)
O6	6079(15)	3656(9)	4004(12)
O7	6744(17)	4071(11)	3189(12)
O8	5714(17)	4683(11)	3504(17)
O9	852(16)	1803(11)	1458(10)
O10	76(15)	1371(11)	2180(13)
O11	1504(13)	1833(15)	2802(11)
O12	254(20)	2472(10)	2139(18)
N1	7462(12)	2774(9)	6212(9)
N2	694(14)	1595(10)	4760(10)
N3	5932(12)	3635(8)	5677(10)
N4	1361(13)	2769(8)	4422(11)
N5	6339(13)	1901(9)	5048(9)
N6	2214(12)	880(9)	4730(10)
N7	6386(12)	2239(9)	7069(8)
N8	2116(12)	1951(9)	6269(9)
N9	4713(13)	2453(8)	5251(9)
N10	3236(13)	2171(8)	4923(10)
C1	7603(17)	3468(12)	6062(13)
C2	6862(16)	3907(13)	6170(13)
C3	5180(15)	4016(11)	5849(11)
C4	4227(16)	3983(10)	5187(13)
C5	4063(21)	4222(10)	4426(16)
C6	3222(23)	4220(11)	3846(16)
C7	2458(20)	3964(11)	3966(14)
C8	2546(22)	3726(11)	4685(16)
C9	3434(21)	3747(10)	5283(14)
C10	1753(18)	3434(14)	4840(16)
C11	322(21)	2705(14)	4238(16)
C12	43(17)	2023(14)	4114(17)
C13	7918(16)	2309(12)	5811(13)
C14	7246(16)	2169(12)	4982(14)
C15	6391(17)	1174(10)	5207(13)
C16	5615(20)	918(9)	5426(12)
C17	5807(18)	710(11)	6201(16)
C18	5044(16)	477(10)	6386(14)
C19	4151(19)	478(10)	5859(13)

(continued)

C20	3939(17)	704(10)	5041(14)
C21	4703(18)	902(10)	4889(14)
C22	2966(16)	671(10)	4458(14)
C23	1293(19)	681(13)	4190(16)
C24	560(17)	876(13)	4530(16)
C25	7896(15)	2646(11)	7101(12)
C26	7389(18)	2086(12)	7296(12)
C27	6241(15)	2622(12)	7723(12)
C29	4944(19)	3394(12)	7674(11)
C30	3985(20)	3519(15)	7539(13)
C31	3388(18)	2995(13)	7342(13)
C32	3632(18)	2361(13)	7266(11)
C33	4592(19)	2258(14)	7429(11)
C34	2925(17)	1836(12)	7025(14)
C35	1328(18)	1498(13)	6248(14)
C36	490(16)	1674(15)	5513(15)
C37	4047(17)	2230(9)	5466(12)
C38	4256(17)	2537(10)	4439(13)
C39	3345(17)	2360(10)	4231(11)

$[Cu_2L4][ClO_4]_2 \cdot 2CH_2Cl_2$. Crystal data. $C_{35}H_{43}Cu_2N_{11}O_8Cl_6$, M = 1085.60, brown block, crystal dimensions 0.68 × 0.54 × 0.24 mm, monoclinic, space group C2/*c*, *a* = 27.256(8), *b* = 10.970(3), *c* = 18.941(6) Å, β = 128.37(3)°, U = 4440(2) Å^3, Dc 1.624 g cm^{-3}. μ = 1.38 mm^{-1}, Z = 4, F(000) =2216.

Data were collected at 193 K on a Nicolet R3M four-circle diffractometer using graphite-monochromated Mo-Kα radiation. 4040 reflections were collected in the range of $4 < 2\theta < 50°$. Of these, 3907 were unique and the 2783 having $F > 6\sigma(F)$ were used in the refinement.

The structure was solved by direct methods, which revealed the positions of all the non-hydrogen atoms. The refinement on 281 parameters converged with $R = 0.051$ and $Rw = 0.061$. The function minimised in the refinement was $\Sigma w(Fo\text{-}Fc)^2$ where $w =$

$[\sigma (Fo) + 0.0006Fo^2]^{-1}$. All programs used in data reduction, structure solution and refinement are contained in the SHELXTL-PC[77] package. Final coordinates are given in Table 2.6.

Table 2.6 Atomic coordinates ($\times 10^4$) for complex $[Cu_2L4][ClO_4]_2 \cdot 2CH_2Cl_2$

	x	y	z
Cu1	4626(1)	2235(1)	2848(1)
N1	4163(2)	2452(4)	3784(3)
C1	4057(3)	1178(5)	3869(3)
C2	4472(2)	326(4)	3802(3)
N2	4374(2)	556(3)	2969(3)
C3	4086(2)	-237(4)	2348(3)
C4	3889(2)	4(4)	1450(3)
C5	3448(2)	-762(4)	737(3)
C6	3202(2)	-454(5)	-124(3)
C7	3404(2)	609(5)	-261(3)
C8	3872(2)	1305(4)	492(3)
N3	4113(2)	1023(3)	1333(3)
C9	4121(2)	2343(5)	314(3)
N4	4663(2)	2799(4)	896(3)
C10	4875(2)	3695(5)	553(4)
C11	5305(2)	3060(5)	411(4)
C12	3607(2)	3185(5)	3142(3)
C13	3408(2)	3110(5)	2190(3)
N5	3945(2)	3501(4)	2236(3)
C14	3942(2)	4614(4)	2037(3)
C15	4492(2)	5250(4)	2240(3)
C16	4472(3)	6519(5)	2217(4)
C17	5000	7167(7)	2500
N6	5000	4608(5)	2500
CL1	1834(1)	2110(1)	2418(1)
O1	1934(2)	2247(3)	3247(2)
O2	1942(2)	3259(4)	2179(3)
O3	2261(2)	1226(4)	2539(3)
O4	1201(2)	1733(5)	1731(3)
CL2	1546(1)	1107(2)	5103(1)
C18	2156(3)	113(6)	5874(4)
CL3	2210(1)	-1124(2)	5330(1)

$[Cu_2(L5\text{-}3H)][ClO_4]$. Crystal data. $C_{30}H_{37}Cu_2Cl\,N_{11}O_4$, M = 777.53, brown block, crystal dimensions 0.35 × 0.32 × 0.15 mm, monoclinic, space group $P2_1/c$, a = 10.597(5), b = 17.554(9), c = 17.560(12) Å, β = 90.85 °, U = 3266(3) $Å^3$, Dc = 1.581 g cm^{-3}, μ = 1.44mm^{-1}, Z = 4, F(000) =1604.

Data were collected at room temperature on an Enraf-Nonius CAD-4 diffractometer with Mo-Kα radiation. The structure was solved by direct methods and refinement converged with R = 0.045, Rw = 0.057 for 2793 reflections with F > 6σ (F). NRCVAX programs[77] were used in data reduction. Structure solution and refinement programs are contained in the SHELXTL-PC package[79]. Final coordinates are given in Table 2.7.

Table 2.7 Atomic coordinates (× 10^4) for complex $[Cu_2(L5\text{-}3H)][ClO_4]$

	x	y	z
Cu1	9533(1)	2826(1)	-571(1)
Cu2	8208(1)	1630(1)	344(1)
N1	1178(6)	3914(3)	-970(3)
N2	6289(5)	981(4)	1170(3)
C1	11880(7)	4249(4)	-220(5)
C2	10711(7)	4110(4)	262(4)
N3	10450(5)	3289(3)	318(3)
C3	10972(7)	2922(4)	861(4)
C4	10927(6)	2108(4)	956(4)
C5	11905(6)	1702(5)	1296(4)
C6	11611(6)	923(4)	1207(4)
C7	10441(6)	902(4)	841(4)
N4	10030(5)	1634(3)	676(3)
C8	9543(7)	311(4)	749(4)
N5	8447(5)	475(3)	487(3)
C9	7428(7)	-62(4)	592(4)
C10	6702(7)	204(4)	1286(4)
C11	12728(7)	3362(5)	-1178(5)
C12	12461(7)	2588(4)	-818(4)
N6	11154(5)	2353(3)	-966(3)

(continued)

C13	10951(7)	1860(4)	-1484(4)
C14	9685(7)	1602(4)	-1623(4)
C15	9161(8)	1189(4)	-2221(4)
C16	7880(9)	1151(4)	-2079(4)
C17	7691(7)	1524(4)	-1398(4)
N7	8793(5)	1818(3)	-1111(3)
C18	6548(7)	1566(4)	-978(4)
N8	6559(5)	1674(3)	-259(3)
C19	5353(7)	1727(5)	133(4)
C20	5198(7)	1063(5)	672(4)
C21	11258(8)	4370(5)	-1588(4)
C22	10266(7)	3933(4)	-2034(4)
N9	9331(5)	3656(3)	-1508(3)
C23	8266(7)	3995(4)	-1463(4)
C24	7461(6)	3834(3)	-844(4)
C25	6378(7)	4214(4)	-609(4)
C26	6148(6)	3970(4)	123(4)
C27	7071(6)	3429(4)	304(4)
N10	7879(5)	3332(3)	-297(3)
C28	7130(7)	3018(4)	998(4)
N11	7642(5)	2372(3)	1118(3)
C29	7482(8)	1992(4)	1857(4)
C30	6296(7)	1490(4)	1837(4)
Cl1	3903(2)	1237(1)	7086(1)
O1	3986(6)	1729(4)	6445(4)
O2	4047(7)	1634(5)	7765(4)
O3	2688(5)	891(3)	7081(3)
O4	4858(6)	678(4)	7059(4)

2.3. Spectroscopy

^{1}H NMR spectra were obtained at QUB with 300 and 500 MHz spectrometers or with the SERC high-field 400 MHz NMR service at Warwick. Infrared spectra were determined as KBr discs or Nujol mulls with a Perkin-Elmer 983 G spectrophotometer. Electronic spectra were recorded on a Perkin-Elmer Lambda 9 spectrometer. EPR

spectra were measured as X-band with a Varian E-109 spectrometer equipped with an Oxford Instruments continuous-flow cryostat. FAB mass spectra were obtained either at QUB with a Spartan Ion Tech Saddle Field Source using argon on an AEI MS902, or at the SERC Mass Spectrometry Centre at Swansea.

2.4. Electrochemical measurements

Cyclic voltammograms were recorded at 20 °C under the protection of N_2, with an EG&G Model 264A or 362 polarographic analyser. The data were analysed with the EG &G Condecom software package (*i*R compensation was not used). A glassy carbon disk and a platinum wire were used as the working and counter electrodes, respectively. Potentials (± 10 mV) were quoted with respect to that of ferrocene/ferrocenium (1+) couple that was arbitrarily given the value of zero volts. Silver/silver chloride was used as the reference electrode, against which the Fc/Fc^+ couple had $E_{½} = 382$ mV.

Tetraethylammonium perchlorate (0.1M)/dimethylformamide was used as the supporting electrolyte/solvent system. The peak currents of the oxidation waves were calibrated by using a dicopper(I) cryptate[78] which is known by reaction stoichiometry to undergo a one-electron oxidation with $AgClO_4$.

2.5. Magnetic susceptibility measurements

Magnetic susceptibility measurements were made in the temperature range of 4 – 300 K with an Oxford Instruments Faraday balance with a field of 0.8 T. Mercury tetrakis(thiocyanato)cobalt (II) was used to calibrate the balance, and all molar susceptibilities were corrected for diamagnetic contributions with Pascal's constants.

The data were fitted by the Bleaney-Bower equation (1), which expresses the variation of

$$\chi_m = (Ng^2\beta^2/3kT)[1 + 1/3\ \exp(-2J/kT)]^{-1} + N\alpha$$

the molar susceptibility with temperature for the spin Hamiltonian H = -2J (S1·S2). The value of the temperature independent paramagnetism, $N\alpha$, was set at 60×10^{-6} $cm^3\ mol^{-1}$ per copper ion. The value of J and g were determined by least-square fitting with an agreement factor $R = \Sigma_i[\chi_m(exptl.)(i) - \chi_m(calc.)(i)]^2/[\chi_m(exptl.)(i)]^2$.

2.6. Catalytic Oxidation Reaction

The experiments on the catalytic oxidation of 3,5-ditertbutylcatechol (3,5-DTBC) were performed at 25 °C. In a typical reaction, the dicopper(I) complex was generated in situ and under argon by dissolving 5×10^{-3} mmol ligand in 5 ml acetonitrile/methanol mixture and then adding 2 equivalent of $[Cu(MeCN)_4][BF_4]$ solid. The solution was stirred for 10 min to allow the complete formation of the dicopper(I) complex. A 10-fold excess of 3,5-DTBC was then added to this solution under argon and the solution was purged with oxygen for 10 min. The formation of oxidation product 3,5-ditertbutyl quinone (3,5-DTBQ) was followed by measuring the absorption at ~ 408 nm (ε = 18000 $M^{-1}cm^{-1}$). The oxidation reaction in the presence of dicopper(II) complexes was performed in a similar way.

CHAPTER 3 DICOPPER COMPLEXES OF HEXAIMINO CRYPTANDS

3.1 Synthesis and hydrolytic sensitivity of dicopper(II) complexes

L1 can not be synthesized by direct condensation of tren and 2,5-diformyl-thiophene. It is made as the disilver complex $[Ag_2L1][O_3SCF_3]_2$ or dicopper(I) complex $[Cu_2L1][BF_4]_2$ by the template method in near-quantitative yield. Transmetallation of $[Ag_2L1][O_3SCF_3]_2$ with Cu(I) or Cu(II) salts also generates $[Cu_2L1][O_3SCF_3]_2$ or $[Cu_2L1][BF_4]_2$. No dicopper(II) complex can be synthesized with **L1** even when Cu(II) salts were used.

L2 is synthesized by the direct condensation of tren and 2,5-diformylfuran. Treatment of **L2** with a Cu(I) salt under a nitrogen atmosphere easily generates the dicopper(I) complex $[Cu_2L2]X_2$ ($X = BF_4^-$, ClO_4^-) as a red microcrystalline solid that is stable in air both in solution and in solid form. In attempts to incorporate a single- or two- atom bridge between the copper(I) centers $[Cu_2L2]X_2$ was treated with neutral ligands such as pyridazine, CO, and O_2. In all three cases, unchanged starting materials were recovered. Treatment of **L2** with a Cu(II) salt in undried ethanol generates dicopper(II) complex $[Cu_2L2(OH)]X_3$ ($X = ClO_4^-$, PF_6^-) as a bright green microcrystalline solid. If Him (imidazole) is added to the mixture of **L2** and Cu(II) salt, the crude product $[Cu_2L2(im)][ClO_4]_3$ can be obtained. All these dicopper(II) complexes lack long-term solution stability. With –OH as the bridge between two Cu(II) centers, the

solution changes color from bright green to blue green as it sits in solution over a couple of hours, indicating a change of coordination geometry consequent upon ring opening. A pure sample of the dicopper(II) complex $[Cu_2\mathbf{L2'}(im)][ClO_4]_3$ (Scheme 1) was obtained in attempts to purify the crude $[Cu_2\mathbf{L2}(im)][ClO_4]_3$.

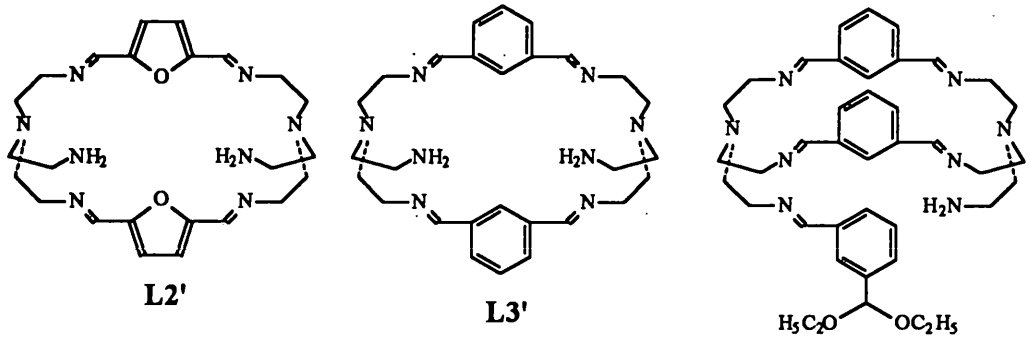

Scheme 1

L3 is synthesized by 2+3 condensation of tren and isophthalaldehyde. By reacting **L3** with Cu(I) salts $Cu(MeCN)_4X$ ($X = ClO_4^-$, BF_4^-), a dicopper(I) complex $[Cu_2\mathbf{L3}]X_2$ that is stable in either DMF or MeCN can be isolated. Treatment of $[Cu_2\mathbf{L3}]X_2$ with $AgClO_4$ as the oxidizing reagent fails to produce the copper(II) state. However, the bright green microcrystalline dicopper(II) complex $[Cu_2\mathbf{L3}(OH)][ClO_4]_3$ can be synthesized by reaction of free cryptand **L3** with $Cu(ClO_4)_2$. Similarly golden microcrystalline $[Cu_2\mathbf{L3}(N_3)][O_3SCF_3]_3$ can be obtained by mixing **L3** with $Cu(O_3SCF_3)_2$ in the presence of NaN_3. Despite repeated attempts, no bulkier bridge such as imidazolate can be incorporated between the copper(II) centers in **L3**. Indeed, even $[Cu_2\mathbf{L3}(OH)][ClO_4]_3$ and $[Cu_2\mathbf{L3}(N_3)][O_3SCF_3]_3$ show signs of strain in that they are not long-term stable in solution. The initially bright green solution of

[CuL3(OH)][ClO_4]$_3$ in MeCN, for example, develops a blue color on standing, owing to hydrolysis with a rate that is solvent and counter-ion dependent. If the solution is left for 1-2 days, particularly in the presence of CH_2Cl_2, a deep blue color develops and crystals of dicopper(II) complexes of the partially hydrolyzed ligand **L3'** or **L3"** (scheme 1) can be isolated. In the case of [Cu_2**L3'**(OH)][ClO_4]$_3$, metal-promoted hydrolysis has resulted in the cleavage of two C=N double bonds on one of the three strands of **L3** and the formation of dipendant macrocyclic ligand **L3'**. The same blue product is obtained under inert atmosphere conditions, indicating that this is a simple hydrolysis with no involvement of oxidative attack on the C-H_A· bond. In the absence of CH_2Cl_2 the hydrolysis of [Cu_2**L3**(OH)][ClO_4]$_3$ proceeds more slowly and dicopper(II) complex of asymmetric dipendant macrocyclic ligand **L3"** is isolated, in which only one C=N double bond has been hydrolyzed and solvent addition accompanying ring opening generates a terminal acetal function group.

L4 and [Cu_2**L4**]X_2 (X = BF_4^-, ClO_4^-) have been synthesized in a similar way. Unlike the other dicopper(I) complexes in the series, [Cu_2**L4**]X_2 is not long-term stable in solution and its behavior towards air- or $AgClO_4$-oxidation will be discussed in detail in this chapter. Treatment of **L4** with Cu(II) salts gives disappointing results. In the absence of base, only crude sample of colorless, apparently protonated **L4** were obtained. When base was added, the resultant green powders show $\nu_{c=o}$ IR absorption, suggesting ring opening arising from hydrolysis of the C=N double bond(s).

The dicopper(I) complex [Cu_2**L5**]X_2 (X= ClO_4^-, BF_4^-) is obtained by template synthesis on the appropriate Cu(I) salt under inert atmosphere condition. The mixed-valence complex [Cu_2(**L5-H**)]BF_4 is generated by one-electron oxidation of [Cu_2**L5**]X_2

with $FcBF_4$. The dicopper(II) complex $[Cu_2(\mathbf{L5\text{-}3H})]X$ ($X = ClO_4^-$, BF_4^-) can be synthesized through one-electron oxidation of $[Cu_2(\mathbf{L5\text{-}H})]BF_4$ or two-electron oxidation of $[Cu_2\mathbf{L5}]X_2$ by $AgClO_4$. This dicopper(II) complex can also be isolated from an aged solution of $[Cu_2\mathbf{L5}]X_2$ or $[Cu_2(\mathbf{L5\text{-}H})]BF_4$ through air-oxidation. Neither $[Cu_2(\mathbf{L5\text{-}H})]BF_4$ and $[Cu_2(\mathbf{L5\text{-}3H})]X$ are vulnerable to the hydrolytic attack that results in the cleavage of C=N double bond(s). Single crystals of $[Cu_2(\mathbf{L5\text{-}3H})]ClO_4$ suitable for X-ray crystallography were collected from an aged solution of $[Cu_2\mathbf{L5}][ClO_4]_2$

The hydrolytic sensitivity of dicopper(II) complexes of hexaimino cryptands is promoted by Cu(II) ion, which withdraws electron density from the C=N double bond more efficiently (Lewis acidity) than Cu(I) and makes it more vulnerable to attack by nucleophiles from the solution.

3.2 X-ray crystal structures of dicopper complexes

$[Cu_2\mathbf{L1}][O_3SCF_3]_2$. The crystal structure was obtained by M. Drew[79]. The asymmetric unit contains half of each of two independent $[Cu_2\mathbf{L1}]^{2+}$ cations along with two triflate anions (Table 3.1). Each cation sits on a two-fold rotation axis which passes through the sulfur atom in one of the thiophene rings [S(2)] and bisects the Cu — Cu vector. There is an approximate, non-crystallographic three-fold axis passing through the copper ions and bridgehead nitrogen atoms of each cation. Although the cations are very similar, there are some subtle differences that can probably be ascribed to packing effects, the most noticeable of which being the Cu · · · Cu distances [Cu(1) · · · Cu(1a) 4.733(2) and Cu(2) · · · Cu(2a) 4.826(2) Å]. In each case (Figure 3.1) the copper ion is co-ordinated to the three imino nitrogen atoms and is displaced by *ca* 0.5 Å from the plane of the three imino donors towards the center of the cavity. The copper ions and

bridgehead nitrogen atoms interact weakly [2.56(1) and 2.51(1) Å for Cu(1) — N(1) and Cu(2) — N(2), respectively] and the copper-thiophene sulfur distances are in the range of 3.17 – 3.31 Å. The distances between bridgehead nitrogen atoms (9.859,

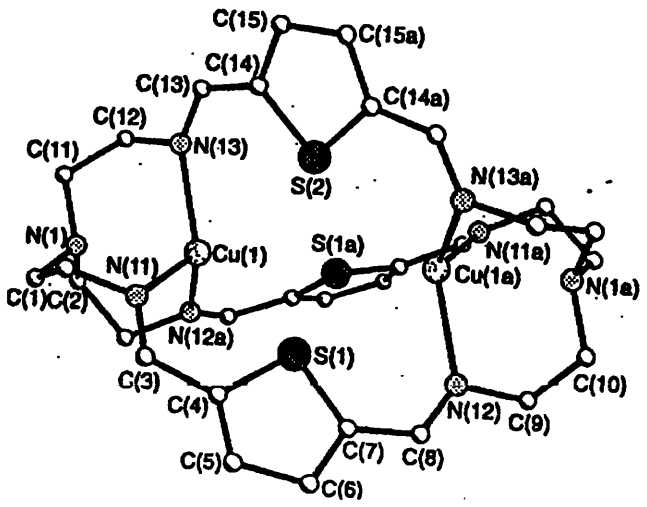

Figure 3.1 Structure of the cation of $[Cu_2L1][O_3SCF_3]_2$

9.855 Å) and the Cu · · · Cu distances (4.733, 4.826 Å) are the longest of the dicopper (I) complexes of hexaimino cryptands discussed in this section. Although it would appear possible to incorporate a single-atom (perhaps even a non-linear two-atom) bridge between copper cations, any bridging ligand would have to suffer the consequences of close approach to the thiophene sulfur lone pairs.

Table 3.1 Selected bond lengths (Å) and angles (°) for $[Cu_2L1][O_3SCF_3]_2$

Cu(1)-N(11)	2.180(11)	Cu(1)-N(12a^{I})	2.229(9)
Cu(1)-N(13)	2.232(10)	Cu(1)-N(1)	2.563(10)
Cu(2)-N(23^{II})	2.240(10)	Cu(2)-N(21^{II})	2.247(11)
Cu(2)-N(22)	2.270(10)	Cu(2)-N(2^{II})	2.514(11)

(continued)

N(11)-Cu(1)-N(12a^{I})	113.9(3)	N(11)-Cu(1)-N(13)	113.8(3)
N(12a^{I})-Cu(1)-N(13)	112.4(3)	N(11)-Cu(1)-N(1)	74.4(3)
N(12a^{I})-Cu(1)-N(1)	74.9(3)	N(13)-Cu(1)-N(1)	75.1(3)
N(23^{II})-Cu(2)-N(21^{II})	116.3(4)	N(23^{II})-Cu(2)-N(22)	113.4(4)
N(21^{I})-Cu(2)-N(22)	111.7(4)	N(23^{II})-Cu(2)-N(2^{II})	75.1(4)
N(21^{II})-Cu(2)-N(2^{II})	76.1(4)	N(22)-Cu(2)-N(2^{II})	74.8(3)

Symmetry transformations used to generate equivalent atoms: I $-x + 3/2, -y + 1, z$; II $-x + 3/2, -y, z$.

$[Cu_2L2][BF_4]_2$. The crystal structure was obtained by V. McKee[80]. Figure 3.2 illustrates the structure of dicopper (I) cation $[Cu_2L2]^{2+}$. Selected bond lengths and angles are given in Table 3.2 Although the cation has no crystallographic symmetry, there is an approximate three-fold axis running through the copper ions and the bridgehead nitrogen atoms. The distance between the bridgehead nitrogen atoms is now 8.89 Å, a shortening of 0.97 Å compared with that in the $[Cu_2L1][O_3SCF_3]_2$. The Cu · · · Cu distance is 4.2 Å, which is also shorter than that in $[Cu_2L1][O_3SCF_3]_2$. Each copper ion is coordinated to three imino nitrogen atoms and one bridgehead nitrogen atom, the distances from the Cu(I) ions to the bridgehead nitrogen atoms being the longest (Cu(1)-N(1) 2.388(4); Cu(2)-N(2) 2.397(4) Å). The geometry around the copper ion can be approximately described as trigonal pyramidal.

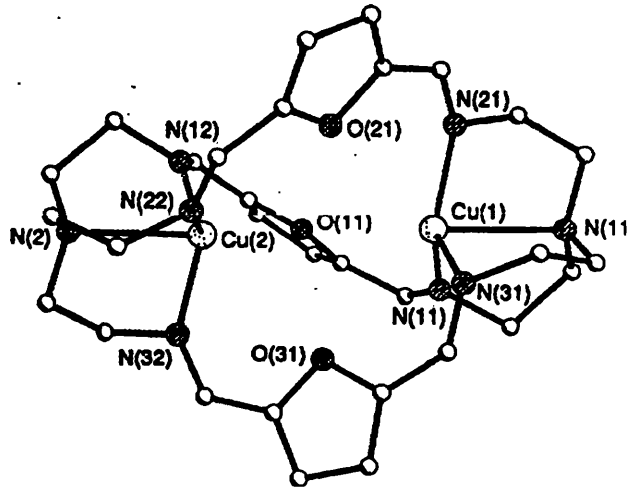

Figure 3.2 Perspective view of the cation of $[Cu_2L2][BF_4]_2$

Table 3.2 Selected bond lengths (Å) and angles (°) for $[Cu_2L2][BF_4]_2$

Cu(1)-N(1)	2.388(4)	Cu(1)-N(11)	1.991(4)
Cu(1)-N(21)	1.981(4)	Cu(1)-N(31)	2.024(4)
Cu(2)-N(2)	2.397(4)	Cu(2)-N(12)	2.003(4)
Cu(2)-N(22)	1.986(4)	Cu(2)-N(32)	2.006(4)
N(1)-Cu(1)-N(11)	81.7(1)	N(1)-Cu(1)-N(21)	79.7(1)
N(11)-Cu(1)-N(21)	123.5(2)	N(1)-Cu(1)-N(31)	79.0(1)
N(11)-Cu(1)-N(31)	111.3(1)	N(21)-Cu(1)-N(31)	116.5(1)
N(2)-Cu(2)-N(12)	79.3(1)	N(2)-Cu(2)-N(22)	80.8(1)
N(12)-Cu(2)-N(22)	119.2(1)	N(2)-Cu(2)-N(32)	80.1(1)
N(12)-Cu(2)-N(32)	112.3(2)	N(22)-Cu(2)-N(32)	119.8(2)

$[Cu_2L3"(OH)][BPh_4]_2[O_3SCF_3]\cdot H_2O\cdot 0.5EtOH$. The crystal structure was obtained by V. McKee[81]. Although the structural data for this complex are of poor quality, there are sufficient datato define the structure. The dipandent macrocycle **L3"** has adopted a U-shaped configuration, containing the pair of Cu(II) cations within the cleft. Both Cu(II) cations are in a distorted trigonal-bipyramidal co-ordination geometry (Figure 3.3), using all available nitrogen donors including the amino or imino nitrogen donor from each of the pendant arms, with a μ–OH bridge completing the coordination sphere. The distortion from trigonal bipyramidal geometry is quite severe, with > 150 ° bond angles (which involves an imino or amino nitrogen donor from the pendant arms) evident in each of the equatorial planes. The N_{ax}-Cu-N_{ax} angle is nearly 20 ° off linear.

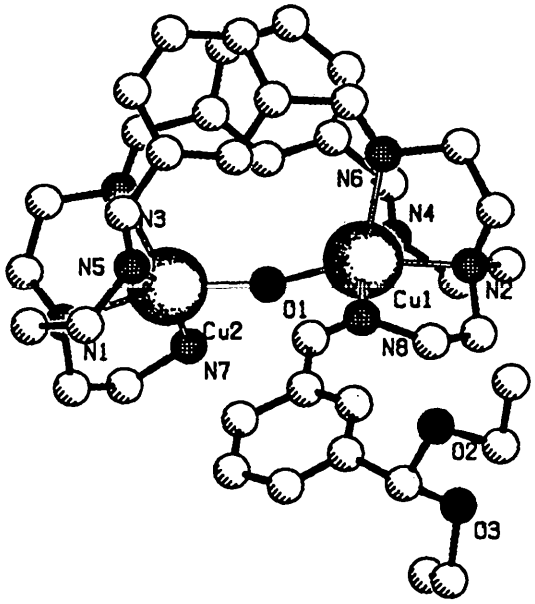

Figure 3.3 Structure of the cation of $[Cu_2L3"(OH)][BPh_4]_2[O_3SCF_3]$ $\cdot H_2O\cdot 0.5EtOH$

The Cu-(O)H-Cu angle (Table 3.3) is 166.1 (5)° and the Cu · · Cu separation is 3.89 Å. The pair of aromatic rings which comprise the macrocycle together with the two tren units are stacked at an approximate separation of 3.4 Å , which presumably contributes to the stabilization of this configuration. The acetal terminus of the pendant is directed away from the ligand cavity and makes no short intermolecular contact.

Table 3.3 Selected bond lengths (Å)) and angles (°) for

$[Cu_2$**L3"**$(OH)][BPh_4]_2[O_3SCF_3] \cdot H_2O \cdot 0.5EtOH$

Cu(1)-O(1)	1.943(9)	Cu(1)-N(8)	2.034(12)
Cu(1)-N(4)	2.073(11)	Cu(1)-N(2)	2.077(10)
Cu(1)-N(6)	2.279(10)	Cu(2)-O(1)	1.976(9)
Cu(2)-N(7)	2.009(13)	Cu(2)-N(5)	2.051(12)
Cu(2)-N(1)	2.126(12)	Cu(2)-N(3)	2.313(13)
O(1)-Cu(1)-N(8)	90.9(4)	O(1)-Cu(1)-N(4)	97.8(4)
N(8)-Cu(1)-N(4)	154.1(4)	O(1)-Cu(1)-N(2)	161.6(4)
N(8)-Cu(1)-N(2)	82.6(4)	N(4)-Cu(1)-N(2)	81.6(4)
O(1)-Cu(1)-N(6)	117.3(4)	N(8)-Cu(1)-N(6)	105.6(4)
N(4)-Cu(1)-N(6)	92.1(4)	N(2)-Cu(1)-N(6)	81.1(4)
O(1)-Cu(2)-N(7)	87.1(5)	O(1)-Cu(2)-N(5)	98.4(4)
N(7)-Cu(2)-N(5)	154.6(6)	O(1)-Cu(2)-N(1)	160.8(4)
N(7)-Cu(2)-N(1)	85.3(6)	N(5)-Cu(2)-N(1)	81.5(5)
O(1)-Cu(2)-N(3)	116.8(4)	N(7)-Cu(2)-N(3)	106.3(5)

(continued)

N(5)-Cu(2)-N(3)	93.4(5)	N(1)-Cu(2)-N(3)	82.3(5)
Cu(1)-O(1)-Cu(2)	166.1(5)		

$[Cu_2L4][ClO_4]_2 \cdot CH_2Cl_2$. The crystal structure was obtained by V. McKee[82]. The coordination geometry of this dinuclear copper(I) complex is similar to that of $[Cu_2L1][O_3SCF_3]_2$. The $[Cu_2L4]^{2+}$ cation (Figure 3.4 and Table 3.4) lies on a crystallographic two-fold axis which passes through N(6) and C(17) bisecting the Cu — Cu vector. Two symmetry-related copper ions are bound in the cavity, each coordinated to three imino nitrogen donors with an Cu-N (imino) distance of ≈ 2.02 Å. The copper atoms are displaced by 0.63 Å from the mean plane of the three imino nitrogen atoms towards the center of the cavity, resulting a further decrease in Cu-Cu separation (Cu-Cu' = 3.038(2) Å). There are weak interactions with the bridgehead nitrogen atom (Cu-N(1) = 2.753(4) Å) and one of the pyridine nitrogen atoms (Cu-N(3) = 2.640 (4) Å). In addition, there may be some even weaker interactions between the copper ion and the remaining pyridine nitrogen atoms (Cu-N(3') = 3.061(5), Cu-N(6) = 3.014(5) Å). Atoms N(1), Cu, Cu', and N(1') are not colinear, the copper ions being displaced from the N(1) – N(1') line towards the N(3) and N(3') (N(1)-Cu-Cu' = 168.3(2)°).

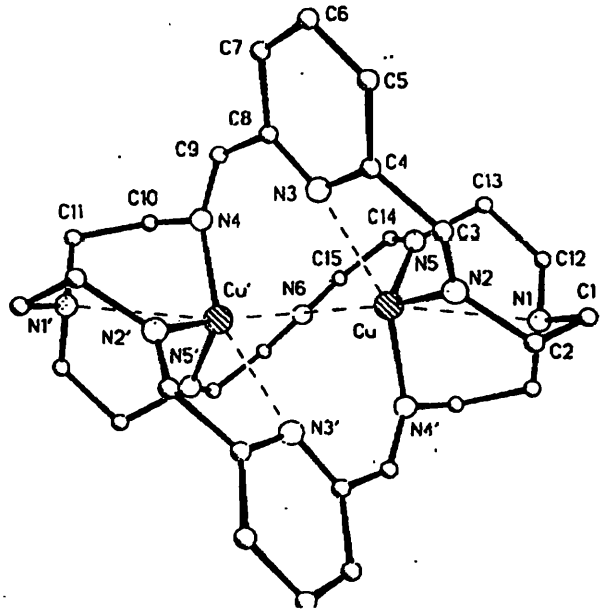

Figure 3.4 Perspective view of the cation of $[Cu_2L4][ClO_4]_2 \cdot 2CH_2Cl_2$

Table 3.4 Selected bond lengths (Å) and angles (°) for $[Cu_2L4][ClO_4]_2 \cdot 2CH_2Cl_2$

Cu-N(1)	2.753(4)	Cu-N(2)	2.028(4)
Cu-N(3)	2.640(4)	Cu-N(5)	2.011(4)
Cu-Cu'	3.038(2)	Cu-N(4')	2.019(3)
N(2)-Cu-N(3)	71.2(2)	N(2)-Cu-N(5)	115.9(2)
N(3)-Cu-N(5)	92.6(1)	N(2)-Cu-N(4')	106.8(2)
N(3)-Cu-N(4')	155.2(2)	N(5)-Cu-N(4')	109.6(2)
N(1)-Cu-Cu'	168.3(2)	N(2)-Cu-Cu'	114.5(2)
N(3)-Cu-Cu'	64.8(1)	N(4')-Cu-Cu'	95.7(2)
N(5)-Cu-Cu'	112.2(2)		

$[Cu_2(L5\text{-}3H)][ClO_4]$. The crystal structure was obtained by V. McKee[83]. It shows that the cation has no internal symmetry, and the geometry at each copper site is irregular (Figure 3.5 and Table 3.5). All three pyrrole nitrogen atoms of **L5** have been deprotonated upon co-ordination of two Cu(II) ions. Copper(1) is coordinated by three imino nitrogen donors and one negatively charged pyrrole nitrogen N(12), having a distorted tetrahedral geometry. Copper(2) is five-coordinate with a square pyramidal geometry, three imino nitrogen donors and one pyrrole nitrogen N(32) comprising the

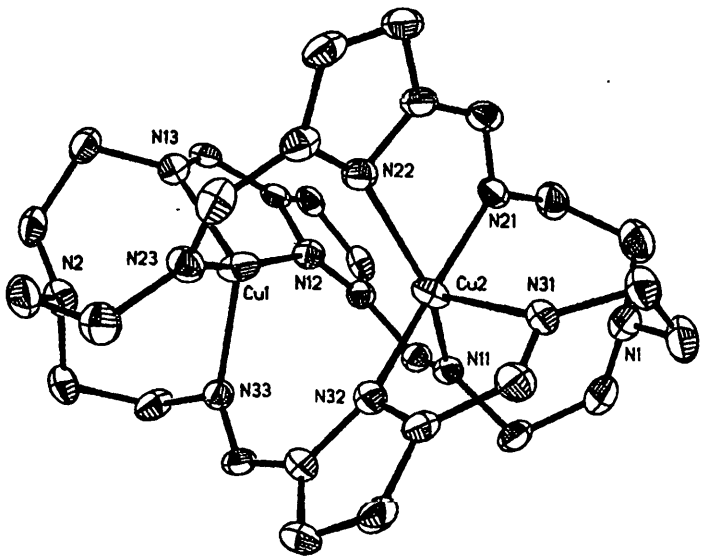

Figure 3.5 Perspective view of the cation of $[Cu_2(L5\text{-}3H)]ClO_4$

equatorial plane while the other pyrrole nitrogen N(22) is at the apical position. The pyrrole rings containing N(12) and N(32) are more or less coplanar with Cu(1) and Cu(2), respectively, whereas Cu(2) lies well out of the ring plane which contains N(22). The Cu-N(22) distance (2.15 Å) is the longest among the three Cu-N_{pyr} bonds.

Table 3.5 Selected bond lengths (Å) and angles (°) for $[Cu_2(L5\text{-}3H)]ClO_4$

Cu(1)-Cu(2)	3.006(2)	Cu(1)-N(12)	2.009(5)
Cu(1)-N(13)	2.058(6)	Cu(1)-N(23)	2.031(6)
Cu(1)-N(33)	1.981(6)	Cu(2)-N(11)	1.999(6)
Cu(2)-N(21)	2.039(6)	Cu2-N(22)	2.151(6)
Cu(2)-N(31)	2.205(6)	Cu(2)-N(32)	2.029(6)
Cu(1)-Cu(2)-N(11)	95.2(2)	Cu(1)-Cu(2)-N(21)	107.4(2)
N(11)-Cu(2)-N(21)	91.6(2)	Cu(1)-Cu(2)-N(22)	59.4(2)
N(11)-Cu(2)-N(22)	148.0(2)	N(21)-Cu(2)-N(22)	79.5(2)
Cu(1)-Cu(2)-N(31)	145.1(2)	N(11)-Cu(2)-N(31)	110.8(2)
Cu(1)-Cu(2)-N(31)	95.1(2)	N(22)-Cu(2)-N(31)	100.6(2)
Cu(1)-Cu(2)-N(32)	76.5(2)	N(11)-Cu(2)-N(32)	92.8(2)
N(21)-Cu(2)-N(32)	173.8(2)	N(22)-Cu(2)-N(32)	98.9(2)
N(31)-Cu(2)-N(32)	79.2(2)	Cu(2)-Cu(1)-N(12)	72.4(2)
Cu(2)-Cu(1)-N(13)	134.1(2)	N(12)-Cu(1)-N(13)	81.5(2)
Cu(2)-Cu(1)-N(23)	95.7(2)	N(12)-Cu(1)-N(23)	165.2(2)
N(13)-Cu(1)-N(23)	101.8(2)	Cu(2)-Cu(1)-N(33)	93.2(2)
N(12)-Cu(1)-N(33)	95.6(2)	N(13)-Cu(1)-N(33)	127.0(2)
N(23)-Cu(1)-N(33)	93.8(2)		

3.3 ^{1}H NMR Spectroscopy

The ^{1}H NMR spectrum of the dicopper(I) complex $[Cu_2L1][BF_4]_2$ in CD_3CN at room temperature shows a singlet at 8.61 ppm and another singlet at 7.58 ppm (Table 3.6), corresponding to imino protons H_C and thiophene protons H_A, respectively. This

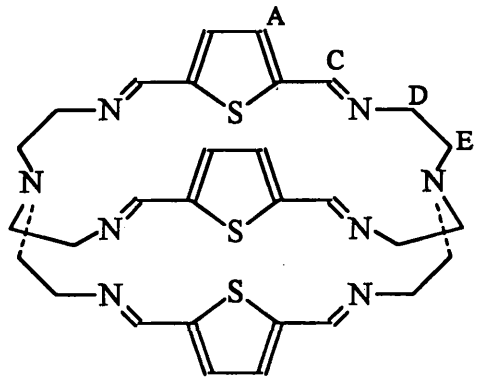

L1

lack of splitting indicates the presence of a symmetric coordination environment around two Cu(I) ions, as anticipated from the crystallographic results. The signals of methylene protons are well resolved and show no sign of fluxionality. The twelve methylene protons (H_D) on the carbon atoms adjacent to the sp^2 imino nitrogen atoms appear at lower field than the twelve methylene protons (H_E) on the carbon atoms adjacent to the sp^3 amino nitrogen atoms. Due to the "conformational rigidity" of the complex, two methylene protons on the same carbon are magnetically non-equivalent, and the geminal splitting ($H_{ax}H_{eq} \approx 12$ Hz) is observed in addition to the coincidentally similar vicinal splitting ($H_{ax}H_{ax}' \approx 12$ Hz). The vicinal couplings $H_{ax}H_{eq}'$ and $H_{eq}H_{eq}'$ are hardly discernible. Thus the signals of axial protons are split into triplets through the near-identical coupling to vicinal axial protons and the geminal equatorial protons, whilst the

signals of equatorial protons are spilt into doublets through the coupling to the geminal axial protons. An NOE (nuclear Overhauser effect) experiment involving irradiation on the H_C enhances the doublet component of the H_D signal, which is believed to correspond to $H_{D(eq)}$. The crystal structure results show that in the solid state of $[Cu_2L1][O_3SCF_3]_2$ the dicarbimine functional groups adopt a *cis, cis* conformation. Therefore the splitting pattern (from low field to high field: triplet $H_{D(ax)}$, doublet $H_{D(eq)}$, doublet $H_{E(eq)}$, triplet $H_{E(ax)}$) seen in ^1H NMR corresponds to the convergent conformation of dicopper(I) cryptate. The well-resolved spectrum of this dicopper (I) complex also suggests that the exchange of copper (I) ions between solvated and complex states is slow on the NMR time-scale.

Dicopper (I) complex $[Cu_2L2][ClO_4]_2$ gives a ^1H NMR spectrum which is similar to that of $[Cu_2L1][BF_4]_2$. The well resolved coupling pattern in the methylene proton region persists at room temperature. This involves larger geminal $H_{ax}H_{eq}$ ($\approx$ 12- 14 Hz) and vicinal $H_{ax}H_{ax}$' (13.8 Hz) coupling, together with smaller vicinal coupling

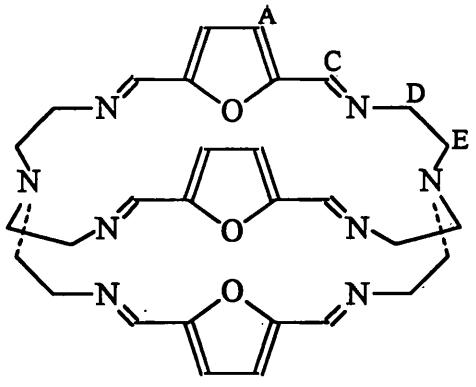

L2

such as $H_{ax}H_{eq}$' around 3-4 Hz (Figure 3.6). In comparison with the ^1H NMR spectrum of free ligand **L2**[84], it is noted that the chemical shifts of axial protons and

equatorial protons on each methylene group are reversed (Table 3.6), illustrating the difference of conformation in ligand **L2** between its uncomplexed and complexed forms. The results from X-ray crystallography confirm that **L2** is in a convergent conformation in the complex whereas it adopts a divergent conformation in its free ligand form.

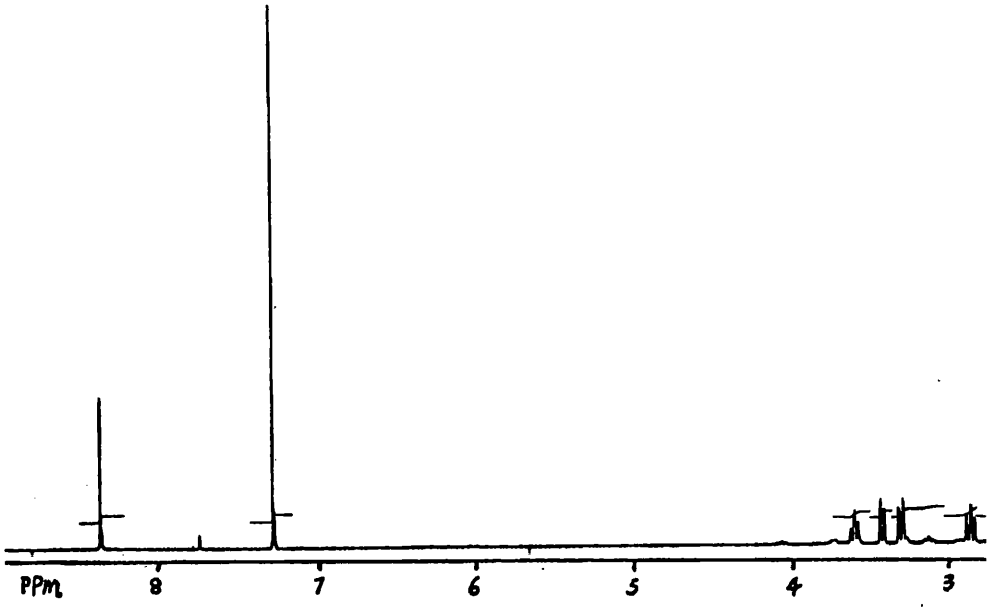

Figure 3.6 ^{1}H NMR spectrum of $[Cu_2L2][BF_4]_2$ at 293 K.

The conformational differences of **L3** between the dicopper (I) complex $[Cu_2L3][ClO_4]_2$ and free cryptand **L3** (Table 3.6) show up clearly in the unique H_A, aromatic signal, which is shifted dramatically downfield from the normal aromatic signal

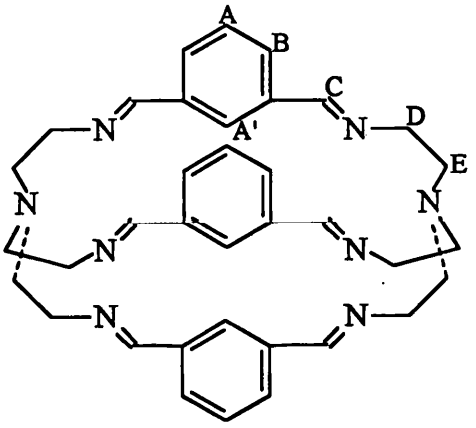

L3

in $[Cu_2L3][ClO_4]_2$ (9.91 ppm), just as it is shifted upfield to the same extent in the free cryptand **L3** (5.33 ppm) [85]. The large difference of $H_{A'}$ chemical shifts between the cryptate and the cryptand reflects that $H_{A'}$ experiences very different magnetic influences in the convergent conformation in the complex in comparison with the divergent conformation as in the free cryptand. The methylene proton (H_D, H_E) signals of $[Cu_2L3][ClO_4]_2$ are well resolved at both 294 and 233 K, showing no fluxionality. Even though the methylene region is more complex than those of the two previous dicopper (I) complexes, the absence of splitting of the H_C resonance demonstrates that the complexity does not originate from an unsymmetrical conformation in which the three strands or two ends of the macrobicycle are different. The complexity of the spectrum of $[Cu_2L3][ClO_4]_2$ may be ascribed to the larger discrepancy between vicinal and geminal coupling constants and the overlap of $H_{D(ax)}$ and $H_{D(eq)}$. At 298 K, these resonances appear as a broad doublet. But at 233 K this doublet has separated into an irregular multiplet. An NOE experiment involving irradiation on H_C enhances the high field

component of the H_D multiplet, which presumably corresponds to $H_{D(eq)}$ by analogy with other complexes' spectra. The crystal structure of $[Cu_2\mathbf{L3}][BPh_4]_2$, recently obtained[86] by Nelson et al. shows evidence of steric strain in the deviation of C=N imino functions from co-planarity with the aromatic rings (N=C(CCC)C=N torsion angle: 36.3°). This presumably affects torsion angles in the tren units and explains the alteration of coupling constants relative to the unconstrained cryptates.

The ^{1}H NMR (233K) spectrum of $[Cu_2\mathbf{L4}][ClO_4]_2$ exhibits well resolved methylene proton signals in the region of 2.6 – 3.2 ppm at 233 K (Table 3.6). A triplet due to the axial methylene protons adjacent to the bridgehead nitrogen ($H_{E(ax)}$) lies clear

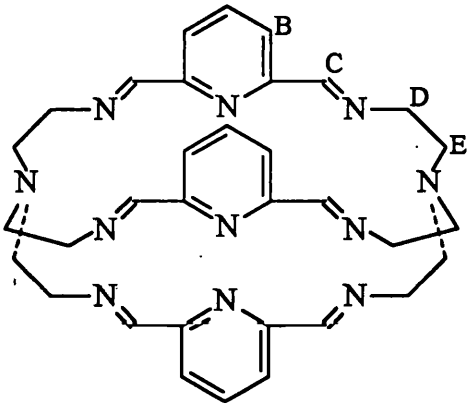

L4

of the other signals at the highest field. NOE enhancement of the doublet at ~ 3.2 ppm upon irradiation of the imino proton signal indicates that $H_{D(eq)}$ is the lowest field component in this region. The doublet signal $H_{E(eq)}$ and the triplet signal $H_{D(ax)}$ can be clearly seen at 3.16 and 3.08 ppm, respectively. It is unusual for $H_{D(ax)}$ to lie at higher

Table 3.6 ^{1}H NMR spectra of hexaimino cryptands and their dicopper(I) complexes

Compounds	ν/MHz	Solvent	T/K	H_A	$H_{A'}$	H_B	H_C	H_D	H_E
$[Cu_2L1][BF_4]_2$	400	CD_3CN	297	7.58(s)			8.61(s)	3.66(t), 3.38(d)	3.07(d), 2.83(t)
L2	90	$CDCl_3$	293	7.03(s)			7.64(s)	3.76(d), 3.26(t)	2.93(t), 2.56(d)
$[Cu_2L2][ClO_4]_2$	400	CD_3CN	293	7.10(s)			8.22(s)	3.42(m), 3.23(d)	3.12(d), 2.67(t)
			233	7.10(s)			8.16(s)	3.36(t), 3.15(d)	3.03(d), 2.64(t)
L3	400	CD_2Cl_2	203	7.52(t)	5.33(s)	8.14(d)	7.49(s)	3.75(q), 3.19(d)	2.87(t), 2.62(q)
$[Cu_2L3][ClO_4]_2$	400	CD_3CN	293	7.71(t)	9.91(s)	7.80(d)	8.51(s)	3.30(d), 3.30(d)	3.18(d), 2.75(m)
			233	7.70(t)	9.89(s)	7.79(d)	8.50(s)	3.25(m), 3.25(m)	3.13(d), 2.64(m)
L4	400	$CDCl_3$	294	7.81(t)		8.11(d)	7.59(s)	3.57(br, s)	2.87(s)
	500	$CDCl_3$	223	7.84(t)		8.08(d)	7.50(s)	3.78(d), 3.25(t)	2.88(t), 2.78(d)
$[Cu_2L4][ClO_4]_2$	400	CD_3CN	294	8.14(br, t)		7.80(d)	8.52(s)	3.20(br)	3.00(br, d), 2.60(br, t)
	500	CD_3CN	233	8.18(t)		7.89(d)	8.52(s)	3.21(d), 3.08(t)	3.16(d), 2.67(t)

field than $H_{E(eq)}$, suggesting an unusual conformation in the dicopper complex that brings $H_{E(eq)}$under the influence of the deshielding cone of the aromatic circulation associated with the pyridine rings.

Unlike other dicopper complexes of this series, fluxionality was evident in the ^1H NMR spectra of $[Cu_2\mathbf{L4}][ClO_4]_2$. At ambient temperature, broad signals are observed for the methylene protons. However when the temperature is lowered to 233 K the axial methylene proton signals are resolved into triplets and equatorial methylene proton signals into doublets. This is similar to the behavior of the free ligand, **L4**, in which the axial and equatorial methylene proton signals are indistinguishable[87] at ambient temperature but frozen out into doublet and triplet components at 213 K. The coalescence temperature Tc of H_D at 500 MHz for **L4** (at 293 K in $CDCl_3$) is similar to that for $[Cu_2\mathbf{L4}][ClO_4]_2$ (298 K in CD_3CN).

NOE enhancement of H_B upon irradiation on H_C of $[Cu_2\mathbf{L4}][ClO_4]_2$ suggests that the imino nitrogens point into the cavity while the imino CH groups point outward. The ligand **L4** in the dicopper cryptate adopts a convergent conformation as seen in other dicopper cryptates, which is also confirmed by the X-ray crystal structure of $[Cu_2\mathbf{L4}][ClO_4]_2 \cdot CH_2Cl_2$.

The complicated ^1H NMR spectrum of $[Cu_2\mathbf{L5}][BF_4]_2$ (Figure 3.6) has been assigned with the assistance of NOE and COSY 45 (Table 3.7). The spectrum shows three different imino proton (H_b, H_c, H_d) signals around 8.08-8.29 ppm and three pyrrole CH proton signals (H_e, H_f, H_g) around 6.65 – 6.74 ppm, of which H_f and H_g are coupled to each other. As far as these protons are concerned, one strand of the complex is different from the other two, and each end of the cryptate is also different. Indeed, two

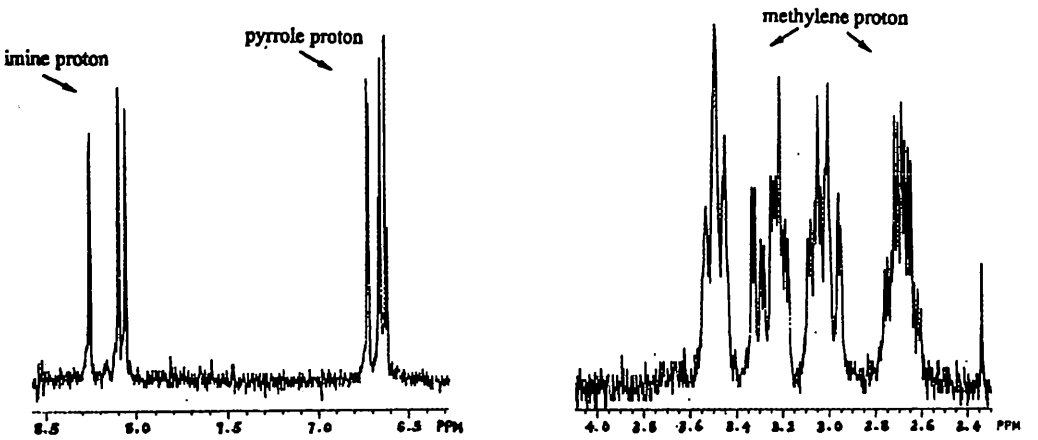

Figure 3.7 ^{1}H NMR spectrum of $[Cu_2L5][BF_4]_2$ at 345 K.

separate sets (H_b, H_h, H_k, H_n, H_q and H_d, H_j, H_m, H_p, H_s) of imino and methylene proton signals which are related (through NOE and COSY) to H_f and H_g protons respectively, can be identified. The third strand of the complex does not show any coupling or differentiation of the pyrrole CH protons and the imino protons. Therefore it looks as though the complex adopts a 'basket' conformation in which the third

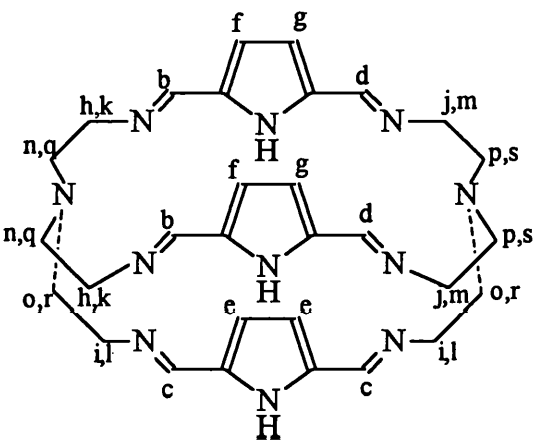

L5

strand is the 'handle'. In agreement with this proposal, a relatively sharp signal has been observed at 11.67 ppm ($H_{a'}$) for one of the three pyrrole NH protons, together with a much broader lower field signal (H_a) corresponding to the other two pyrrole NH protons.

The coupling pattern of the methylene protons indicates that axial methylene protons (H_q, H_r, H_s) on the carbons adjacent to the bridge-head nitrogen atoms lie at the highest field while the axial methylene protons (H_h, H_i, H_j) on the carbons adjacent to the imino nitrogen atoms are the lowest field components of the methylene proton signals. Both COSY and NOE results confirm, like the other dicopper(I) cryptates in this series, the presence of a convergent ligand conformation induced by the Cu(I) ions.

Table 3.7 ^{1}H NMR spectrum of $[Cu_2L5][BF_4]_2$ in CD_3CN at 345K[a]

Pyrrole NH	Imino CH	Pyrrole CH	Methylene CH_2			
H_a	H_b	H_f	H_h	H_k	H_n	H_q
12.9br(s)	8.29(s)	6.65(d)	3.58(t)	3.34(d)	3.10	2.70
$H_{a'}$	H_c	H_e	H_i	H_l	H_o	H_r
11.67(s)	8.11(s)	6.74(s)	3.54(t)	3.26(d)	3.06	2.72
H_a	H_d	H_g	H_j	H_m	H_p	H_s
12.9br(s)	8.08	6.69(d)	3.51(t)	3.23(d)	3.01	2.75

[a] Signals have been assigned by a combination of NOE and COSY 45.

The variable temperature ^{1}H NMR studies of $[Cu_2L5][BF_4]_2$ reveal that each methylene proton group is frozen out into H_{ax} and H_{eq} even at temperature as high as 345

K. It appears that steric constraint within the molecule prevents the inter conversion of the axial and equatorial positions even at higher temperature.

3.4 Redox behavior

The siting of copper in a coordination environment composed of soft donors such as sp^2 nitrogen is of great interest in bioinorganic chemistry[88]. Such an environment frequently generates a borderline Cu(I)/Cu(II) stability for utilization in enzyme-mediated redox transformations. In abiological systems, particularly where geometric constraint is absent, soft donors such as -S or -P are normally considered necessary to stabilize the Cu(I) oxidation state[89]. However, it has been noted [90.91] that ligands that favor tetrahedral coordination geometry stabilize Cu(I) even in the absence of S- or P- donors. Hexaimino cryptands **L1-L5** provide a pair of trigonal N3 or distorted tetrahedral N4 coordination sites depending on whether or not the bridgehead N is utilized, and at least six "softer" sp^2 nitrogen donors. X-ray crystallographic structural data available for dicopper(I) complexes of **L1-L4** (the crystal structure of dicopper(I) complex $[Cu_2L3][BPh_4]_2$ was obtained recently by Nelson et al.[89]) confirm the dominance of trigonal/distorted tetrahedral coordination geometry. In fact none of the dicopper(I) cryptates of **L1-L5** were subject to air oxidation within a period of hours in either acetonitrile or dimethylformamide (DMF) solutions. In order to understand whether this stability arises from thermodynamic or kinetic factors the cyclic voltammetry of the dicopper (I) cryptates of **L1-L5** has been investigated.

The cyclic voltammetric data are listed in Table 3.8. $[Cu_2L1][BF_4]_2$ and $[Cu_2L2][BF_4]_2$ have similar cyclic voltammograms. Both show a single irreversible two-

electron oxidation wave together with a irreversible reduction wave (Figure 3.8). Complex $[Cu_2L1][BF_4]_2$ is more stable towards the oxidation than $[Cu_2L2][BF_4]_2$ by 200 mV. The irreversible electrochemical behavior of these two dicopper(I) complexes is presumably a consequence of the hydrolytic instability of the corresponding dicopper(II) complexes formed on oxidation.

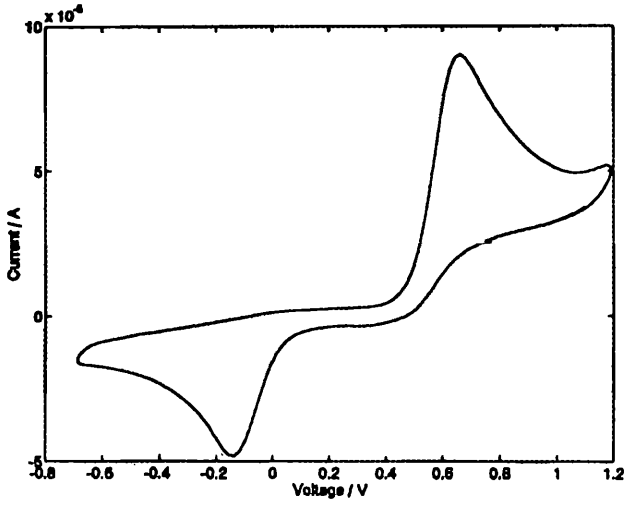

Figure 3.8 Cyclic voltammogramm of $[Cu_2L2][BF_4]_2$, potentials vs. Ag/AgCl, scan rate 50 mV s^{-1}.

$[Cu_2L3][BF_4]_2$ gives a pair of irreversible oxidation waves at 480 and 700 mV and shows similar stability towards oxidation as $[Cu_2L1][BF_4]_2$. Even though the two oxidation waves may suggest a possibility of a two-step one-electron process involving a mixed-valence species, the evidence from the X-ray crystallographic results[86] (symmetrical coordination environment around the two Cu(I) ions and the relatively large Cu-Cu separation ~ 4.2 Å) opposes this possibility. The irreversibility may be

attributed to the modification of the ligand such as ring-opening of the cryptand following the oxidation of Cu(I) to the Cu(II) state.

Table 3.8 Cyclic voltammetric data[a] for dicopper(I) cryptates

Complex	Ea^1	Ec^1	ΔE	Ea^{2b}	Ec^2	ΔE	Ec^{3c}
$[Cu_2L1][BF_4]_2$	480[d]	310[e]	170(*irr*)				-450(*br, irr*)
$[Cu_2L2][BF_4]_2$	280[d](*irr*)						-510(*br, irr*)
$[Cu_2L3][BF_4]_2$	480[f](*irr*)			700(*irr*)			-480(*br, irr*)
$[Cu_2L4][BF_4]_2$	-110[f]	-190	80(*qr*)	60	-20	80(*qr*)	-450(*br, irr*)
$[Cu_2L5][BF_4]_2$	-30[f]	-110	80(*qr*)	410(*irr*)			-500(*br, irr*)

a. Scan rate 50 mVs^{-1}, DMF solution, potentials vs. Fc/Fc^+ which has $E_{1/2}$ of 382 mV against Ag/AgCl.
b. Assumed $[Cu_2L]^{3+}$ oxidation.
c. Irreversible reduction of oxidation decomposition product.
d. Only one broad two-electron wave observed.
e. Weaker reduction component.
f. Assumed $[Cu_2L]^{2+}$ oxidation.

Ea = anodic peak potential, Ec = cathodic peak potential, ΔE = Ea- Ec. *qr* = quasi-reversible, *irr* = irreversible.

Two closely spaced quasi-reversible one-electron oxidation waves (Ea^1 = -110, and Ea^2 = 60 mV *vs* Fc/Fc^+) are observed for $[Cu_2L4][BF_4]_2$. It is noted that its stability towards oxidation is considerably decreased compared to those of $[Cu_2L1][BF_4]_2$, $[Cu_2L2][BF_2]_2$, and $[Cu_2L3][BF_4]_2$, even though there is no obvious color change of its solution on exposure to air or oxygen. The stability enhancement of the Cu(II) oxidation state in cryptand L4 may arise from the involvement of pyridine nitrogen donors in the

coordination sphere of Cu ions, constituting overall a more favorable coordination environment for Cu(II).

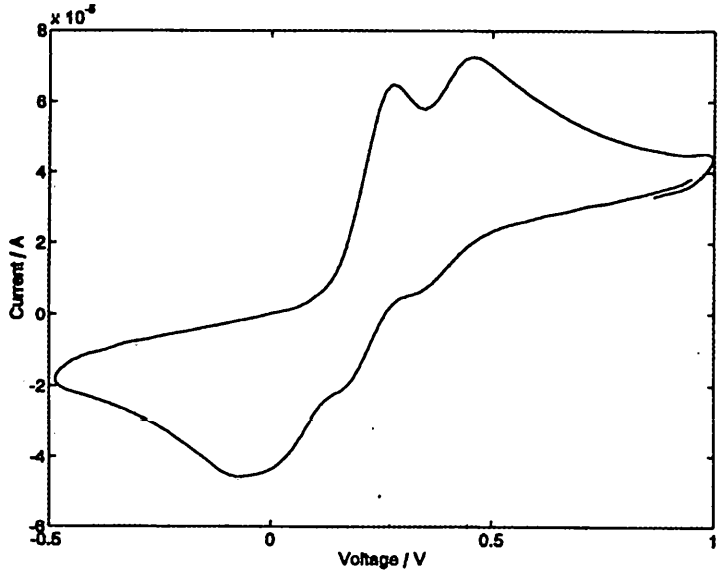

Figure 3.9 Cyclic voltammogramm of $[Cu_2L4][BF_4]_2$, potentials vs. Ag/AgCl, scan rate 50 mV s^{-1}.

From the oxidation potentials it seems that the mixed valence cryptate of **L4** can be synthesized from the oxidation of $[Cu_2L4][BF_4]_2$ with $FcBF_4$. Indeed a light brown product $[Cu_2L4][BF_4]_3$ which has magnetic susceptibility corresponding to one unpaired electron has been isolated from the 1:1 mixture of $[Cu_2L4][BF]_4$ and $FcBF_4$. The EPR spectrum of $[Cu_2L4][BF_4]_3$ contains an 'axial' 4-line signal ($g_{//}$= 2.33, $A_{//}$ = 120 G, $g_{\perp}$= 2.05) together with a different 4-line signal ($g_{//}$= 2.14, $A_{//}$ = 160 G, $g_{\perp}$= 2.00) as a minor component. The $A_{//}$ = 160 G signal eventually replaces the $A_{//}$ = 120 G signal and the

solids recovered from an aged solution of $[Cu_2L4][BF_4]_3$ show ν_{CO} and ν_{NH} absorptions in the IR spectrum, indicating that the ligand has been modified by the hydrolysis of imino C=N double bond(s). The formation of a mixed-valence cryptate of **L4** may be due to the shorter Cu-Cu distance (3.04 Å in $[Cu_2L4][BF_4]_2$) which probably is close enough for two Cu ions to interact with each other. The poor solution stability of mixed-valence $[Cu_2L4][BF_4]_2$ and the difficulty in synthesizing the dicopper(II) cryptate of L4 seems in contradiction to the cyclic voltammetry results. One possible explanation is that the coordination of pyridine nitrogen donor(s) to the Cu(II) ion(s) in the mixed-valence or dicopper(II) cryptate increases the strain in the cryptate and renders it even more hydrolytically sensitive.

With $[Cu_2L5][BF_4]_2$, three well-separated oxidation waves ($Ea^1 = -30$, $Ea^2 = 410$, and $E_a^3 = 693$ mV vs. Fc/Fc^+) are observed (Figure 3.10a). The first two may be assigned to the two-step one-electron oxidation process that involves the generation of the mixed-valence and dicopper(II) cryptates. The oxidation wave appearing at potentials above 693 mV indicates electrochemical-activity of the ligand **L5**, which may be attributed to deprotonation of the pyrrole nitrogen in the manner well-established for porphyrin complexes[92]. This may also account for the irreversible nature of the second oxidation wave. Once deprotonation has taken place, the oxidation state of the coordinated cation may not be easily defined because of electron delocalization, as commonly observed in porphyrin complexes between a metal ion and ligand. The redox potentials of $[Cu_2L5][BF_4]_2$ suggest that one electron-oxidation with $FcBF_4$ should be able to generate the mixed-valence dicopper(I, II) cryptate. Indeed the oxidation product of $[Cu_2L5][BF_4]_2$ by $FcBF_4$ is the mixed-valence cryptate $[Cu_2(L5\text{-}H)][BF_4]_2$, which has a

temperature-independent solid-state magnetic moment around 2.0 μB per formula unit and a MeCN glass EPR spectrum consisting of a poorly resolved $g \approx 2$ signal lacking hyperfine structure. The absence of hyperfine structure of the EPR spectrum hinders the assessment of the degree of electron delocalization between two copper sites. The lack of intense near-IR absorption attributable to intervalence transfer, however, indicates that $[Cu_2(\mathbf{L5\text{-}H})][BF_4]_2$ may be classified as Class 1[93] localized mixed-valence species. In the absence of base, no perceptible oxidation of $[Cu_2(\mathbf{L5\text{-}H})][BF_4]_2$ by $AgClO_4$ or O_2 occurs over a period of days. At pH > 7, nevertheless, such oxidation takes place within hours, confirming that the oxidation of the Cu(I) center of the mixed-valence species is associated with deprotonation of pyrrole nitrogen atom(s).

The cyclic voltammogram of $[Cu_2(\mathbf{L5\text{-}H})][BF_4]_2$ (Figure 3.10b) shows that the first oxidation wave is shifted about 500 mV negatively whereas the second oxidation wave is almost unchanged, in comparison with that of $[Cu_2\mathbf{L5}][BF_4]_2$. This suggests that the deprotonated pyrrole nitrogen coordinates to Cu(II) at the site generating Ea^1 while the site generating Ea^2 in $[Cu_2(\mathbf{L5\text{-}H})][BF_4]_2$ remains the same as in $[Cu_2\mathbf{L5}][BF_4]_2$. However, the cyclic voltammogram of $[Cu_2(\mathbf{L5\text{-}H})][BF_4]_2$ obtained in basic MeCN solution shows shifting of Ea^2 to a more negative potential together with a loss of reversibility, implying that further deprotonation of pyrrole nitrogen atom(s) affects the second copper coordination site.

Oxidation of $[Cu_2(\mathbf{L5\text{-}H})][BF_4]_2$ or $[Cu_2\mathbf{L5}][BF_4]_2$ in basic solution with $AgClO_4$ generates a dark-brown solution from which black crystals of dicopper(II) $[Cu_2(\mathbf{L5\text{-}3H})]ClO_4$ can be isolated. The dicopper(II) formulation is confirmed by the elemental analysis and the absence of ν_{NH} IR absorption. The electrochemistry of

$[Cu_2(L5\text{-}3H)]ClO_4$ (Figure 3.10c) is quite different from that of $[Cu_2(L5\text{-}H)][BF_4]_2$, demonstrating that neither of the coordination sites revealed in the crystal structure are identical with those in $[Cu_2(L5\text{-}H)][BF_4]_2$. The voltammogram of $[Cu_2(L5\text{-}3H)]ClO_4$ shows little reversibility with a feature consisting of two broad overlapping anodic waves (-299 and 55 mV, vs. Fc/Fc^+) and a single cathodic wave (-550 mV vs. Fc/Fc^+). Irreversibility presumably derives from the instability of the reduced form of $[Cu_2(L5\text{-}3H)]ClO_4$. Chemical reduction of this dicopper(II) complex with ascorbic acid generates dicopper(I) cryptate $[Cu_2L5)][BF_4]$, whereas no reduction has so far been observed with non-acidic reductants such as $Cu(MeCN)_4ClO_4$ or $NaBPh_4$. This further confirms that the redox reactions of dicopper complexes of **L5** are closely linked to the pH. Scheme 2 summaries the observed redox transformations.

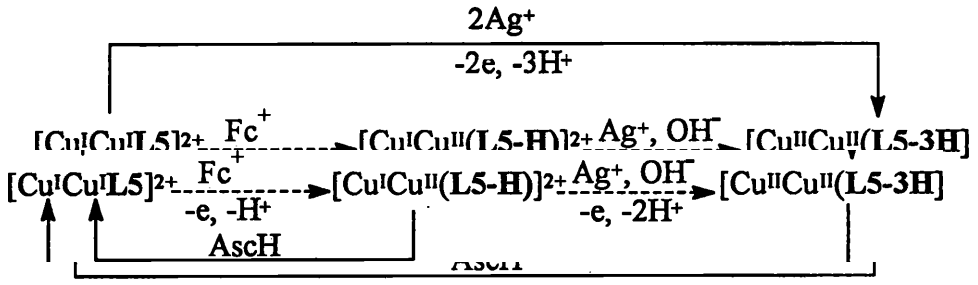

Scheme 2

It is worthwhile to mention that both mixed-valence and dicopper(II) cryptates of **L5** show no sign of hydrolysis of the ligand. This may be attributed to the negative charge on the deprotonated ligand that considerably reduces the Lewis acidity of Cu(II) ion and therefore the vulnerability of C=N double bond to attack from nucleophiles.

(a)

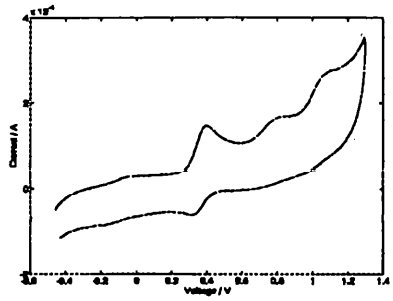

(b)

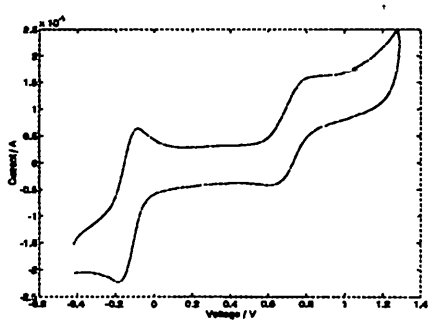

(c)

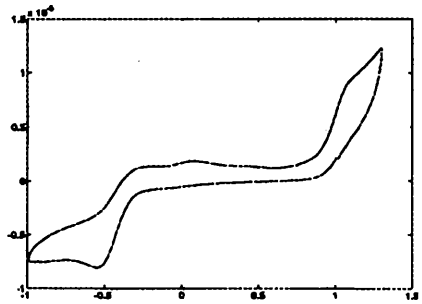

Figure 3.10 Cyclic voltammogramm of (a) $[Cu_2L5][BF_4]_2$, (b) $[Cu_2(L5\text{-}H)][BF_4]_2$, (c) $[Cu_2(L5\text{-}3H)]ClO_4$, potentials vs. Ag/AgCl, scan rate 50 mV s^{-1}.

3.5 Spectroscopic and magnetic properties of dicopper(II) complexes

Only a few dicopper(II) complexes of hexaimino cryptands have been obtained with acceptable purity. Among them, $[Cu_2L2(OH)]X_3$ ($X = ClO_4^-$, PF_6^-) and $[Cu_2L3(OH)][ClO_4]_3$ have similar d-d transition bands ($[Cu_2L2(OH)]X_3$: 720, 875 nm; $[Cu_2L3(OH)][ClO_4]_3$: 720, 845 nm), indicating similar coordination geometries around Cu(II) ions in these two complexes: trigonal bipyramidal[94]. The ligand-to-metal charge-transfer band $HO^- \rightarrow$ Cu(II) occurs at around 400 nm in both complexes. There are no EPR signals from either two and magnetic susceptibility measurements have been carried out. The molar susceptibility per Copper(II) ion has been fitted to the Bleaney-Bowers equation (1) based on the Hamiltonian $-2JS1 \bullet S2$ for the two interacting spins (-1/2, 1/2), modified to take

$$\chi_m = (Ng^2\beta^2/3kT)[1+1/3\exp(-2J/kT)]^{-1}(1-P) + PNg^2\beta^2/4kT + N_\alpha \quad (1)$$

account of temperature-independent paramagnetism (N_α) and the contribution of a small percentage (P) of monomeric paramagnetic impurity. The best fits have been obtained with a $-2J$ value of 965 cm^{-1} for $[Cu_2L2(OH)]X_3$ and 800 cm^{-1} for $[Cu_2L3(OH)][ClO_4]_3$. Such large antiferromagnetic exchanges, which are close to the upper limit[95, 96] of those known for a pair of copper(II) ions separated by a single hydroxo bridge, imply efficient mediation of magnetic exchange. Lack of long-term solution stability of these two complexes prevents growth of crystals of sufficient size to confirm the speculation that the efficient antiferromagnetic exchange derives from enforced linearity of the Cu-O(H)-Cu moiety. However, the linearity hypothesis of the Cu-O(H)-Cu moiety has been

confirmed by the crystal structure of an EPR-silent hydroxo-bridged dicopper(II) complex of **RL2**, which will be discussed in the next chapter.

The electronic spectrum of $[Cu_2L3(N_3)][O_3SCF_3]_3$ also suggests a trigonal bipyramidal coordination geometry (*d-d* transitions: 730, 909 nm) around each Cu(II) ion. The intense band at around 467 nm may be assigned to $N_3^- \rightarrow$ Cu(II) charge-transfer. The magnetic susceptibility measurement reveals that $[Cu_2L3(N_3)][O_3SCF_3]_3$ exhibits behavior close to the Curie law down to 80 K. The EPR spectrum is quite unusual (Figure 3.11), the breadth of the signal testifying to the existence of very large zero-field splitting. Another unusual feature of $[Cu_2L3(N_3)][O_3SCF_3]_3$ is the infrared ν_{asym}(NNN) absorption close to 2200 cm^{-1}. The possible bridging mode of the azide anion in this complex that shows unique spectroscopic properties will be discussed in the next chapter.

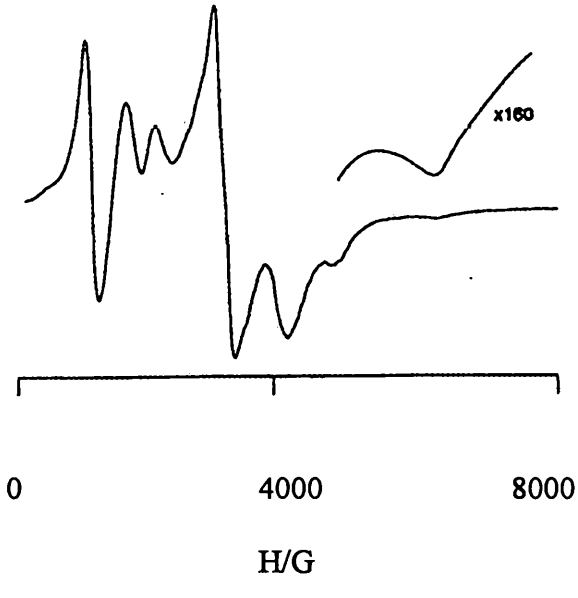

Figure 3.11 The X-band EPR spectrum of $[Cu_2L3(N_3)][O_3SCF_3]_3$, as a polycrystalline solid at 5K.

In the case of $[Cu_2(\mathbf{L5\text{-}3H})]ClO_4$, three d-d transition bands have been observed (550, 720, 904 nm). X-ray crystal structural data show that one Cu(II) ion is four-coordinate, having a geometry distorted toward tetrahedral from square planar, while the coordination geometry around the second Cu(II) ion approximates to square pyramidal. The magnetic susceptibility measurement gives a virtually temperature-independent solid-state moment of $\approx$ 1.90 μB per Cu(II) ion, which indicates that any interaction between the Cu(II) ions is limited to the through-space dipolar mechanism. The MeCN glass ESR spectrum is broad with $g \approx 2$ signal extending over 2000G and poorly defined, lacking both hyperfine structure and any clear differentiation of Cu(II) sites. A poorly resolved half-band signal appearing with $1/10^{th}$ intensity of the $g \approx 2$ signal is evidence for at least weak interaction between Cu(II) paramagnets.

3.6 Conclusions

The hexaimino cryptands **L1-L5** show good coordination properties for Cu(I) ion due to the presence of at least six sp^2 nitrogen donors in each of these cryptands and of the rigidity in the ligands which can impose a trigonal or distorted tetrahedral coordination geometry, both favoring the Cu(I) oxidation state. The crystal structure data of dicopper (I) cryptates available for **L1-L4** reveal that each Cu(I) ion is normally coordinated by three imino nitrogen atoms. In some cases Cu(I) ions also form longer bonds with the bridgehead nitrogen atoms and have weaker interaction with donor atoms from the spacer groups, such as the pyridine nitrogen in **L3**. Both X-ray crystallography and ^1H NMR results indicate that **L1-L5** adopt the convergent conformation in their complex forms which are opposite to the divergent conformation when they are as free ligands.

The results obtained on the redox behavior of dicopper(I) cryptates of **L1**-**L5** provide useful insight on the structure-redox reactivity relationship. $[Cu_2L1][BF_4]_2$, $[Cu_2L2][BF_4]_2$, and $[Cu_2L3][BF_4]_2$ are much more stable thermodynamically towards oxidation than $[Cu_2L4][BF_4]_2$ and $[Cu_2L5][BF_4]_2$, as indicated by their oxidation potentials. One common structural feature of the first three complexes is that they do not have nitrogen donors from the spacer groups which may be used in coordination of the Cu(II) state. Therefore the Cu(II) oxidation state is less favored relative to Cu(I) in **L1**-**L3** in comparison to **L4** and **L5**, both of which have additional nitrogen donors from the pyridine or pyrrole rings which could be involved in the coordination of Cu(II) oxidation state. From the cyclic voltammetric data it appears that $[Cu_2L4][BF_4]_2$ and $[Cu_2L5][BF_2]_4$ can be oxidized to mixed-valence or dicopper(II) cryptates under atmospheric conditions (it has to be remembered that the standard O_2 potentials refer to aqueous media. As our cyclic voltammetric investigations were carried in non-aqueous media due to the poor solubility of most dicopper cryptates in aqueous solution, caution must be taken in the direct comparison of thermodynamic data). Neither of these two dicopper(I) cryptates, however, shows a color change of its solution on exposure to air for days or even weeks. It seems the kinetic factors that may result from the rearrangement of the coordination geometry around Cu ion upon oxidation, are responsible for stabilizing the dicopper(I) state under aerobic conditions.

Dicopper(II) cryptates of some of the hexaimino cryptands can be isolated as azido- or hydroxo-bridged dimers through direct reaction of free ligand with the hydrated Cu(II) salt with or without NaN_3. None of these bridged dicopper(II) complexes has long-term stability in solution and ring-opened products are usually obtained from

their aged solutions due to the hydrolysis of C=N double bond(s). The dicopper(II) cryptate of **L5**, however, makes no use of anionic bridging ligands, preferring instead the strong coordination of three deprotonated pyrrole nitrogen donors. The negative charge on the cryptand significantly reduces the Lewis acidity of two Cu(II) ions encapsulated inside the cryptate and the possibility of metal-assisted hydrolytic attack on C=N double bond(s). The dicopper(II) complex of **L5** is the only one in this series which has long-term solution stability.

In order to avoid hydrolytic ring opening and to extend the range of bridged dicopper(II) cryptates that could be studied, a series of octaamino cryptands **RL1-RL5** has been synthesized by hydrogenation of hexaimino cryptands **L1-L5** with $NaBH_4$. These octaamino cryptands, which contain eight sp^3 nitrogen donors, are chemically resistant to hydrolytic degradation and are good hosts for a pair of Cu(II) ions. The chemistry of their dicopper(I)/(II) cryptates will be explored in chapter 4.

CHAPTER 4 DICOPPER COMPLEXES OF HYDROLYTICALLY-INERT OCTAAMINO CRYPTANDS

4.1 Synthesis of dicopper complexes of hydrolytically-inert ocatamino cryptands

Dicopper(I) complexes of octaamino cryptands **RL1**, **RL2**, and **RL3** have been synthesized by mixing the appropriate cryptand with a Cu(I) salt under the protection of argon. In all cases the isolated creamy or white solid acquires a greenish color on standing in air over a period of time depending on the cryptand, and is oxidized more rapidly to the Cu(II) state in solution. With **RL4** and **RL5** as the ligand, the dicopper(I) complex can not be isolated with acceptable purity. The air-sensitivity of these dicopper(I) complexes prevented the acquisition of NMR spectra.

The dicopper(I) complex $[Cu_2\mathbf{RL2}][BF_4]_2$ is also susceptible to attack by carbon monooxide. On bubbling CO through an MeCN/MeOH solution of $[Cu_2\mathbf{RL2}][BF_4]_2$ a white precipitate $[Cu_2\mathbf{RL2}(CO)][BF_4]_2$ has been obtained. It shows an infrared absorption at 2065 cm^{-1}, suggesting terminally bonded CO. This product has greater redox stability than the parent dicopper(I) complex, retaining its pale yellow color in solution for around an hour while the latter acquires a greenish color within seconds. Similarly, the solid product $[Cu_2\mathbf{RL2}(CO)][BF_4]_2$ can be stored in air for months while $[Cu_2\mathbf{RL2}][BF_4]_2$ turns green within days. This is expected since CO is known as a weak Lewis acid that is capable of accepting an appreciable amount of $d\pi$-electron density from transition metal ions into its π or π * orbitals.

Dicopper(II) complexes with or without different bridging ligands have been synthesized by reactions of Cu(II) salts with **RL1**-**RL4** in the absence or presence of appropriate bridging ligands. With **RL1**-**RL3**, three kinds of dicopper(II) complexes

with three different bridging ligands were obtained: they are $[Cu_2RL(OH)]X_3$, $[Cu_2RL(im)]X_3$, and $[Cu_2RL(N_3)]X_3$ (**RL** = **RL1**, **RL2**, **RL3**; X = ClO_4^-, $O_3SCF_3^-$). With **RL4**, attempts to synthesize dicopper(II) complexes with hydroxo- or imidazolate-bridge failed. Instead, the bright blue tetracationic $[CuRL4][ClO_4]_4$ has been isolated as the only product. $[Cu_2RL4(N_3)][ClO_4]_3$ has been readily synthesized. It has different spectroscopic properties from the other azido-bridged dicopper(II) complexes.

4.2 X-ray crystal structures

$[Cu_2RL2(OH)][O_3SCF_3]_3$. Figure 4.1 illustrates siting and geometry of the Cu-O(H)-Cu entity within the cryptand **RL2**. Selected bond lengths and angles are listed in Table 4.1.Each copper(II) ion coordinates to four amino nitrogen donors including the bridgehead, and the oxygen donor from the bridging hydroxide anion. The furan oxygen atoms are not coordinated to either copper(II) ion but there is one hydrogen bond formed between one of the furan oxygen atoms and the hydroxo-bridge [O(1) · · · O(11) 2.819(7) Å]. The coordination geometries around both copper(II) ions are almost trigonal bipyramid, although the copper(II) ions lie slightly out of the trigonal plane

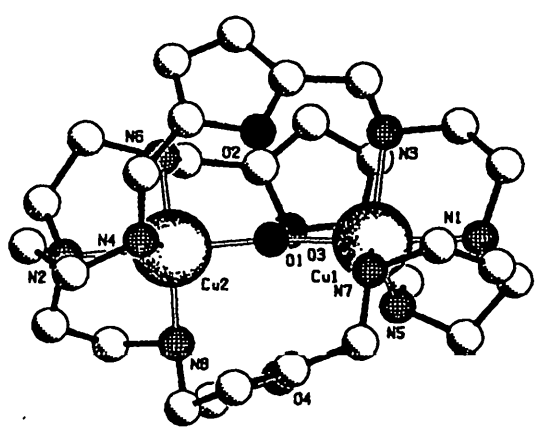

Figure 4.1 Structure of the cation of $[Cu_2RL2(OH)][O_3SCF_3]_3$

(0.222 and 0.277 Å) towards the direction of the hydroxo-bridge. The axial donors, bridgehead nitrogen and bridging hydroxide oxygen form shorter bonds to Cu(II) ions than the equatorial nitrogen donors. The Cu-O(H)-Cu angle is 174° which is virtually linear. The Cu(II) – Cu(II) distance of 3.900(1) Å is surprisingly long in terms of single-atom bridge, but it meets the requirement of a linear geometry.

Table 4.1 Selected bond lengths (Å) and angles (°) for $[Cu_2\mathbf{RL2}(OH)][O_3SCF_3]_3$

Cu(1)-O(1)	1.957(4)	Cu(1)-N(1)	2.075(5)
Cu(1)-N(31)	2.129(5)	Cu(1)-N(21)	2.144(5)
Cu(1)-N(11)	2.173(5)	Cu(2)-O(1)	1.948(4)
Cu(2)-N(2)	2.074(5)	Cu(2)-N(32)	2.130(5)
Cu(2)-N(22)	2.149(5)	Cu(2)-N(12)	2.182(6)
O(1)-Cu(1)-N(1)	178.0(2)	O(1)-Cu(1)-N(31)	97.0(2)
N(1)-Cu(1)-N(31)	83.7(2)	O(1)-Cu(1)-N(21)	96.8(2)
N(1)-Cu(1)-N(21)	84.3(2)	N(31)-Cu(1)-N(21)	124.9(2)
O(1)-Cu(1)-N(11)	93.8(2)	N(1)-Cu(1)-N(11)	84.2(2)
N(31)-Cu(1)-N(11)	116.9(2)	N(21)-Cu(1)-N(11)	114.9(2)
O(1)-Cu(2)-N(2)	178.8(2)	O(1)-Cu(2)-N(32)	96.7(2)
N(2)-Cu(2)-N(32)	84.4(2)	O(1)-Cu(2)-N(22)	96.2(2)
N(2)-Cu(2)-N(22)	83.2(2)	N(32)-Cu(2)-N(22)	119.0(2)
O(1)-Cu(2)-N(12)	95.2(2)	N(2)-Cu(2)-N(12)	84.2(2)
N(32)-Cu(2)-N(12)	121.9(2)	N(22)-Cu(2)-N(12)	115.8(2)
Cu(2)-O(1)-Cu(1)	174.0(3)		

$[Cu_2\mathbf{RL3}(im)][ClO_4]_3$. In this cryptate the bridging imidazolate ring is sandwiched between the phenyl rings (Figure 4.2). These three rings are almost parallel, but are offset by about 1.4 Å with respect to each other. They exhibit a parallel offset π-π attractive interaction as defined by Hunter and Sanders [97], with an unusually short stacking distance of 3.05 Å. The third phenyl ring is almost perpendicular to the other three rings (79.2, 80.6, 86.4° respectively). The conformation of the molecule places this ring in another energetically favorable position to one of the stacked aromatic rings: edge-to-face with an H · · · ring- plane distance of 3.15 Å. Selected bond lengths and angles are listed in Table 4.2.

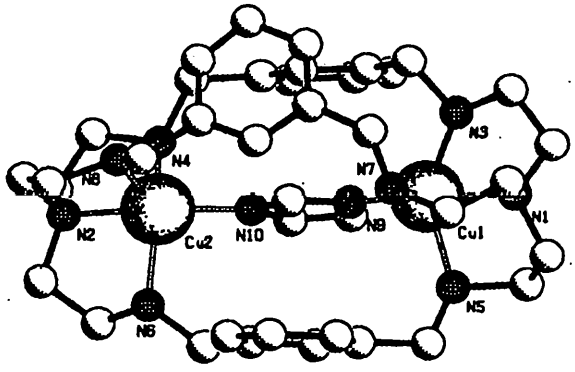

Figure 4.2 Structure of cation of $[Cu_2\mathbf{RL3}(im)][ClO_4]_3$

The coordination geometry around each Cu(II) is distorted trigonal-bipyramidal. The longest Cu-N bond is the one between Cu(II) and the nitrogen atom from the strand containing the non-stacked aromatic ring (ca. 2.3 Å). At Cu(1) no bond angle deviates by more than 15 ° from ideal trigonal-bipyramidal geomotry, with N(1) and N(9) at axial

positions. The geometry around Cu(2) is somewhat closer to square-pyramidal, with N(8) at the apical position.

Table 4.2 Selected bond lengths (Å) and angles (°) for $[Cu_2\mathbf{RL3}(im)][ClO_4]_3$

Cu(1)-N(9)	1.93(2)	Cu(2)-N(10)	1.96(2)
Cu(1)-N(1)	2.02(2)	Cu(2)-N(2)	2.01(2)
Cu(1)-N(3)	2.10(2)	Cu(2)-N(4)	2.09(2)
Cu(1)-N(5)	2.111(14)	Cu(2)-N(6)	2.10(2)
Cu(1)-N(7)	2.251(14)	Cu(2)-N(8)	2.32(2)
N(9)-Cu(1)-N(1)	170.8(6)	N(10)-Cu(2)-N(2)	169.1(7)
N(9)-Cu(1)-N(3)	93.3(7)	N(10)-Cu(2)-N(4)	92.0(7)
N(1)-Cu(1)-N(3)	84.5(7)	N(2)-Cu(2)-N(4)	84.38)
N(9)-Cu(1)-N(5)	90.1(7)	N(10)-Cu(2)-N(6)	94.2(7)
N(1)-Cu(1)-N(5)	84.3(7)	N(2)-Cu(2)-N(6)	83.9(7)
N(3)-Cu(1)-N(5)	128.1(6)	N(4)-Cu(2)-N(6)	143.8(7)
N(9)-Cu(1)-N(7)	103.5(6)	N(10)-Cu(2)-N(8)	108.6(7)
N(1)-Cu(1)-N(7)	83.7(6)	N(2)-Cu(2)-N(8)	82.2(6)
N(3)-Cu(1)-N(7)	113.9(6)	N(4)-Cu(2)-N(8)	104.6(7)
N(5)-Cu(1)-N(7)	114.9(6)	N(6)-Cu(2)-N(8)	107.0(7)

4.3 Electrochemical behavior

The oxidation state preference of copper within the hexaimino cryptands and octaamino cryptands are markedly different. As we have discussed, the dicoppper(I) complexes of hexaimino cryptands are readily obtained and are stable towards attack of oxygen, especially in the solid state. However, the analogous complexes of copper(I) with octaamino cryptands are so easily oxidized that only dicopper (I) complexes of **RL1**, **RL2**, and **RL3** can be isolated with acceptable purity under the protection of argon. The only cyclic voltammograms obtained for dicopper(I) complexes are for $[Cu_2\mathbf{RL1}][BF_4]_2$ and $[Cu_2\mathbf{RL2}][ClO_4]_2$. Both give a single two-electron irreversible wave with Ea = 30 mV for $[Cu_2\mathbf{RL1}][BF_4]_2$ and Ea = -97 mV for $[Cu_2\mathbf{RL2}][ClO_4]_2$ versus Fc/Fc^+. Compared to their analogous dicopper(I) complexes of hexaimino cryptands, both complexes show much enhanced stability of the Cu(II) oxidation state. There are two possible reasons for the destabilization of Cu(I) oxidation state in octaamino cryptands. Firstly, the "harder" sp^3 nitrogen donors favor the Cu(II) oxidation state relative to the Cu(I) oxidation state. Secondly, the more flexible octaamino cryptands may not be able to impose a near tetrahedral coordination environment that is favored by the Cu(I) oxidation state.

The cyclic voltammograms of dicopper(II) complexes have been done with $[Cu_2\mathbf{RL4}][ClO_4]_4$ and $[Cu_2\mathbf{RL4}(N_3)][ClO_4]_3$. In contrast to the results obtained on $[Cu_2\mathbf{L4}][BF_4]_2$ where two sequential one-electron oxidation waves have been observed, $[Cu_2\mathbf{RL4}][ClO_4]_4$ only shows a single (fairly broad) two-electron quasi-reversible wave (Figure 4.3 a). This suggests that the Cu-Cu separation in $[Cu_2\mathbf{RL4}][ClO_4]_2$ may be large enough to prevent the two Cu(II) ions from interacting with each other, and the

coordination environments of the two Cu(II) ions are almost identical. The more negative oxidation potential Ea = -546 mV versus Fc/Fc^+, compared to those of $[Cu_2L4][BF_4]_2$ (Ea^1 = -110, and Ea^2 = 60 mV versus Fc/Fc^+), testifies to the increased thermodynamic stability of the Cu(II) oxidation state encapsulated within the octaamino cryptand.

In the case of $[Cu_2RL4(N_3)][ClO_4]_3$, a pair of quasi-reversible oxidation waves (Figure 4.3b) have been observed at –789 and –612 mV, respectively. Recent crystallographic results[98] reveal that the azide anion in this cryptate terminally coordinates to the one of the Cu(II) centers together with four amino nitrogen donors from one of the tren units. Another Cu(II) is also five-coordinated by one of the pyridine nitrogen donors and the four amino nitrogen donors for the second tren unit. The difference in two coordination sites or the shorter Cu-Cu distance caused by the coordination of pyridine nitrogen donor to one of the Cu(II) ions may account for the appearance of two

(a)

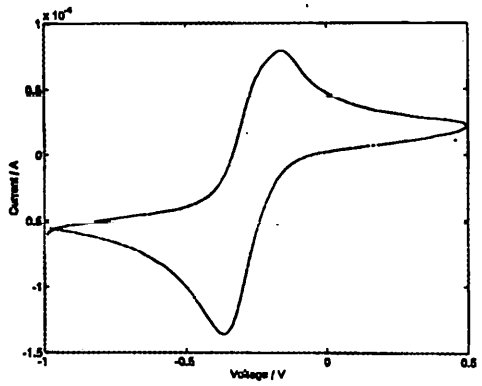

(b)

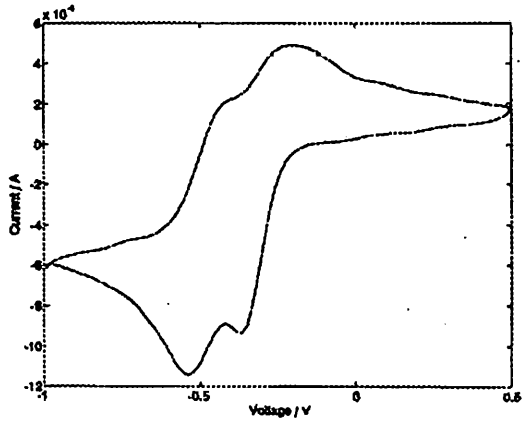

Figure 4.3 Cyclic voltammetry of (a) $[Cu_2\mathbf{RL4}][ClO_4]_4$, (b) $[Cu_2\mathbf{RL4}(N_3)][ClO_4]_3$, potential vs. Ag/AgCl, scan rate 50 mV s^{-1}.

one-electron oxidation waves. The coordination of anionic ligand N_3^- to the Cu(II) ion further stabilizes the Cu(II) oxidation state.

4.4 Bridged dicopper(II) complexes of octaamino cryptands

Octaamino cryptands coordinate two copper(II) ions using two tren units with all sp^3 nitrogen donors, and hold them at a distance and in an arrangement so that the two copper(II)) ions may further bind a bridging ligand in a "cascade' fashion. In this section the spectroscopic and magnetic properties of dicopper(II) complexes of octaamino cryptands **RL1-RL4** containing hydroxo-, imidazolato-, and azido-bridge will be discussed. The interest of these types of complexes lies in their significance as models of biological dimetallic sites and their potential chemical reactivity as dinuclear catalysts.

4.4.1 Hydroxo-bridged dicopper(II) cryptates

Hydroxo-bridged dicopper(II) cryptates have been obtained with **RL1**-**RL3**. The attempt to make hydroxo-bridged dicopper(II) cryptate with **RL4** has failed. Instead the non-bridged complex $[Cu_2\mathbf{RL4}][ClO_4]_4$ has been isolated. In all three hydroxo-bridged dicopper(II) cryptates two *d-d* transition bands at ~ 700 and 850 nm have been observed, indicating a trigonal bipyramidal coordination geometry. In addition they all have an intense $O(H)^- \rightarrow Cu(II)$ charge-transfer band at ~ 370 nm. The familiar magnetic behavior observed in $[Cu_2\mathbf{L2}(OH)][ClO_4]_3$ and $[Cu_2\mathbf{L3}(OH)][ClO_4]_3$ is also seen in $[Cu_2\mathbf{RL2}(OH)][O_3SCF_3]_3$. Variable temperature magnetic susceptibility investigation shows a tiny room-temperature magnetic moment, which reduces further on cooling to 4 K (Figure 4.4). The increase in susceptibility at very low temperature indicates a paramagnetic impurity, estimated from the data at 4 K as 1.3% assuming Curie-law behavior and a g value of 2. Fitting of the data to the Bleaney-Bowers equation (including the impurity)[99] yields a magnetic exchange constant, -2J of -880 ± 70 cm^{-1}. In agreement with this large J value, the EPR spectrum in frozen solution shows only ill defined absorption associated with the small proportion of paramagnetic impurity. It is known from the X-ray structural results that the Cu-O(H)-Cu linkage in this complex is almost co-linear (Cu-O(H)-Cu: 174°). Such linearity is believed to allow the most advantageous overlap between the d_z^2 magnetic orbital of the Cu(II) ions and the $2p_z$ magnetic orbital of the hydroxo-bridge, rationalizing the efficient antiferromagnetic exchange observed by magnetic susceptibility and EPR measurement. Due to the similarity of the magnetic and spectroscopic behaviors of $[Cu_2\mathbf{RL2}(OH)][O_3SCF_3]_3$ to those of $[Cu_2\mathbf{L2}(OH)][ClO_4)_3$ and $[Cu_2\mathbf{L3}(OH)][ClO_4]_3$, the established near-linearity of

the Cu-O(H)-Cu linkage in $[Cu_2RL2(OH)][O_3SCF_3]_3$ can be extrapolated to the latter two complexes.

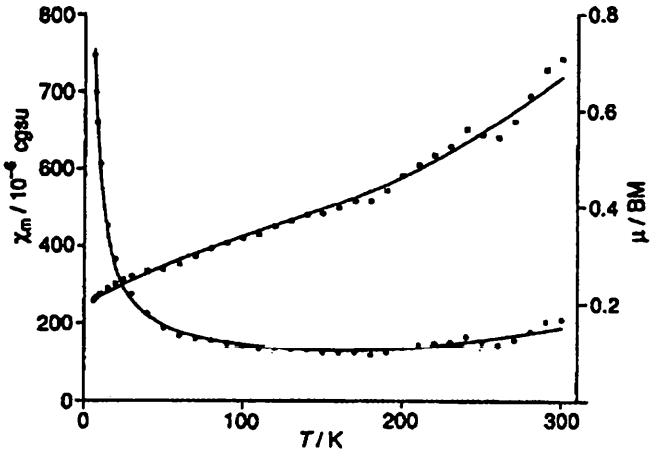

Figure 4.4 Temperature variation of magnetic susceptibility and effective magnetic moment for $[Cu_2RL2(OH)][O_3SCF_3]_3$ assuming $g = 2.07$, $N_\alpha = 95 \times 10^{-6}$ cgsu per Cu ion, $-2J = (880 \pm 70)$ cm^{-1}. Calculated curves —; χ_m (experimental) •; μ (experimental) •.

Complexes $[Cu_2RL1(OH)][ClO_4]_3$ and $[Cu_2RL3(OH)][ClO_4]_3$ are alike in terms of their magnetic and EPR behavior. Magnetic susceptibility measurements reveal the lack of strong antiferromagnetic interaction in both complexes ($-2J$ *ca* 72 cm^{-1} for $[Cu_2RL1(OH)][ClO_4]_3$, 46 cm^{-1} for $[Cu_2RL3(OH)][ClO_4]_3$), suggesting that the Cu-O(H)-Cu linkage held within **RL1** or **RL3** is not co-linear. The steric hindrance caused by the large sulfur atoms from thiophene groups in **RL1** or the $H_{A'}$ protons from the

phenyl groups in **RL3** may be responsible for the non-linearity of Cu-O(H)-Cu linkage held within the **RL1** and **RL3** cavities.

Even though the non-linearity of Cu-O(H)-Cu linkage has been found in $[Cu_2RL3(OH)][ClO_4]_3$, the co-linear disposition of the Cu-O(H)-Cu linkage in $[Cu_2L3(OH)][ClO_4]_3$, may however, be enforced by the rigid cryptand **L3**, even in the presence of steric hindrance from $H_{A'}$ protons of phenyl groups. The steric strain in this cryptate makes it unstable in solution: the initially bright green solution of $[Cu_2L3(OH)][ClO_4]_3$ develops a blue color on standing, indicating a change of coordination geometry upon hydrolytic ring-opening. On the other hand, the more flexible **RL3** may adopt an asymmetric conformation in $[Cu_2RL3(OH)][ClO_4]_3$ which involves significant bending of the Cu-O(H)-Cu linkage, in order to avoid the close contact of the $H_{A'}$ protons.

4.4.2 Imidazolato-bridged dicopper(II) cryptates

Imidazole (Him), a five-membered nitrogen heterocycle, is a ubiquitous ligand in chemical and biological systems. It occurs in proteins as part of the side chain of the amino acid histidine[100], in nucleic acid structures as part of the purine ring of adenine and guanine[101] and in the vitamin B12 coenzyme as benzimidazole[102]. In these systems the imidazole functions in a variety of roles: for example, as a proton donor and/or acceptor site for hydrogen bonding, as a specific/general base or nucleophilic catalyst, or as a site of metal ion coordination[103]. The imidazole moiety of histidyl residues in a large number of metalloproteins constitute all or part of the binding sites of various transition metal ions such as Mn^{2+}, $Fe^{2+,3+}$, $Cu^{+,2+}$, and Zn^{2+} [104]. Thus, structural and spectroscopic

studies that characterize the bonding between imidazole and transition metal ions are of considerable interest.

An imidazolato-bridge is readily accommodated between the copper(II) ions encapsulated in the cryptands **RL1-RL3**. Attempts to synthesize imidazolato-bridged dicopper(II) complex with **RL4** have failed. The electronic spectra of the three imidazolato-bridged complexes isolated suggest coordination geometries intermediate between square pyramidal and trigonal bipyramidal, which has been confirmed by the X-ray structural results of $[Cu_2\mathbf{RL3}(im)][ClO_4]_3$. Moderately strong antiferromagnetic interaction is mediated via the heterocyclic bridge, having $-2J$ of 122 cm^{-1} for $[Cu_2\mathbf{RL1}(im)][O_3SCF_3]_3$, 92 cm^{-1} for $[Cu_2\mathbf{RL2}(im)][ClO_4]_3$, and 111 cm^{-1} for $[Cu_2\mathbf{RL3}(im)][ClO_4]_3$ (Figure 4.5). All three complexes exhibit similar EPR spectra,

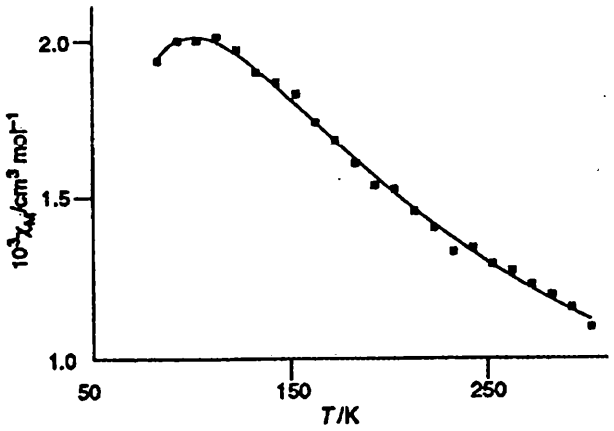

Figure 4.5 Temperature variation of magnetic susceptibility for $[Cu_2\mathbf{RL3}(im)][ClO_4]_3$ assuming $g = 2.05$, TIP = 80×10^{-6} cgsu per Cu ion, $-2J = 111 cm^{-1}$. Calculated curve —; experimental values •.

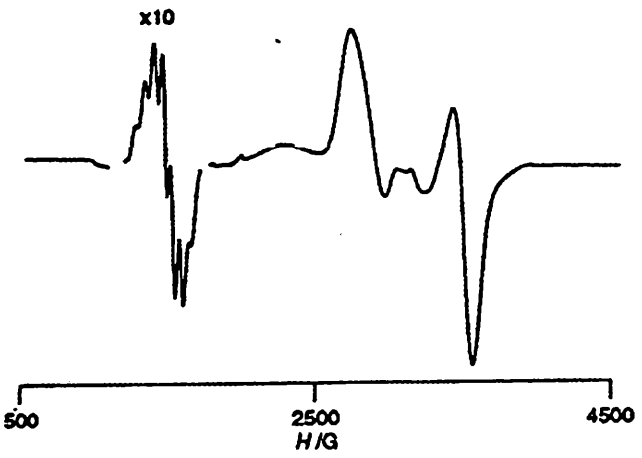

Figure 4.6 The X-band EPR spectrum of $[Cu_2$**RL3**$(im)][ClO_4]_3$ as a DMF glass at 100 K.

showing significant zero-field splitting (D ≈ 900 G) and a weaker half-band which is well resolved into seven lines in $[Cu_2$**RL2**$(im)][ClO_4]_3$ and $[Cu_2$**RL3**$(im)][ClO_4]_3$ (Figure 4.6), giving hyperfine-splitting coupling constant A of about 60 G.

It is believed that the interaction between the copper ions through the imidazolato-bridge may be explained in terms of a σ- and/or a π-exchange pathway. For dicopper(II) complexes with square pyramidal coordination geometry, the magnetic orbitals are σ-antibonding, and thus the relevant exchange pathway through the imidazolato-bridge is of the σ-type[105]. On the basis of theoretical calculations[106], it has been demonstrated that a maximum value of J is obtained when the Cu-N_{im} bonds are parallel to the imidazolate C-C bond (Scheme 1), therefore favoring an σ-exchange pathway. The crystal structure of $[Cu_2$**RL3**$(im)[ClO_4]_3$ shows that the Cu-N_{im}- -N_{im} angles are not very far from 180 °[165 ° for Cu(1), 164 ° for Cu(2)], which may also be

true in $[Cu_2\mathbf{RL1}(im)][O_3SCF_3]_3$ and $[Cu_2\mathbf{RL2}(im)][ClO_4]_3$ since they all show relatively strong antiferromagnetic interaction.

Scheme 1

4.4.3 Azido-bridged dicopper(II) cryptates

Metal complexes with azido-bridges are of great interest due to the broad range of their structural and magnetic properties[107]. The azide can bridge two metal ions either in a bent end-to-end fashion (1), or in an end-on fashion (2), or in a linear end-to-end fashion (3)[108,109]. Extensive experimental and theoretical work has been directed towards a detailed understanding of the magneto-structural correlations in azido-bridged dinuclear metal complexes[110-114].

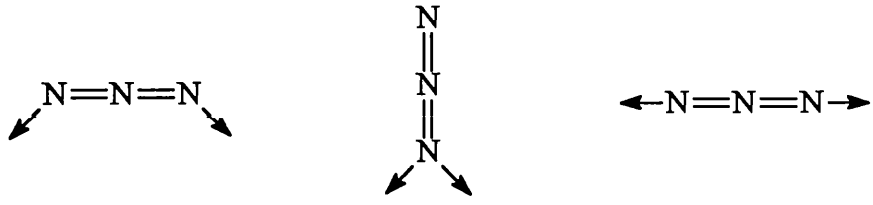

(1) (2) (3)

Moreover, azido-bridged dicopper(II) systems have been studied as structural models for copper-containing enzymes involved in the reversible binding and activation of dioxygen, such as in hemocyanin (Hc)[114, 115]. Three azido-bridged dicopper(II) cryptates have been obtained with **RL1-RL3**. Distorted trigonal bipyramidal coordination geometry has been found in all these three complexes as judged by their *d-d* transition bands ($[Cu_2\mathbf{RL1}(N_3)][ClO_4]_3$: 740, 900 nm; $[Cu_2\mathbf{RL2}(N_3)][O_3SCF_3]_3$: 660, 900 nm; $[Cu_2\mathbf{RL3}(N_3)][O_3SCF_3]_3$: 710, 858 nm). Similar magnetic and spectroscopic behavior has also been observed in these complexes, although the $N_3^- \rightarrow$Cu(II) charge-transfer absorption of $[Cu_2\mathbf{RL3}(N_3)][O_3SCF_3]_3$ appears at higher energy (404 nm) than those of $[Cu_2\mathbf{RL1}(N_3)][ClO_4]_3$ (465 nm) and $[Cu_2\mathbf{RL2}(N_3)][O_3SCF_3]_3$ (460 nm). They all have infrared ν_{as} (N_3^-) absorption around 2200 cm^{-1}, which is at much higher frequency than that observed for azido-bridging either in an end-on or a bent end-to-end mode. The EPR spectral signals spread over 5-6 kG due to very large zero-field splitting with an intense feature at very low field ($g \approx 8$ for $[Cu_2\mathbf{RL1}(N_3)][ClO_4]_3$, $g \approx 7$ for $[Cu_2\mathbf{RL2}(N_3)][O_3SCF_3]_3$ (Figure 4.7) and $g \approx 6$ for $[Cu_2\mathbf{RL3}(N_3)][O_3SCF_3]_3$.In addition, magnetic susceptibility measurements show the presence of weak ferromagnetic interaction with $-2J$ about -5 cm^{-1} for $[Cu_2\mathbf{RL1}(N_3)][ClO_4]_3$, -4 cm^{-1} for $[Cu_2\mathbf{RL2}(N_3)][O_3SCF_3]_3$, and -25 cm^{-1} for $[Cu_2\mathbf{RL3}(N_3)][O_3SCF_3]_3$. Recent results[116] on $[Cu_2\mathbf{RL3}(N_3)][ClO_4]_3$ reveal that the J value of this complex reflects the total interaction of intramolecular ferromagnetic exchange and intermolecular antiferromagnetic exchange, even though there is no evidence of intermolecular interaction in $[Cu_2\mathbf{RL3}(N_3)][O_3SCF_3]_3$. X-ray structural results for $[Cu_2\mathbf{RL3}(N_3)][ClO_4]_3$[112] confirm the existence of colinear Cu-NNN-Cu geometry, which

is believed to be the origin of the unusual spectroscopic properties observed in azido-bridge dicopper(II) cryptates of **RL1-RL3**. It is believed that the colinear Cu-NNN-Cu linkage also exists in $[Cu_2L3(N_3)][O_3SCF_3]_3$ because of the similarity of its spectroscopic properties to those of the azido-bridged dinuclear Cu(II) complexes of **RL1-RL3**.

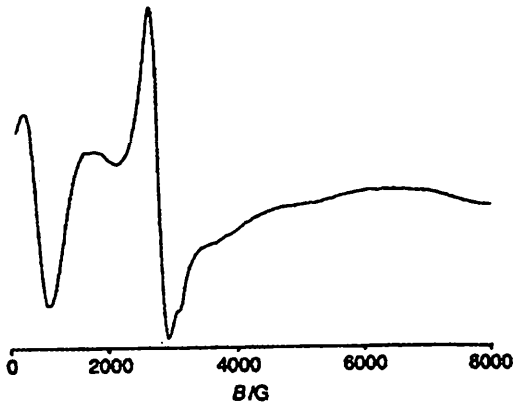

Figure 4.7 The X-band EPR spectrum of $[Cu_2RL2(N_3)][O_3SCF_3]_3$ as a polycrystalline solid at 100 K.

4.5 Preliminary results on catalytic oxidation with dicopper cryptates

The investigation of dinuclear copper complexes which interact with dioxygen has been extensive because of their relevance to biological systems and their applications as oxidation catalysts for laboratory and industrial use.[117] A number of dinuclear coppe(I) complexes of acyclic and macrocyclic ligands have been studied for oxygenated complex formation.[117-120] One of the most significant advances is the structural elucidation of an oxygenated dicopper model complex by Kitajima et al.[46], which led to a reinterpretation of the mechanism at the active sites of oxyhemocyanin.

In order to find out if dicopper (I) complexes of octaamino cryptands, which are very sensitive to oxygen, offer better catalytic reactivity than those of acyclic and macrocyclic ligands, the oxidation of 3,5-di-t-butylcatehol (3,5-DTBC), a two-electron reducing agent, with oxygenated dicopper(I) complexes of **RL2** and **RL3**, and hydroxo-

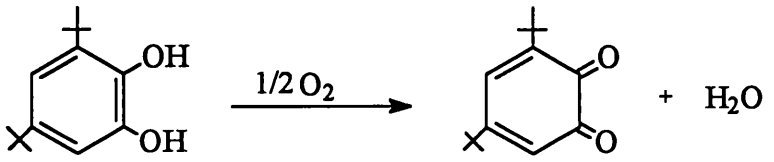

3,5-DTBC 3,5-DTBQ

bridged dicopper(II) complexes of **RL2** and **RL3** have been investigated. For the purpose of comparison $Cu(ClO_4)_2$ and a dicopper(I) complex of a macrocyclic ligand are also included in the investigation. Preliminary results of oxidation reaction are listed in Table 4.3.

It is seen from Table 4.3 that 3,5-DTBC can be oxidized by both the dicopper(I) and dicopper(II) complexes of **RL2** and **RL3** in the presence oxygen, a necessity to complete the catalytic cycle. However, even though dicopper complexes of octaamino cryptands show some catalytic reactivity in comparison to uncomplexed Cu(II) ion, their reactivities are much lower than that of the dicopper(I) complex of macrocyclic **L** which has only two nitrogen donors coordinating to each Cu(II) ion. It is generally believed that coordinative unsaturation of a Cu center is an advantage in redox catalysis. The poor catalytic reactivity shown by dicopper complexes of **RL2** and **RL3** may result from the coordination saturation of Cu centers in the oxygenated and hydroxo-bridged dicopper(II) cryptates, which prevents the substrate from binding to the copper center.

Another possibility in lowering the catalytic reactivity may be the macrobicyclic structure, which renders access of substrate to the active center more difficult.

Table 4.3 Oxidation reaction with copper complexes

Complexes (0.001M)	Substrate (0.01M)	Yield of product (%) (after 18 hr)
$Cu(ClO_4)_2$	3,5-DTBC	7
$[Cu_2(I)\mathbf{L}][ClO_4]_2$		50 (in 10 min.)
$[Cu_2(I)\mathbf{RL2}][ClO_4]_2$		92
$[Cu_2(II)\mathbf{RL2}(OH)][ClO_4]_2$		44
$[Cu_2(I)\mathbf{RL3}][ClO_4]_2$		18
$[Cu_2(II)\mathbf{RL3}(OH)][ClO_4]_2$		24

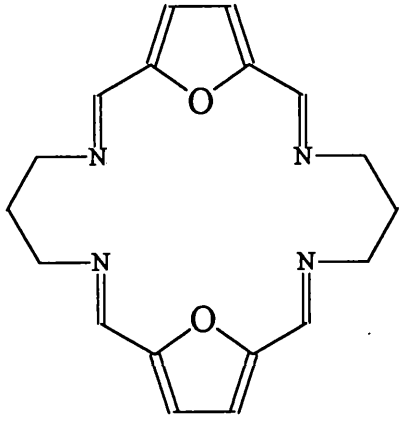

L

Scheme 2

4.6 Conclusions

Upon reduction of hexaimino cryptands **L1-L4**, the hydrolytically-inert octaamino cryptands **RL1-RL4** have been obtained. These ligands favor the Cu(II) oxidation state relative to the Cu(I) oxidation state due to the presence of eight "harder" sp^3 nitrogen donors and their flexibility in adopting coordination environments around Cu ion other than trigonal/tetrahedral geometry. The formation of bridged dicopper(II) complexes of octaamino cryptands by incorporating anionic bridging ligands further stabilizes the Cu(II) oxidation state and at the same time offers a broad range of structural, spectroscopic, and magnetic properties.

The cryptand **RL4** is unique compared to **RL1**, **RL2**, and **RL3**. In addition to having eight sp^3 nitrogen donors from the two tren units, it also has three sp^2 nitrogen donors from pyridine spacer groups. The coordination of the Cu(II) ion by the pyridine nitrogen donor excludes the formation of bridged dicopper(II) complexes of **RL4**, which is confirmed by the crystal structure of $[Cu_2\mathbf{RL4}(N_3)][ClO_4]_3$.

The preliminary results on oxidation reactions of 3,5-DTBC with dicopper complexes of **RL2** and **RL3** indicate that combined factors of the coordination saturation around Cu ions and the macrobicyclic structure may be responsible for the poor catalytic activity.

REFERENCES

1. F. A. Cotton, *Advanced Inorganic Chemistry*, Fifth ed., Wiley, New York, **1988**.
2. E. I. Solomon, M. J. Baldwin and M. D. Lowery, *Chem. Rev.*, **1992**, 92, 521.
3. N. Kitajima, *Advances in Inorg. Chem.*, **1992**, 39, 1.
4. J. M. Guss, H. D. Bartllnk and H. C. Freeman, *Acta Crystallogr.*, **1992**, B48, 790.
5. K.W. Penfield, R. R. Gay R.S. Himmelwright, N. C. Eickman, V. A. Norris, H. C. Freeman and E. I. Solomon, *J. Am. Chem. Soc.*, **1981**, 103, 4382.
6. E. I. Solomon, J. W. Hare, D. M. Dooley, J. H. Dawson and H. B Gray, *J. Am. Chem. Soc.*, **1980**, 102, 168.
7. E. I. Solomon, J. W. Hare and H.B. Gray, *Proc. Natl. Acad. Sci.*, U.S.A.**1976**, 73, 1389.
8. C. A. Collyer, J. M . Guss and H.C. Freeman, *J. Mol. Biol.*, **1990**, 211, 617.
9. E. N. Baker, *J. Mol. Biol.*, **1988**, 203, 1071.
10. W. E. B. Shepard, B.F. Anderson, D. A. Lewandoski, G. E. Norris and E. N. Baker, *J. Am. Chem. Soc.*, **1990**, 112, 7817.
11. H. Nar, A. Messerschmidt, R. Huber, M. van de Kamp and G. W. Canters, *J. Mol. Biol.*, **1991**, 221, 765.
12. D. W. Zhu, T. Dahms, K. Willis, A. G. Szabo and X. Lee, *Arch. Biochem. Biophys.*, **1994**, 308.
13. C. L. Coyle, W. G. Zumft, P. M. H. Kroneck, H. Korner and W. Jakob, *Eur. J. Biochem.*, **1985**, 153, 459.
14. J. W. Godden, S. Turley, D. C. Teller, E. T. Adman, M. Y. Liu and W. J. Payne, J. LeGall, *Science*, **1991**, 253.

15. H. Jin, H. Thomann, C. L. Coyle and W. G. Zumft, *J. Am. Chem. Soc.*, **1989**, 111, 4262.

16. A. Messerschmidt, R. Ladenstein, R. Huber, M. Bolognesi, L. Avigliano, R. Petruzzelli, A. Rossi and A Finazzi-Agro, *J. Mol. Biol.*, **1992**, 224, 197.

17. W. E. Blumberg and J Peisach, *Biochim. Biophys. Acta*, **1966**, 126, 269.

18. A. S. Brill and G. F. Bryce, *J. Chem. Phys.*, **1968**, 48, 4398.

19. J. A. Fee, *Struct. Bonding.*, Berlin, **1975**, 23, 1.

20. H. B. Gray and E. I. Solomon, In *Copper Proteins*, T.G. Spiro, Ed., Wiley: New York, 1981.

21. E. I. Solomon, In *Copper Coordination Chemistry: Biochemical and Inorganic Perspectives*, K. Karlin and J. Zubieta, Eds., Adenine Press: Guilderland, NY, 1982.

22. E. I. Solomon, K. W. Penfield and D. E. Wilcox, *Struct. Bonding* (Berlin) 1983, 53, 1.

23. R. Dorfman, R. Bereman and M. Whango, In *Copper Coordination Chemistry: Biochemical and Inorganic Perspectives*, K. Karlin and J. Zubieta, Eds., Adenine Press: Guilderland, NY, 1982.

24. D. F. Blair, G. W. Campbell, J. R. Schoonover, S. I. Chan, H. B. Gray, B. G. Malmstrom, I. Pecht, B. I. Swanson, W. H. Woodruff, W. K. Cho, A. M. English, H. A. Fry, V. Lum and K. A. Norton, *J. Am. Chem. Soc.*, **1985**, 107, 5755.

25. J. E. Roberts, J. F. Cline, V. Lum, H. C. Freeman, H. B. Gray, J. Reisach, B. Reinhammer and B. Hoffman, *J. Am. Chem. Soc.*, **1984**, 106, 5324.

26. R. A. Scott, J. E. Hahn, S. Boniach, H. C. Freeman and K. O. Hodgson, *J. Am. chem. Soc.*, **1985**, 107, 5755.

27. K. W. Penfield, A. A. Gewircth and E. I. Solomon, *J. Am. Chem, Soc.*, **1985**, 107, 4519.

28. S. E. Shadle, J. E. Penner-Hahn, H. J. Schugar, B. Headman, K. O. Hodgson and E. I. Solomon, *J. Am. Chem. Soc.*, **1993**, 115, 767.

29. S. J. George, M. D. Lowery, E. I. Solomon and S. P. Cramer, *J. Am. Chem. Soc.*, **1993**, 115, 2968.

30. A. A. Gewirth and E. I. Solomon, *J. Am. Chem. Soc.*, **1988**, 110, 3811.

31. P. Zanello, *Comm. Inorg. Chem.* **1988**, 8, 45.

32. M. A. Augustin, J. K. Yandell, A. W. Addison and K. D. Karlin, *Inorg. Chem. Acta*, **1981**, 55, L35.

33. K. D. Karlin and J. K. Yandell, *Inorg. Chem.*, **1984**, 23, 1184.

34. U. Sokaguchi and A. W. Addison, *J. Chem. Soc., Dalton Trans.*, **1979**, 600.

35. R. Lumry and H. Eyring, *J. Phys. Chem.*, **1954**, 58, 110.

36. R. J. P. Williams, *J. Mol. Catal.*, **1985**, 30, 1.

37. B. G. Malmström, *Eur. J. Biochem.*, **1994**, 223, 711.

38. H. B. Gray and B. G. Malmström, *Inorg, Chem.*, **1983**, 11, 203.

39. *Structure and Function of Hemocyanin*; J. V. Bannister, Ed.; Springer-Verlag: Berlin, 1977.

40. T. B. Freedman, J. S. Loehr and T. M. Loehr, *J. Am. Chem. Soc.*, **1976**, 98, 2809.

41. T. J. Thamann, J. S. Loehr and T. M. Loehr, *J. Am. Chem. Soc.*, **1977**, 99, 4187.

42. K. W. Nickerson and K. E. van Holde, *Comp, Biochem. Physiol.*, **1971**, 390, 855.

43. (a) A. Volbeda and W. G. J. Hol, *J. Mol. Biol.*, **1989**, 206, 531. (b) A. Volbeda and W. G. J. Hol, *J. Mol. Biol.*, **1989**, 209, 249.

44. B. Hazes, K.A.Magnus, C. J. Bonaventura, Z.Dauter, K. H. Kalk and W. G. J. Hol, *Protein Sci.*, **1993**, 2, 597.

45. K. A. Magnus, H. Ton - That and J. E. Carpenter, *Bioinorganic Chemistry of Copper*, K. D. Karlin, Z. Tykelar; Eds., Chapman & Hall: New York, **1993**.

46. (a) N. Kitajima, K. Fujisawa, Y. Moro-oka and K. J. Toriumi, *J. Am. Chem. Soc.*, **1989**, 111, 8975. (b) N. Kitajima, K. Fujisawa, C. Fujimoto, Y. Moro-oka, S. Hashimoto, T. Kitagawa, K. Toriumi, K. Tatsumi and A. Nakamura, *J. Am. Chem. Soc.*, **1992**, 114, 1277.

47. E. I. Solomon, F. Tuczek, D. E. Root and C. A. Brown, *Chem. Rev.*, **1994**, 94, 3827.

48. R. S. Himmelwright, N. C. Eickman, C. D. LuBien, K. Lerch and E. I. Solomon, *J. Am. Chem. Soc.*, **1980**, 102, 7339.

49. D. E. Wilcox, A. G. Porras, Y. T. Hwang, K. Lerch, M. E. Winkler and E. I. Solomon, *J. Am. Chem. Soc.*, **1985**, 107, 4015.

50. E. I. Solomon, M.D. Lowery, D. E. Root and B. L. Hemming, Mechanistic *Bioinorganic Chemistry, Advances in Chemistry Series*, 246, H. H. Thorp, V. L. Pecoraro, Eds; 1995.

51. J. L. Cole, P. A.Clark and E. I. Solomon, *J. Am. Chem, Soc.*, **1990**, 112, 9534.

52. B. G. Malmström, In *New Trends in Bioinorganic Chemistry*; R. J. P. Williams and R. J. R. F. DaSilva, Eds., Academic: London, 1978.

53. B. Reinhammar, In *Copper Proteins and Copper Enzymes*; R. Lontie, Ed., CRC Press: Boca Raton, **1984**, Vol III.

54. A. Finazzi-Agro, *Life Chem Rep*, **1987**, 5, 199.

55. L. Ryden, In *Copper Proteins and Copper Enzymes*: R. Lontie, Ed., CRC Press: Boca Raton, **1984**, Vol III.

56. A. Messerschmidt, A. Rossi, R. Ladenstein, R. Huber, M. Bolognesi, G. Gatti, A. Marchesini, R. Petruzzeli and A. Finazzi-Agro, *J. Mol. Biol.*, **1989**, 206, 513.

57. A. Messerschmidt, H. Luecke, and R. Huber, *J. Mol. Biol.*, **1993**, 230, 997.

58. B. Dietrich, P. Viout and J.-M. Lehn, *"Macrocyclic Chemistry"*, Transl: W. E. Douglas, VCH, 1992.

59. J. -M. Lehn, In *"Supramolecular Chemistry"*, Ed.: U. Anton, VCH, 1995, Berlin.

60. J. -M. Lehn, *Structure and Bonding*, **1973**, 16, 1.

61. J. -M. Lehn, *Acc. Chem. Res.*, **1978**, 11, 49.

62. J. Nelson, V. Mckee, and G. Morgan, *Progr. Inorg. Chem.*, **1998**, 47, 167, and references cited therein.

63. J. –M. Lehn, *Pure Appl. Chem.*, **1977**, 49, 857,.

64. J. –M. Lehn, *Pure Appl.Chem.*, **1978**, 50, 871.

65. J. –M. Lehn and F. Montavon, *Helv. Chim. Acta*, **1978**, 61, 67.

66. J. –M. Lehn, Pure Appl. Chem., **1980**, 50, 2441, and references cited therein.

67. J. Jazwinski, J. –M. Lehn, D. Lilienbaum, R. Zeissel, J. Guilheim and C. Pascard, *J. Chem. Soc., Chem. Commun.*, **1987**, 1691.

68. D. McDowell and J. Nelson, *Tetrahedron Lett.*, **1988**, 385.

69. J. M. Griffing and L. F. Salisburg, *J. Am. Chem. Soc.*, **1948**, 70, 3416.

70. A. F. Alenik, K. Noviskii and Zh. Yu, *Org. Khim.*, **1970**, **6**, 2632.

71. D. Jerchel and H.E. Heck, *Liebigs Ann Chem.*, **1958**, 613, 180.

72. Miller, K. Olssen, *Acta Chem. Scand.*, **1981**, B35, 303.

73. G. M. Sheldrick, SHELXS 86, *Acta Crystallogr.*, Sect. A, **1990**, 46, 467.

74. G. M. Sheldrick, *SHELXTL-PC User Manual*, Siemens Analytical X-ray Instruments Inc., Madison, WI, 1990.

75. G. M. Sheldrick, *SHELXL 93*, University of Göttingen, 1993.

76. G. M. Sheldrick, *SHELXTL-PC* (version 4.1), Siemens Analytical X-ray Instruments Inc., Madison, WI, 1989.

77. A. C. Larson, F. L. Lee, Y. Le Page, M. Webster, J. P. Charland and E. I. Gabe, *The NRCVAX Crystal Structure System*, Chemistry Division, NRC Ottawa, Canada K1A 0RG.

78. J. Hunter, J. Nelson, C. J. Harding, M. McCann and V. McKee, *J. Chem. Soc., Chem. Commun.*, **1990**, 1148. C. J. Harding, V. McKee and J. Nelson, *J. Am. Chem. Soc.*, **1991**, 9684.

79. M. G. B. Drew, C. J. Harding, O. W. Howarth, Q. Lu, D. J. Marrs, G. G. Morgan, V. McKee and J. Nelson, *J. Chem. Soc., Dalton Trans.*, **1996**, 3021.

80. Q. Lu, J-M. Latour, C. J. Harding, N. Martin, D. J. Marrs, V. McKee and J. Nelson, *J. Chem. Soc., Trans.*, **1994**, 1471.

81. C. J. Harding, Q. Lu, J. F. Malone, D. J. Marrs, N. Martin, V. McKee and J. Nelson, *J. Chem. Soc., Dalton Trans.*, **1995**, 1739.

82. D. J. Marrs, V. McKee, J. Nelson, Q. Lu and C. J. Harding, *Inorg. Chim. Acta*, **1993**, 195.

83. Q. Lu, V. McKee and J. Nelson, *J. Chem. Soc., Chem. Commun.*, **1994**, 649.

84. D. M. Dowell, V. McKee, M. G. B. Drew and J. Nelson, *Polyhedron*, **1989**, 8, 1143.

85. D. Marrs, V. McKee, J. Nelson and W. Robinson, *Tetrahedron Lett.*, **1989**, 7453.

86. D. F. Farrell, M. G. B. Drew, G. G. Morgan, J. Nelson and V. McKee, *J. Chem. Soc., Dalton Trans.*, submitted.

87. M. G. B. Drew, V. Felix, V. McKee, G. G. Morgan and J. Nelson, *Supramol. Chem.*, **1995**, 5, 281.

88. *Biological and Inorganic Copper Chemistry*, Part 1, K. D. Karlin and J. Zubeita, Eds., Adenine Press:, New York, 1983.

89. J. P. Gisselbrecht and M. Gross, *J. Electroanal. Chem.*, **1981**, 127, 127.

90. S. M. Nelson, F. Esho, A. Lavery and M.G. B. Drew, *J. Am. Chem. Soc.*, **1983**, 105, 5693.

91. P. C. Yates, M. G. B. Drew, J. –T. Grimshaw, K. P. McKillop, S. M. Nelson, P. T. Ndifon, C. A. McAuliffe and J. Nelson, *J. Chem. Soc., Dalton, Trans.*, **1991**, 1973.

92. K. M. Kadish, *Progr. Inorg. Chem.*, **1980**, 34, 435.

93. M. B. Robin and P. Day, *Adv. Chem. Radiochem.*, **1967**, 10, 247.

94. M. Duggan, N. Ray, B. Hathway, G. Tomlinson, P. Brint and K. Pelin, *J. Chem. Soc., Dalton, Trans.*, **1980**, 1342.

95. P. L. Burke, J. A. Osborn, M. –T. Youinou, Y. Angus, R. Louis and R. Wiess, *J. Am. Chem. Soc.*, **1981**, 103, 1273.

96. P. K. Coughlin and S. J. Lippard, *J. Am. Chem. Soc.*, **1981**, 103, 3228.

97. C. A. Hunter and J. K. M. Sanders, *J. Am. Chem. Soc.*, **1990**, 112, 5525; P. Hobza, H. L. Selzle and E. W. Schlag, *J. Am. Chem. Soc.*, **1994**, 116, 3500.

98. Y. Dussart, J. Nelson and V. McKee, *work in progress.*

99. C. J. O'Connor, *Prog. Inorg. Chem.*, **1982**, 29, 203.

100. T.E. Creighton, *Proteins: Structures and Molecular Properties*, Freeman, New York, 1984.

101. W. Saenger, *Principles of Nuclei Acid Structure*, Springer-Verlag, New York, 1984.

102. J. M. Pratt, *Inorganic Chemistry of Vitamin B_{12}*, Academic Press, New York, 1972.

103. H.C. Freeman, In *Inorganic Biochemistry*, G. L. Eichhorn Ed., Elsevier, New York, 1973.

104. J. S. Richardson, K. A. Thomas and D.C. Richardson, *Proc. Natl. Acad. Sci., U.S.A.* **1975**, 72, 1349.

105. P. Chaudhuri, I. Karpenstein, M. Winter, M. Lengen, C. Butzlaff, E. Bill. A. X. Trautwein, U. Flörke and H.-J. Hauptmann, *Inorg. Chem.*, **1993**, 32, 888.

106. M. S. Haddad and D. N. Hendrickson, *Inorg. Chem.*, **1978**, 17, 2622.

107. O. Kahn, *Molecular Magnetism*, VCH, New York, 1993; O. Kahn, In *Magnetostructural Correlations in Exchange Coupled Systems*, R. D. Willett, D. Gatteschi and O. Kahn, Eds., Reidel, Dordrecht, 1985.

108. M.-F. Charlot, O. Kahn, M. Chaillet and C. Larriea, *J. Am. Chem. Soc.*, **1986**, 108, 2674.

109. C. J. Harding, F. E. Mabbs, E. J. L. MacInnes, V. McKee and J. Nelson, *J. Chem. Soc., Dalton Trans.*, **1996**, 3227.

110. J. E. Pate, P. K. Ross, T. J. Thamann, C. A. Reed, K. D. Karlin, T. N. Sorrell and E. I. Solomon, *J. Am. Chem. Soc.*, **1989**, 111, 5198.

111. S. S. Tandon, L. K. Thompson, M. E. Manuel and J. N. Bridson, *Inorg. Chem.*, **1994**, 33, 5555.

112. L. K. Thompson, S. S. Tandon and M.E. Manuel, *Inorg. Chem.*, **1995**, 34, 2356.

113. A. Escuer, C. J. Harding, Y. Dussart, J. Nelson, V. McKee and R. Vicente, *J. Chem. Soc., Dalton Trans.*, **1999**, 223.

114. M. Monfort, J. Ribas, X. Solans and M. FontBadia, *Inorg. Chem.*, **1996**, 35, 7633; M. A. S. Goher, A. Escuer, M. A. M. Abu-Youssef, and F. A. Mautner, *Polyhedron*, **1998**, 17, 4265; A. Escuer, R. Vicente, F. A. Mautner, and M. A. S. Goher, *Inorg. Chem.*, **1997**, 36, 1233.

115. E. I. Solomon, In *Metal Clusters in Proteins*, L. Que, Ed., ACS Symposium Series 372, American Chemical Society, Washington, DC, 1988.

116. V. McKee, M. Zvagulis, J. V. Dagdigian, M. G. Patch and C. A. Reed, *J. Am. Chem. Soc.*, **1984**, 106, 4765.

117. N. Kitajima and Y. Moro-oka, *Chem. Rev.*, **1994**, 94, 737.

118. N. Kitajima, *Adv. Inorg. Chem.*, **1992**, 114, 1277.

119. K. D. Karlin, S. Kaderli, and A.D. Zuberbühler, *Acc. Chem. Res.*, **1997**, 30, 139.

120. D. A. Rockcliffe and A. E. Martell, *Inorg. Chem.*, **1993**, 32, 14, 3143.

APPENDIX 1 ATTEMPTED SYNTHESES OF CRYPTANDS FROM CARBON-BRIDGEHEAD TRIPOD AMINE 1,1,1-TRIS(AMINOMETHYL)ETHANE

In order to synthesize a series of dicopper(I) cryptates with unsaturated coordination environments the analogous reaction to those in chapter III have been proposed with carbon-bridgehead tripod amine 1,1,1-tris(aminomethyl)ethane (tame).

1. Preparations

Tame.

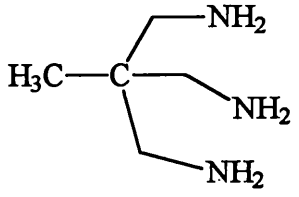

Step1 Preparation of 1,1,1-Tris(benzenesulphonyl oxymethyl)ethane

Benzenesulphonyl chloride (480 ml) was added slowly (3hr) to a solution of 1,1,1-tris(hydroxomethyl)ethane (126 g) in pyridine (550 ml) at 10 °C. After stirring (by means of a mechanical stirrer) for 24 hr at room temperature the resulting mixture was added slowly into a 5 L beaker containing water (1 L), methanol (2 L), and concentrated HCl (800 ml). The granular white precipitate was formed and collected after washing with water and a little methanol. After recrystallization of the crude product from acetone white needle crystals were collected under suction. (Yield: 96%).

Step 2 Preparation of 1,1,1-Tris(azidomethyl)ethane

A mixture of 1,1,1-tris(benzenesulphonyl oxymethyl)ethane, sodium azide, and dried DMSO was maintained at 85 °C under nitrogen for 8 hr. This mixture was poured into

water and extracted with dichloromethane. The extract was washed with water, dried over anhydrous Na_2SO_4, filtered and reduced to minimum volume on a rotary evaporator, giving an almost colorless oil in about 90% yield.

Step3 Preparation of tris-(aminomethyl)ethane

A solution of the triazide in ethanol under nitrogen was heated under gentle reflux. Hydrazine hydrate (193 ml) and 5% Pd/C (2.72g) were added in four equal portions over a period of 2 hr intervals. During addition fizzing occurred. This was violent if too much Pd/C was added at once or if hydrazine hydrate went in too quickly. The resulting mixture was heated at reflux temperature for another 3 hr and then filtered through a celite bed. 1,1,1-Tris(aminomethyl)ethane (tame) was collected after removing the solvent by rotary evaporation. The hydrochloride salt of tame was obtained by adding concentrated HCl to the methanol solution of tame. ^1H NMR (CD_3Cl, ppm): 2.59 (s, 6H), 1.95 (s, 6H), 0.81 (3H). Anal. Cal. For $C_5H_{16}N_3O_{0.5}$ (tame·0.5 H_2O): C, 47.62; H, 12.70; N, 33.33. Found: C, 48.45, H, 12.26, N, 33.17. Cal. For $C_5H_{18}Cl_3N_3$ (tame·3HCl): C, 26.51; H, 8.01; N, 18.55. Found: C, 26.89; H, 8.20; N, 18.18.

Attempted synthesis of free cryptands and cryptates.

Attempts to synthesize free cryptands through 2+3 condensation from tame and a series of dialdehydes used in the syntheses of **L1-L5** failed to give desired products. Instead polymeric products formed in all cases even under the high-dilution condition. When template ions such as Na^+, Ca^{2+}, Sr^{2+}, Ba^{2+}, Cu^+, and Ag^+ were used, insoluble polymeric products precipitated from the solution. Only in one case where the template ion is Na^+ and the dialdehyde is 2,5-diformylfuran, the freshly isolated product was

soluble in acetonitrile and FAB mass spectrum was obtained with two peaks at 931 (100%) and 954 (16%). The possible structures corresponding to these two peaks are shown below.

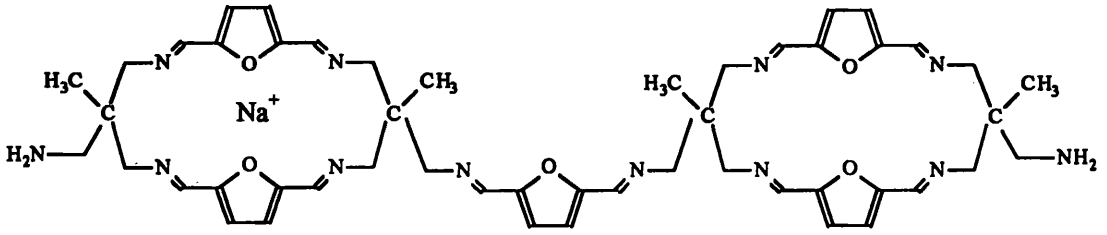

Peak1: $C_{50}N_{12}O_5H_{60}Na$

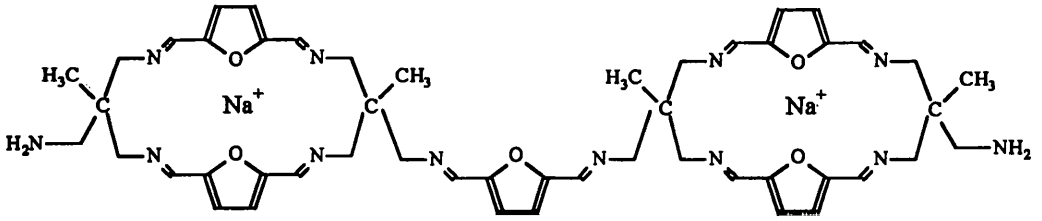

Peak 2: $C_{50}N_{12}O_5H_{60}Na_2$

Formation of dipendant amine macrocycles.

The syntheses of dipendant amine macrocycles through 2 + 2 condensation from tame and dialdehydes gave rise to insoluble polymeric products in most cases in the presence and absence of template ions. When the template ion is Cu^+, the following two dicopper(I) complexes of dipendant amine macrocycles were obtained.

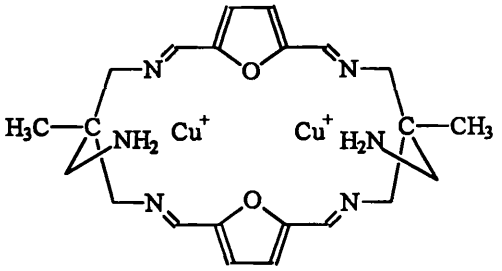

$[Cu_2(\textbf{furtame})][BF_4]_2 \cdot H_2O$

Analysis:	C	H	N
Found:	36.43	5.12	11.16
Cal.	36.22	4.39	11.52

IR: ν_{NH}: 3330, 3287 cm^{-1}; $\nu_{C=N}$: 1636 cm^{-1}. No $\nu_{C=O}$.

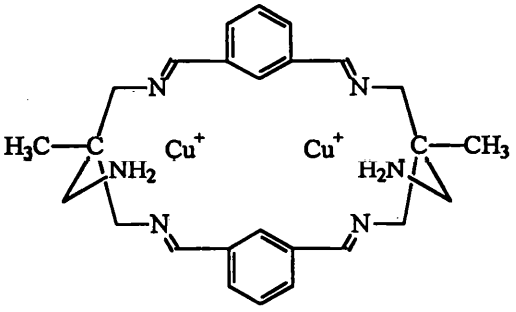

$[Cu_2(\textbf{xyltame})][BF_4]_2 \cdot H_2O$

Analysis:	C	H	N
Found:	41.26	5.05	11.67
Cal.	41.67	4.81	11.22

IR: ν_{NH}: 3331, 3283 cm^{-1}; $\nu_{C=N}$: 1639 cm^{-1}. No $\nu_{C=O}$.

These two dicopper(I) complexes are very sensitive to air oxidation both in the solid state and in solution, preventing the further characterization.

2. Conclusions

From the above results it is known that tame is a not good choice in the syntheses of cryptands with an unsaturated coordination environment for Cu(I). The shorter carbon linkage in tame compared to tren makes the ring closure reaction difficult. Instead, polymeric products are isolated.

APPENDIX 2 INTRODUCTION TO MAGNETOCHEMISTRY

Magnetochemistry is concerned with the study of magnetic susceptibility as applied to chemical problems. Many of these problems lie in the area of molecular structure.

If a material is placed in a magnetic field, the magnetic field in the material will be the sum of the external magnetic field and the magnetic field generated by the material itself. The magnetic field in a material is called magnetic induction and is given the symbol "B":

$$B = H + 4\pi M \qquad (1)$$

where

B = magnetic induction

H = external magnetic field

$\pi = 3.14159$

M = magnetization

The intensity of magnetization in a material may be either slighter smaller, or somewhat larger, than that produced in a vacuum by the same field. In the first case the material is called a diamagnet and is slightly repelled by such a field. In the second case the material is called a paramagnet and is attracted into an applied field.

For mathematical and experimental convenience Eq. (1) is often written as

$$B/H = 1 + 4\pi M/H = 1 + 4\pi\chi_v \qquad (2)$$

where $\chi_v = M/H$ = volume magnetic susceptibility. The volume magnetic susceptibility is so named because B, H, and M are defined per unit volume. It is convenient to use the

magnetic susceptibility instead of the magnetization because the magnetic susceptibility is independent of the external magnetic field, H, for diamagnetic and paramagnetic materials. Many studies have been done using χ_g magnetic susceptibility per gram, which is χ_v divided by the density. Molar magnetic susceptibility can be obtained by multiplying χ_g with the molecular weight.

In general diamagnetic susceptibilities are independent of temperature and of field strength. The paramagnetic susceptibilities are often inversely proportional to the absolute temperature, but independent of field strength which distinguishes them from ferromagnetic materials. In addition, many paramagnetic materials have interactions that cause them to become antiferromagnets or ferromagnets, and their temperature-dependent properties become even more complex.

1. Diamagnetism

Diamagnetism is especially important in the consideration of materials with completely filled electronic shells, that is, systems that do not contain any unpaired electrons. The molar susceptibility of a diamagnetic material is negative, and rather small. Diamagnetism is a property of all matter and arises from the interaction of paired electrons with the magnetic field. Since transition metal substances with unpaired electrons also have a number of filled shells, they too have a diamagnetic contribution to their susceptibility. It is much smaller than the paramagnetic susceptibility, and can usually be separated out by the measurement of the temperature dependence of the susceptibility. Indeed, paramagnetic susceptibilities frequently become so large at low temperature that it is scarcely necessary even to correct for them.

2. Paramagnetism

Paramagnetism is a property exhibited by substances containing unpaired electrons. Paramagnetic susceptibilities are temperature dependent. To a first (high-temperature) approximation, the susceptibility χ varies inversely with temperature, which is the Curie law:

$$\chi = C/T. \qquad (3)$$

Here, χ is the measured molar susceptibility, C is called the Curie constant, and T is the absolute temperature. The plot of the Curie law together with a plot of χ^{-1} *vs.* T for a representative ion is given in Figure A.2.1. Since $\chi^{-1} = C^{-1}T$, a plot of χ^{-1} vs. T is a convenient procedure for the determination of the Curie constant.

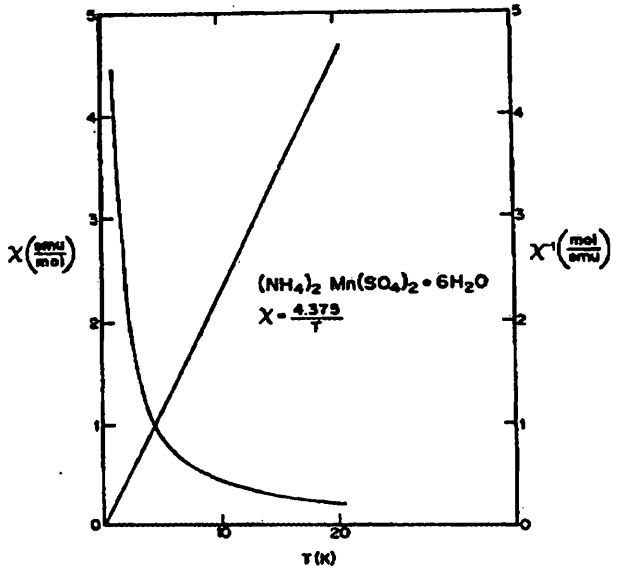

Figure A2.1. Curie and inverse Curie plots for a salt containing manganese(II), for which C = 4.375 emu-K/mol.

Since the magnitude of χ at room temperature is an inconvenient number, it is common among chemist to report the effective magnetic moment, μ_{eff}, which is defined as

$$\mu_{eff} = (3k/N)^{1/2} (\chi T)^{1/2} \qquad (4)$$

$$= [g^2 S(S+1)]^{1/2} \mu_B$$

Here, k is the Boltzman constant, 1.38×10^{-23} JK^{-1}, N is Avogardro's number, 6.02×10^{23} mol^{-1} and $\mu_B = 9.27 \times 10^{-24}$ JT^{-1} is the Bohr magneton.

There are many situations in which the Curie law is not strictly obeyed. One source of the deviation can be the presence of an energy level whose population changes appreciably over the measured temperature interval; another source is the magnetic interaction that can occur between paramagnetic ions. To the simplest approximation, this behavior is expressed by a small modification of the Curie law, to the Curie-Weiss law,

$$\chi = C/(T-\theta), \qquad (5)$$

where the correction term, θ, has the units of temperature. The θ is obtained empirically from a plot of χ^{-1} *vs.* T, as for the Curie law, but now the intercept with the abscissa is not at the origin. When θ is negative it is called antiferromagnetic; when θ is positive, it is called ferromagnetic. The Curie and Curie-Weiss laws are compared for a hypothetical situation in Figure A2.2.

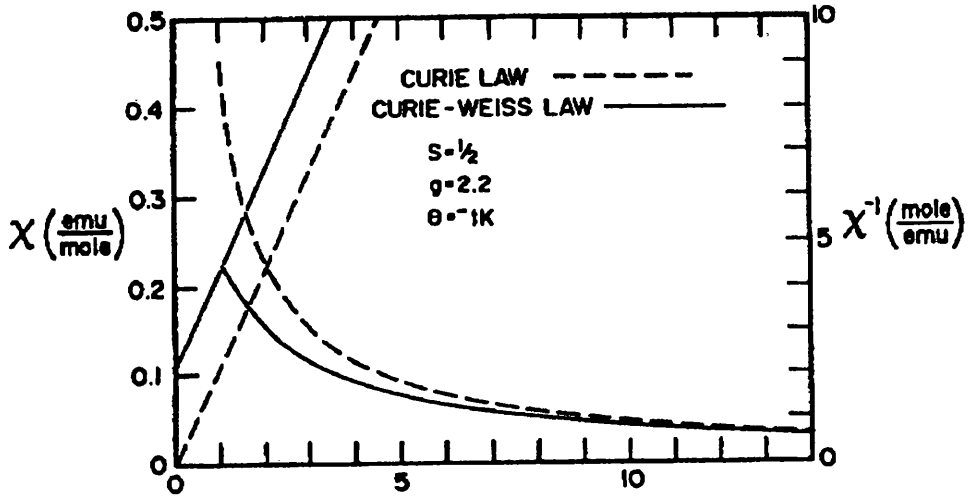

Figure A2.2. The Curie and Curie-Weiss laws. The Curie constant C = 0.454 emu-K/mol (s = ½, g = 2.2) has been used for both curves, while θ = -1 K has been used.

3. Ferromagnetism and antiferromagnetism

The diamagnetism and paramagnetism of materials are characteristic of individual atoms or complexes. In contrast ferromagnetism and antiferromagnetism depend on interactions between electron spins on many atoms and arise from the cooperative behavior of many unit cells in a crystal.

In ferromagnetic substances the spins on different metal centers are coupled into parallel alignment (Figure A2.3a) that is sustained over thousands of atoms in a magnetic domain. The net magnetic moments may be very large because the magnetic moments of individual spins augment each other. Moreover, once established and the temperature maintained below Curie temperature (Tc), the magnetization persists because the spins are locked together. Ferromagnetism is exhibited by materials containing unpaired electrons in *d* or *f* orbitals that couple with unpaired electrons in similar orbitals on

surrounding atoms. The key feature is that this interaction is strong enough to align spins but not strong enough to form covalent bonds, where the electrons are paired.

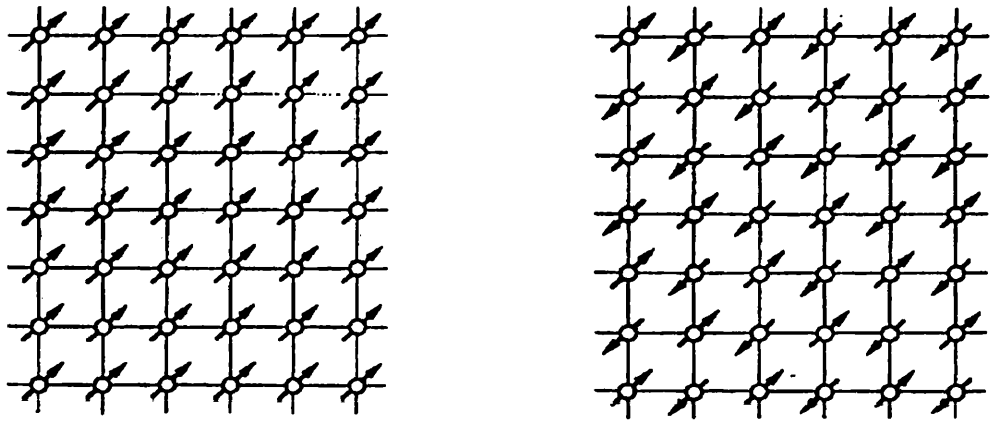

(a) (b)

Figure A2.3. (a) The parallel alignment of individual magnetic moments in a ferromagnetic material and (b) the antiparallel arrangement of spins in an antiferromagnetic material.

A ferromagnetic material, like a paramagnetic material, shows a decrease in magnetic susceptibility with increasing temperature. However, a plot of χ vs. T shows a different line shape for these materials than for paramagnetic material (Figure A2.4a and b). This plot would have a positive curvature for paramagnetic compound and a negative curvature for ferromagnetic compounds. When a critical temperature (Curie temperature) is reached, the curvature of the plot changes and ferromagnetic compounds become paramagnetic.

In an antiferromagnetic substance, neighboring spins are locked into an antiparallel alignment (Figure A2.3b) and the sample has a low magnetic moment.

Antiferromagnetism is often observed when a paramagnetic material is cooled to a low temperature (Figure A2.4c). The critical temperature for the onset of antiferromagnetism is called the Neel temperature (T_N). Above Neel temperature antiferromagnetic materials also become paramagnetic.

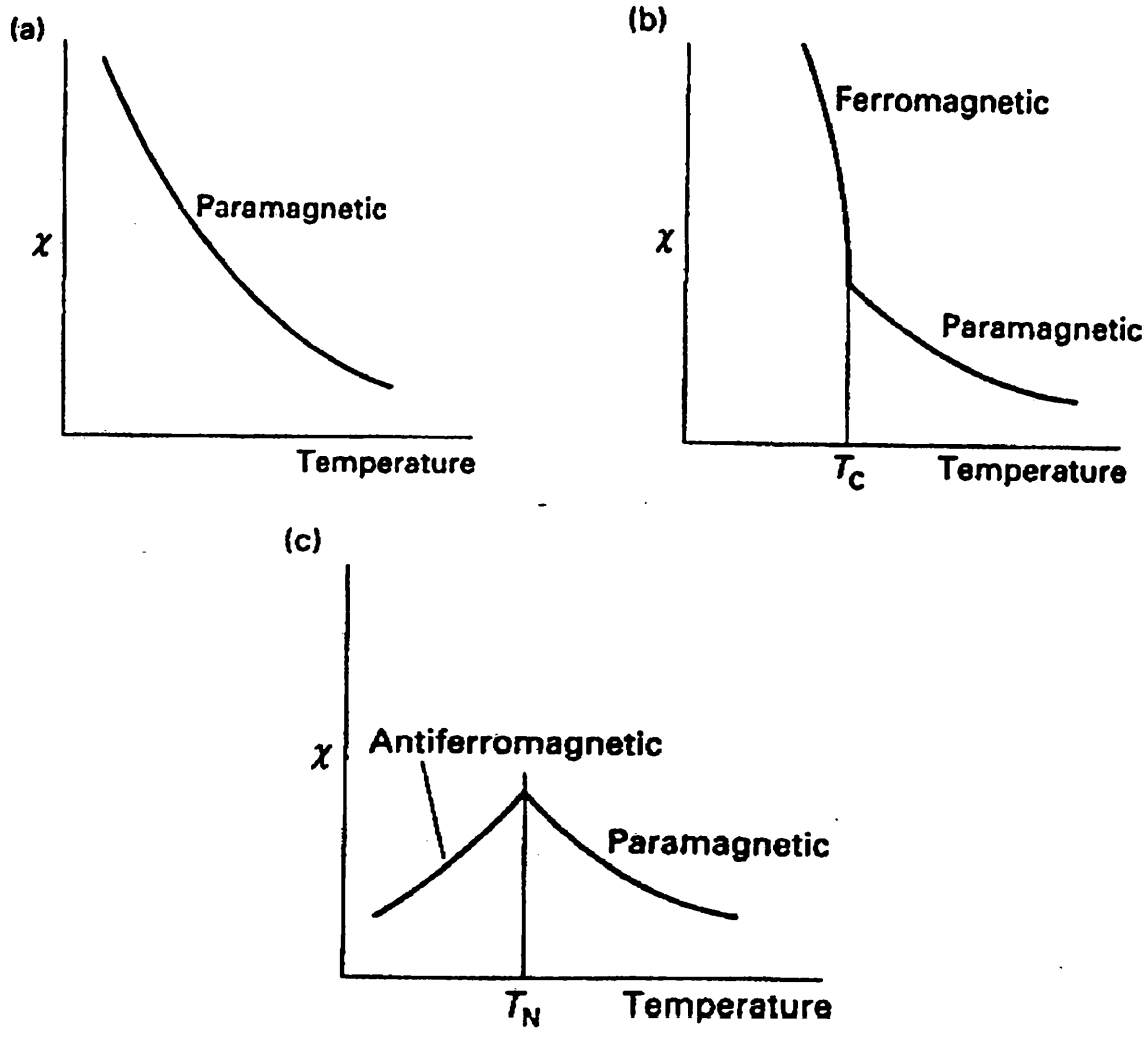

Figure A2.4. Comparison of the temperature dependence of (a) paramagnetic, (b) ferromagnetic, and (c) antiferromagnetic substances.

4. Magnetic exchange in dimers

The Hamiltonian in use for metal-metal exchange interaction in magnetic insulators is of the form

$$H = -2 \Sigma J_{ij} s_i \cdot s_j, \qquad (6)$$

where the sum is taken over all pair-wise interactions of spins i and j in a lattice. In the case of dimeric molecule, the Hamilitonian takes the form

$$H = -2J s_1 \cdot s_2. \qquad (7)$$

This is called an isotropic Hamiltonian and the exchange constant J measures the strength of the interaction. Conventionally the negative J refers to antiferromagnetic (spin-paired or singlet ground state in a dimer) interaction, and positive J refers to ferromagnetic (spin-triplet ground state) interactions. An antiferromagnetic interaction of the type given in Eq. (7), when applied to two ions each of s = ½ gives a spin-singlet ground state and a spin-triplet excited state -2J in energy above the singlet (Figure A2.5) Naturally, if the interaction were ferromagnetic, the diagram would be simply inverted. The isothermal magnetic susceptibility per mol of dimers can be calculated by Bleaney-Bowers equation

$$\chi = \frac{2Ng^2\mu_B{}^2 / 3kT}{1 + (\frac{1}{3})\exp(-2J/kT)} \qquad (8)$$

which is obtained with the application of Van Vleck's equation

$$\chi = \frac{N\sum_n [(E_n{}^{(1)})^2 / kT - 2E_n{}^{(2)}]\exp(-E_n{}^0 / kT)}{\sum_n \exp(-E_n{}^0 / kT)} \qquad (9)$$

to the energy level situation in Figure A2.5.

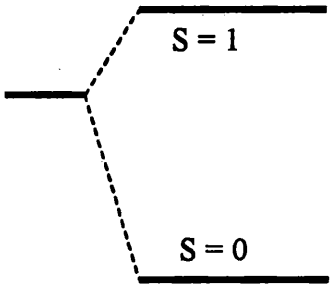

Figure A2.5. Energy-levels for a pair of s = ½ ions undergoing antiferromagnetic exchange. The $S = 1$ level is $-2J$ in energy above the $S = 0$ level.

References

1. R. L. Carlin, *Magneto-Chemistry*, Springer-Verlag Berlin, 1986.

2. P. W. Selwood, *Magnetic Chemistry*, Interscience, New York, 1956.

3. D. F. Shriver, P. W. Atkins, and C. H. Langford, *Inorganic Chemistry*, 2nd Ed.; Oxford University Press, 1998.

4. P. W. Atkins, *Physical Chemistry*, sixth Ed.; Oxford University Press, Oxford, 1998.

APPENDIX 3 INTRODUCTION TO CYCLIC VOLTAMMETRY

Cyclic voltammetry is the most widely used technique for acquiring qualitative information about electrochemical reactions. The power of cyclic voltammetry results from its ability to rapidly provide considerable information on the thermodynamics of redox processes and the kinetics of heterogeneous electron transfer reactions, and on coupled chemical reactions or adsorption processes. Cyclic voltammetry is often the first experiment performed in an electro-analytical study. In particular, it offers a rapid location of redox potentials of the electro-active species, and convenient evaluation of the effect of media upon the redox process.

Cyclic voltammetry consists of scanning linearly the potential of a stationary working electrode (in an unstirred solution), using a triangular potential waveform (Figure A3.1). Depending on the information sought, single or multiple cycles can be used. During the potential sweep, the potentiostat measures the current resulting from the applied potential. The resulting plot of current vs. potential is termed a cyclic voltammogram.

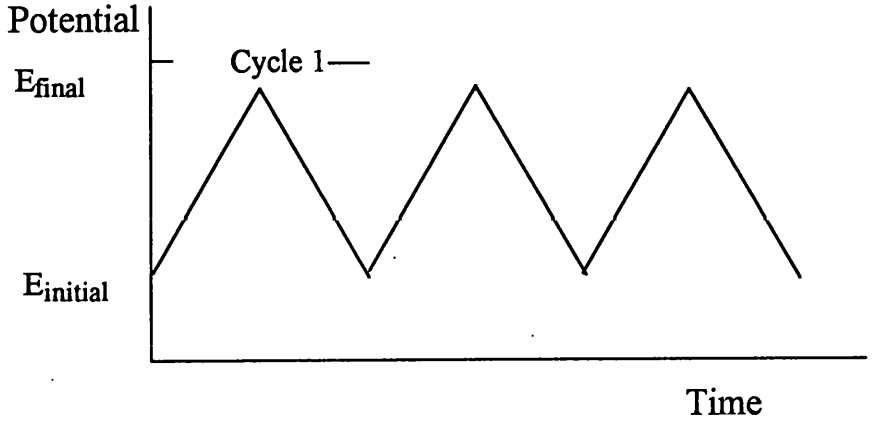

Figure A3.1. Potential-time excitation signal in cycle voltammetric experiment

Figure A3.2 illustrates the expected response of a reversible redox couple during a single potential cycle. It is assumed that only the oxidized form O is present initially. Thus, a negative-going potential scan is chosen for the first half cycle, starting from a value where no reduction occurs. As the applied potential approaches the characteristic E° for the redox process, a cathodic current begins to increase, until a peak is reached. After traversing the potential region in which the reduction process takes place (at least $90/n$ mV beyond the peak), the direction of the potential sweep is reversed. During the reverse scan, R molecules (generated in the forward half cycle and accumulated near the surface) are re-oxidized back to O, and an anodic peak results.

The characteristic peaks in the cycle voltammogram are caused by the formation of the diffusion layer near the electrode surface. These can be best understood by carefully examining the concentration-distance profiles during the potential sweep. For example, Figure A3.3 illustrates four concentration gradients for the reactant and product at different times corresponding to (A) the initial potential value, (B) and (D) the formal potential of the couple during the forward and reversed scans, respectively, and (C) the achievement of a zero reactant surface concentration. Note that the continuous change in the surface concentration is coupled with an expansion of the diffusion layer thickness (as expected in quiescent solutions). The resulting current peaks thus reflect the continuous change on the concentration gradient with time. Hence, the increase of the peak current corresponds to the achievement of diffusion control, while the current drop (beyond the peak) exhibits a $t^{1/2}$ dependence (independent of the applied potential). For the above reasons, the reversal current has the same shape as the forward one.

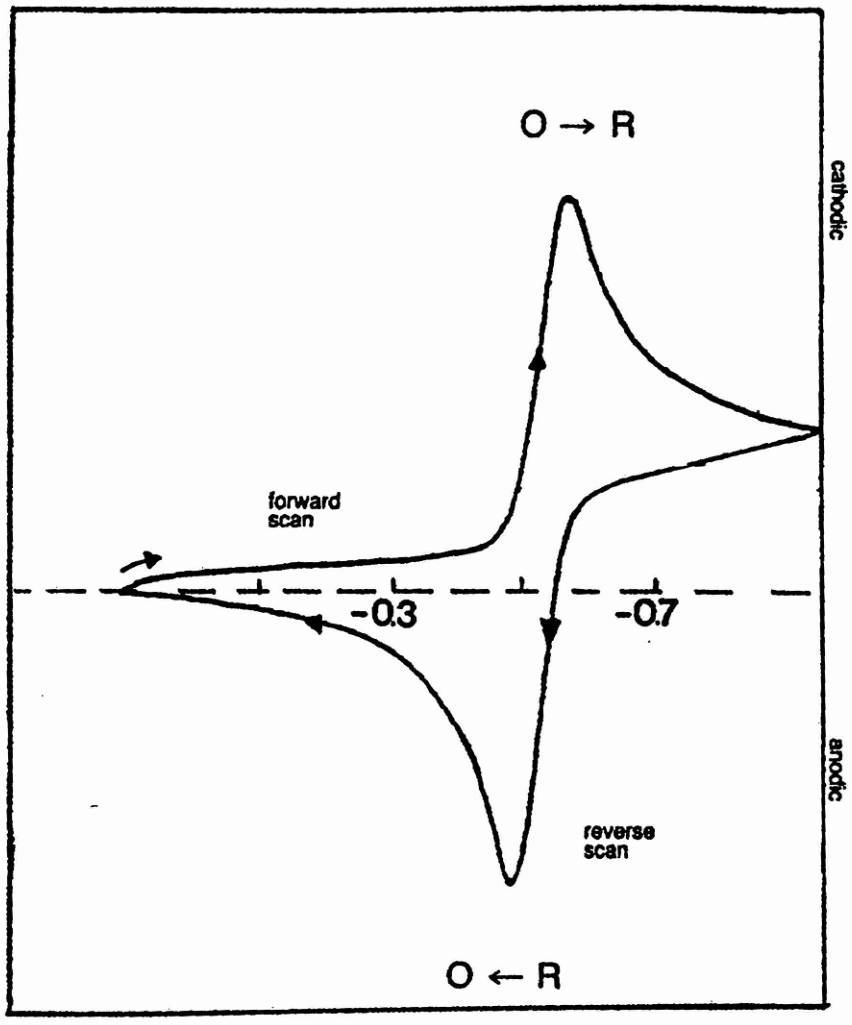

Figure A3.2. Typical cyclic voltammogram for a reversible O + ne^- → R redox process.

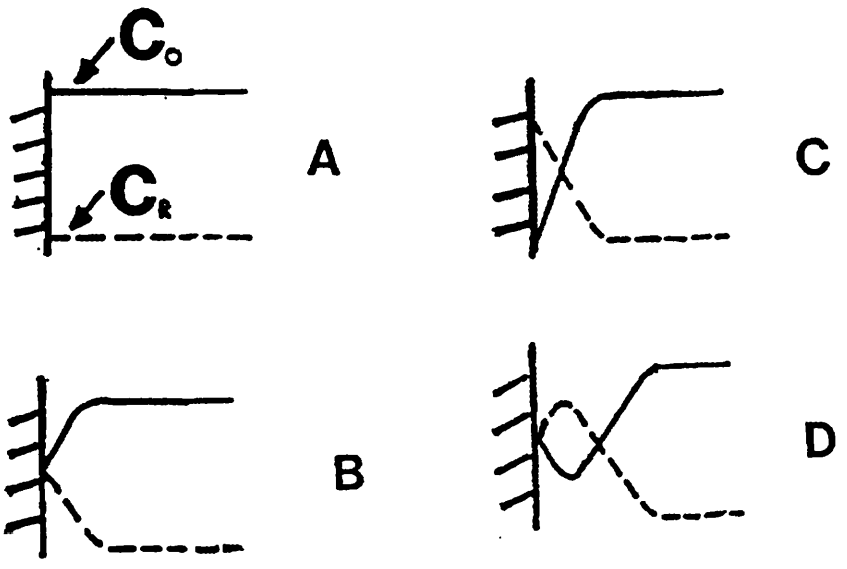

Figure A3.3. Concentration distribution of the oxidized and reduced forms of the redox couple at different times during a cyclic voltammetric experiment corresponding to (A) the initial potential, (B) and (D) the formal potential of the couple during the forward and reversed scans, respectively, and (C) the achievement of a zero reactant surface concentration.

1. Reversible systems

The cyclic voltammogram is characterized by several important parameters. At 25°C, the peak current for reversible couple is given by the Randles-Sevcik equation:

$$i_p = (2.69 \times 10^5) n^{3/2} A C D^{1/2} \nu^{1/2} \qquad (1)$$

where ν is the scan rate, n is the number of electrons transferred, A is the area of electrode, C is the concentration, and D is the diffusion coefficient. Accordingly, the current is directly proportional to the concentration and increases with the square root of

the scan rate. The ratio of the reverse-to-forward peak currents, $i_{p,r}/i_{p,f}$, is unity for a simple reversible couple. This peak ratio can be strongly affected by chemical reactions coupled to the redox process. The current peaks are commonly measured by extrapolating the preceding baseline current.

The position of the peak on the potential axis (E_p) is related to the formal potential of the redox process. The formal potential for a reversible couple is centered between $E_{p,a}$ and $E_{p,c}$:

$$E^\circ = (E_{pa} + E_{pc})/2 \qquad (2)$$

The separation between the peak potentials (for reversible couple) is given by

$$\Delta E_p = E_{p,a} - E_{p,c} = 0.059V/n \qquad (3)$$

Thus, in theory the peak separation can be used to determining the number of electrons transferred, and as a criterion for a Nernstian behavior. Accordingly, a fast one-electron process exhibits a ΔE_p of about 50 mV. Both the cathodic and anodic peak potentials are independent of the scan rate. It is possible to relate the half-peak potential ($E_{p/2}$, where the current is half of the peak current) to the polarographic half-wave potential, $E_{1/2}$:

$$E_{p/2} = E_{1/2} \pm 0.028V/n \qquad (4)$$

(The sign is positive for a reduction process.)

For multi-electron-transfer reversible processes, the cyclic voltammogram consists of several distinct peaks, depending upon the separation of the potentials of the individual steps.

The situation is very different when the redox reaction is slow or coupled with a chemical reaction. Indeed, it is these "non-ideal" processes that are often of great

chemical interest and for which the diagnostic power of cyclic voltammetry is most useful.

2. Irreversible and quasi-reversible systems

For irreversible processes (those with sluggish electron exchange), the individual peaks are reduced in size and widely separated (Figure A3.4, curve A). Totally irreversible systems are characterized by a shift of the peak potential with the scan rate:

$$E_p = E^0 - \frac{RT}{\alpha n_a F}[0.78 - \ln\frac{k^0}{D^{1/2}} + \ln(\frac{\alpha n_a F v}{RT})^{1/2}] \qquad (5)$$

where α is the transfer coefficient and n_a is the number of electrons involved in the charge-transfer step. Thus, E_p occurs at potentials higher than E^0, with the over-potential related to k^0 and α. Independent of the value k^0, such peak displacement can be

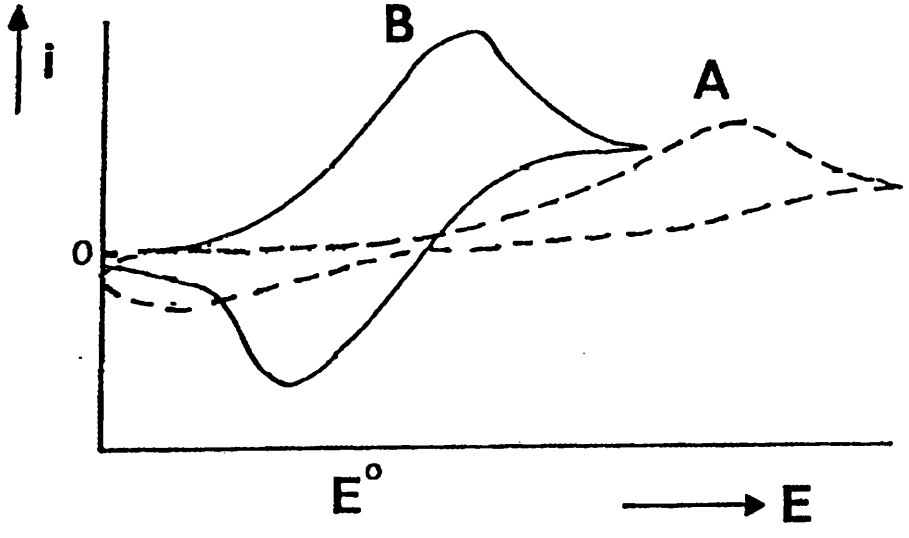

Figure A3.4 Cyclic volatmmograms for (A) irreversible and (B) quasi-reversible redox processes.

compensated by an appropriate change of the scan rate. The peak potential and the half-peak potential (at 25 °C) will differ by $48/\alpha n$ mV. Hence, the voltammogram become more drawn out as αn decreases.

The peak current, given by

$$I_p - (2.99 \times 10^5) n(\alpha n_a)^{1/2} A C D^{1/2} v^{1/2} \qquad (6)$$

is still proportional to the bulk concentration, but will be lower in height. Assuming an α value of 0.5, the ratio of the reversible-to-irreversible current peaks is 1.27 (i.e., the peak current for the irreversible process is about 80% of the peak for a reversible one).

For quasi-reversible systems (with $10^{-1} > k^0 > 10^{-5}$ cm/s), the current is controlled by both the charge transfer and mass transport. The shape of the cyclic voltammogram is a function of $k^0 / (\pi a D)^{1/2}$ (where $a = nFv/RT$). As $k^0 / (\pi a D)^{1/2}$ increases, the process approaches the reversible case. For small values of $k^o / (\pi a D)^{1/2}$ (i.e., at very fast v), the system exhibits an irreversible behavior. Overall, the voltammograms of a quasi-reversible system are more drawn out and exhibit a larger separation in peak potentials compared to a reversible system (Figure 4, curve B).

3. Study of reaction mechanisms

One of the most important applications of cyclic voltammetry is for qualitative diagnosis of chemical reactions that precede or succeed the redox process. Such electrochemical reaction mechanisms are commonly classified by using the letters E and C (for the redox and chemical steps, respectively) in the order of the steps in the reaction scheme. The occurrence of such chemical reactions that directly affect the available surface concentration of the electro-active species is common to redox processes of many important organic and inorganic compounds. Changes in the shape of the cyclic

voltammogram, resulting from the chemical competition for the electrochemical reactant or product, can be extremely useful for elucidating these reaction pathways and for providing reliable chemical information about reactive intermediates.

For example, when the redox system is perturbed by a following chemical reaction, i.e., an EC mechanism,

$$O + ne^- \rightleftharpoons R \longrightarrow Z \qquad (7)$$

the cyclic voltammogram will exhibit a smaller reverse peak (because the product R is chemical removed from the surface). The peak ratio $i_{p,r}/i_{p,f}$ will thus be smaller than unity; the exact value of the peak ratio can be used to estimate the rate constant of the chemical step. In the extreme case, the chemical reaction may be so fast that all of R will be converted to Z, and no reverse peak will be observed.

Additional information on the rates of these (and other) coupled chemical reactions can be achieved by changing the scan rate (i.e., adjusting the experimental time-scale). In particular, the scan rate controls the time spent between the switching potential and the peak potential (during which the chemical reaction occurs).

Other reaction mechanisms can be elucidated in a similar fashion. For example, for a CE mechanism, where a slow chemical reaction precedes the electron transfer, the ration of $i_{p,r}/i_{p,f}$ is generally larger than one, and approaches unity as the scan rate decreases. The reverse peak is usually not affected by the coupled reaction, while the forward one is no longer proportional to the square root of the scan rate.

ECE processes, with a chemical step being interposed between electron transfer steps

$$O_1 + ne^- \rightleftharpoons R_1 \longrightarrow O_2 + ne^- \longrightarrow R_2 \qquad (8)$$

are also easily exploited by cyclic voltammetry, because the two redox couples can be observed separately. The rate constant of the chemical step can thus be estimated from the relative sizes of the two cyclic voltammetry peaks.

References

1. J. Wang, *Analytical Electrochemistry*, VCH, Weiheim, 1994.

2. P. H. Rieger, *Electrochemistry*, 2nd ed., Chapman & Hall, London,1993.

APPENDIX 4 INTRODUCTION TO UV-VIS SPECTROSCOPY

Absorption of ultraviolet and visible light by a molecule may cause an electronic transition from a lower energy orbit to a higher one. UV-VIS spectra resulting from electronic transitions between two states of the molecule carry information about these states. One of their important special features relevant to coordination compounds (as well as to some other molecular systems) is the strong dependence of the electronic energies on the inter-atomic distances. Owing to this fact, the stationary states of the system are not purely electronic but electron-vibrational.

1. The Franck-Condon principle

According to the Franck-Condon Principle, an electronic transition in a molecule takes place so much more rapidly than a vibrational transition that, in a vibronic transition, the nuclei have very nearly the same position and velocity before and after the transition. Before the absorption, the molecule is in the lowest vibrational state of its lowest electronic state (Figure A4.1); the most probable location of the nuclei is at their equilibrium separation, *Re*. The electronic transition is most likely to take place when the nuclei have this separation. When the transition occurs, the molecule is excited to the state represented by the upper curve. According to the Franck-Condon principle, the nucleus framework remains constant during this excitation, so we imagine the transition as lying along the vertical line in Figure A4.1. Thus the transition is called vertical transition indicating an electron transition that occurs without change of the nuclear geometry.

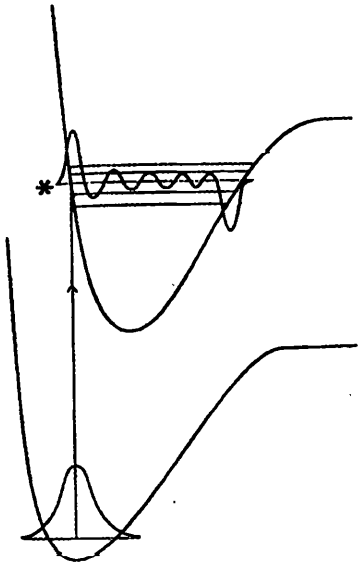

Figure A4.1. In the quantum mechanical version of the Franck-Condon principle, the molecule undergoes a transition to the upper vibrational state that most closely resembles the vibrational wavefunction of the vibrational ground state of the lower electronic state.

The vertical transition cuts through several vibrational levels of the upper electronic state. The level marked * is the one in which the nuclei are most probably at the same initial separation Re (because the vibrational wave function has maximum amplitude there), so this vibrational state is the most probable state for the termination of the transition. However, it is not the only accessible vibrational state because several nearby states have an appreciable probability of the nuclei being at the separation R_e. Therefore, transitions occur to all the vibrational states in this region, but most intensely to the state with a vibrational wavefunction that peaks most strongly near R_e.

The vibrational structure of the spectrum depends on the relative horizontal position of the two potential energy curves, and a lot of vibrational structure is

stimulated if the upper potential curve is appreciably displaced horizontally from the lower. The upper curve is usually displaced to greater equilibrium bond lengths because electronically excited states usually have more anti-bonding character than electronic ground states.

The separation of the vibrational fine structure in an electronic absorption spectrum depends on the vibrational quantum of the upper electronic state. Hence, electronic absorption spectra may be used to assess the force fields and dissociation energies of electronically excited molecules.

2. Franck-Condon factors

The quantitative form of the Franck-Condon principle is derived from the expression for the transition dipole moment, $\mu_{f,i}$, between the initial and final states, where $\mu_{fi} = \langle f | \mu | i \rangle$, and μ is the electronic dipole moment operator. The dipole moment operator is a sum over all nuclei and electrons in the molecule:

$$\mu = -e\sum_i \mathbf{r}_i + e\sum_I Z_I \mathbf{R}_I \qquad (1)$$

where the vectors are the distances from the center of charge of the molecule. The intensity of the transition is proportional to the square modulus, $|\mu_{fi}|^2$, of the magnitude of the transition dipole moment.

The overall state of the molecule consists of an electronic part, $|\varepsilon\rangle$, and a vibrational part, $|v\rangle$. Therefore, within the Born-Oppenheimer approximation, the transition dipole moment factorizes as follows:

$$\mu_{fi} = \left\langle \varepsilon_f \nu_f \left| \left\{ -e\sum_i \mathbf{r}_i + e\sum_I Z_I \mathbf{R}_I \right\} \right| \varepsilon_i \nu_i \right\rangle$$
$$= -e\sum_i \left\langle \varepsilon_f \left| \mathbf{r}_i \right| \varepsilon_i \right\rangle \left\langle \nu_f \middle| \nu_i \right\rangle + e\sum_I Z_I \left\langle \varepsilon_f \middle| \varepsilon_i \right\rangle \left\langle \nu_f \left| \mathbf{R}_I \right| \nu_i \right\rangle$$

The second term on the right of the last row is zero, because $\langle \varepsilon_f | \varepsilon_i \rangle = 0$ for two different electronic states (they are orthogonal). Therefore,

$$\mu_{fi} = -e\sum_i \left\langle \varepsilon_f \left| \mathbf{r}_i \right| \varepsilon_i \right\rangle \left\langle \nu_f \middle| \nu_i \right\rangle = \mu_{\varepsilon_f, \varepsilon_i} S(\nu_f, \nu_i) \qquad (2)$$

where

$$\mu_{\varepsilon_f, \varepsilon_i} = -e\sum_i \left\langle \varepsilon_f \left| \mathbf{r}_i \right| \varepsilon_i \right\rangle, \qquad S(\nu_f, \nu_i) = \left\langle \nu_f \middle| \nu_i \right\rangle \qquad (3)$$

The matrix element $\mu_{\varepsilon f, \varepsilon i}$ is the transition dipole moment arising from the redistribution of electrons. The factor S (ν_f, ν_i) is the overlap integral between the vibrational state $|\nu_i\rangle$ in the initial electronic state of the molecule, and the vibrational state $|\nu_i\rangle$ in the final electronic state of the molecule.

Because the transition intensity is proportional to the square of the magnitude of the transition dipole moment, the intensity of absorption is proportional to $|S(\nu_f, \nu_i|^2$, which is known as the **Frank-Condon factor** for the transition. It follows that, the greater overlap of the vibrational state wavefunction in the upper electronic state with the vibrational wavefunction in the lower electronic state, the greater the absorption intensity of that particular simultaneous electronic and vibrational transition.

3. Specific types of transitions

The absorption of a photon can often be traced to the excitation of specific types of electrons or to electrons that belong to a small group of atoms. For example, when a carbonyl group (>C=O) is present, an absorption at about 290 nm is normally observed,

although its precise location depends on the nature of the rest of the molecule. Groups with characteristic optical absorption are called chromophores and their presence often accounts for the colors of substances.

(a) d-d transitions

All five *d* orbitals of a given shell are degenerate in a free atom. In a complex, where the immediate environment of the atom is no longer spherical, the *d* orbitals are not all degenerate, and electrons can absorb energy by making transition between them. In an octahedral complex, such as $[Ti(OH_2)_6]^{3+}$, the five *d* orbitals of the central atoms are split into two sets (Figure A4.2a), a triply degenerate set labeled t_{2g} and a doubly degenerate set labeled e_g. The three t_{2g} orbitals lie below the two e_g orbitals; the difference in energy is denoted Δ_O and called the ligand-field splitting parameter (the O denoting octahedral symmetry). The *d* orbitals also divide into two sets in a tetrahedral complex (Figure A4.2b). In this case, however, the *e* orbitals lie below the t_2 orbitals and their separation is written Δ_T. Neither separation is large, so transitions between the two sets orbitals typically occur in the visible region of the spectrum even though they are electronic. The transitions are responsible for many of the colors that are so characteristic of transition metal complexes.

There are two selection rules governing the intensities of d-d transition bands: spin selection rules (spin-allowed transitions: $\Delta S = 0$) and the Laporte selection rules (symmetry-allowed transitions for centrosymmetric complexes $g \leftrightarrow u$). The coupling of spin and orbital angular momenta can relax the spin selection rule, but such spin forbidden $\Delta S \neq 0$ transitions are generally much weaker than spin-allowed transitions. The Laporte selection rule may be relaxed in two ways. Firstly, a complex may be

departing slightly from perfect centrosymmetry. Secondly, the complex might undergo an asymmetric vibration.

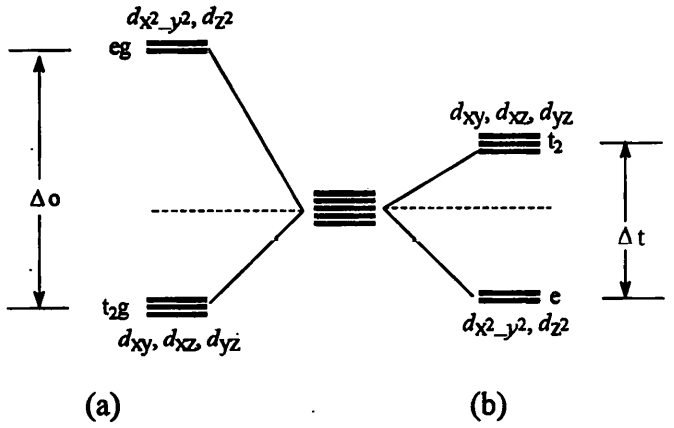

Figure A4.2 Energy-level diagrams showing the splitting of a set of *d* orbitals (degenerate in the uncoordinated ion at the center of the diagram) by octahedral and tetrahedral crystal fields. (a) The splitting caused by octahedral coordination of six ligands, (b) The splitting caused by tetrahedral coordination of four ligands.

(b) Charge –transfer transitions

A complex may absorb radiation as a result of the transfer of an electron from the ligands to the *d* orbitals of the central atom, or vice versa. In such charge-transfer transitions the electron moves through a considerable distance, which means that the transition dipole moment may be large and the absorption is correspondingly intense. This mode of chromophore activity is shown in many oxoanions such as the permanganate, MnO^{4-}, where it accounts for the intense violet color (which arises from

strong absorption within the range 420-700 nm). In this oxoanion, the electron migrates from an orbital that is largely confined to the O atom of the ligand to an orbital that is largely confined to the Mn atom. It is therefore an example of a ligand-to metal charge-transfer transition (LMCT). The reverse migration, a metal-to-ligand charge-transfer transition (MLCT), can also occur. An example is the transfer of a *d* electron into the antibonding π orbitals of an aromatic ligand.

(c) $\pi^* \leftarrow \pi$ and $\pi^* \leftarrow n$ transitions

Absorption by a C=C double bond excites an π electron into an antibonding π^* orbital. The chromophore activity is therefore due to a $\pi^* \leftarrow \pi$ transition. Its energy is about 7 eV for an unconjugated double bond, which corresponds to absorption at 180 nm (in the ultraviolet). When the double bond is part of a conjugated chain, the energy of the molecular orbitals lies closer together and the $\pi^* \leftarrow \pi$ transition moves to longer wavelength: it may even lie in the visible region if the conjugated system is long enough.

The transition responsible for absorption in the >C=N- chromophore can be traced to the lone pairs of electrons on the N atom. The Lewis concept of a 'lone pair' of electrons is represented in molecular orbital theory by a pair of electrons in an orbital confined largely to one atom and not appreciably involved in bond formation. One of these electrons may be excited into an empty π^* orbital of the >C=N- chromophore, which gives rise to a $\pi^* \leftarrow n$ transition.

References

1. I. B. Bersuker, *Electronic Structure and Properties of Transition Metal Compounds*, Wiley, New York, 1996.

2. P. W. Atkins, *Physical Chemistry*, 6th ed., Oxford University Press, Oxford, 1998.

APPENDIX 5 INTRODUCTION TO NMR SEPCTROSCOPY

Nuclear magnetic resonance (NMR) is the most powerful and widely used spectroscopic method for the determination of molecular structures in the solution, pure liquids, and gases. In many cases, it provides information about shape and symmetry with greater certainty than is possible with other spectroscopic techniques. NMR also provides information about the rate and nature of the interchange of ligands in fluxional molecules.

NMR can be observed only for compounds containing elements with magnetic nuclei (those with non-zero nuclear spin). The sensitivity is dependent on several parameters, including the abundance of the isotope and the size of its nuclear magnetic moment. With modern multinuclear NMR techniques it is easy to observe spectra for approximately 20 different nuclei, including many elements that are important in inorganic chemistry, such as ^{1}H, ^{7}Li, ^{11}B, ^{13}C, ^{15}N, ^{19}F, ^{23}Na, ^{27}Al, ^{29}Si, ^{31}P, ^{195}Pt, and ^{199}Hg.

1. Measurement

A nucleus with spin I can takes up $2I + 1$ distinct orientations relative to the direction of an applied magnetic field. Each orientation has a different energy, with the lowest level (marginally) the most populated. The energy of the transition between these nuclear spin states is measured by exciting nuclei in the sample with a radio-frequency pulse or pulses sequence and then observing the return of the nuclear magnetization back to equilibrium. After data processing (Fourier transformation), the data are displayed as an absorption spectrum, with peaks at frequencies corresponding to transitions between the different energy levels.

2. Chemical shifts

The frequency of a NMR transition depends on the local magnetic field, B_{loc}, the nucleus experiences. This local field is the sum of the field of the magnet, B_{appl}, and an additional local field arising from the effect of the applied field on the molecule, which is written as $-\sigma B_{appl}$:

$$B_{loc} = (1-\sigma)B_{appl}.$$

The constant σ, which expresses the role of the local chemical environment, is called the shielding constant. In practice, the position of a NMR signal is expressed as the chemical shift δ. This is defined in terms of the difference between the resonance frequency of nuclei in the sample and that of a reference compound:

$$\delta = \frac{\nu_{sample} - \nu_{ref}}{\nu_{ref}} \times 10^6.$$

A common standard for ^1H, ^{13}C, or ^{29}Si NMR spectra is tetramethylsilane, $Si(CH_3)_4$(TMS).

When δ for a signal is negative, the nucleus involved is said to be shielded relative to the standard. Conversely, a positive δ corresponds to nucleus that is de-shielded with respect to the reference. The chemical shift for a particular nucleus in a given compound always has the same value, whatever spectrometer frequency is used.

3. Spin-spin coupling

In addition to being sensitive to the surrounding electron density, the nuclear resonance is also affected by the presence of neighboring magnetic nuclei. Each such nucleus acts as an additional magnet whose effect is added to that of the spectrometer magnet. For a neighbor nucleus of spin I, each of the $2I+1$ orientations corresponds to a

different field increment, so that the nucleus probed is equally likely to experience any one of $2I+1$ different magnetic fields, giving a set of signals of slightly different frequencies. Thus, a nucleus close to one other nucleus of spin I will give a signal consisting of $2I+1$ equally intense components. For example, the methyl protons of an H_3C-CH group will give a doublet signal because of the single ^1H nucleus adjacent. Similarly, the ^{13}C signal of $CDCl_3$ is a 1:1:1 triplet (^2D, $I = 1$). The spacing between the components of these signals is referred to as the spin-spin coupling constant, since it represents the energy of the magnetic coupling between the two nuclei. The magnitude of the coupling constant depends on the identity of the two nuclei and on the nature of the bonds connecting them, hence, on the stereochemistry.

Similar arguments show that a set of n equivalent adjacent nuclei with $I = ½$ will result in a splitting of the signal into $2n + 1$ components, equally spaced by an amount equal to the coupling constant. The intensities are in the ratios of the binomial coefficients, but are perhaps more easily derived by the J-tree technique, in which the effects of each individual nucleus are considered consecutively. Thus, a single spin = 1/2 nucleus produces a 1:1 doublet with a separation of J (Figure A5.1a). A second such nucleus will split each of the doublet lines into two, again separated by J, so that the two central lines superpose, giving a 1:2:1 triplet. The process is continued until all the coupling nuclei have been included (Figure A5.1b). Note that equivalent nuclei appear not to couple with each other.

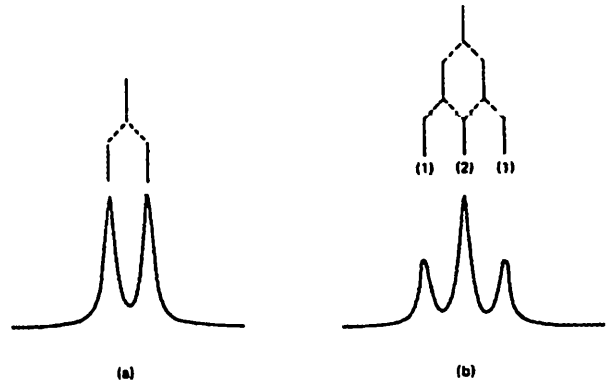

Figure A5.1 Characteristic coupling patterns due to (a) one, (b) two equivalent I = ½ nuclei. The numbers in brackets are the relative intensities.

It often happens that the coupling nuclei are not all equivalent. Nevertheless, it is still possible to use the same procedure, provide that the appropriate coupling constants are used. Thus, for coupling to two non-equivalent nuclei (each with $I = ½$), two different J-values are involved and a 1:1:1:1 four lines spectrum is expected (Figure A5.2). Note that the same result is obtained regardless of the order in which the couplings are considered.

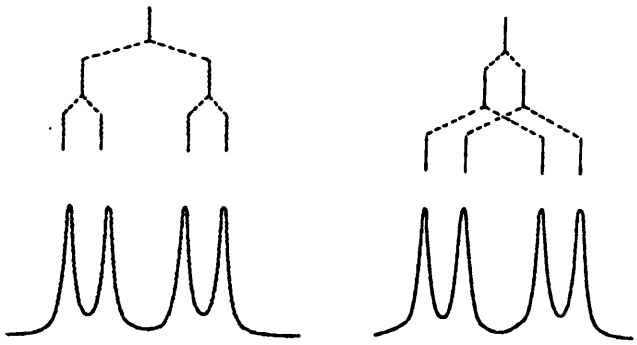

Figure A5.2 Coupling to two non-equivalent $I = 1/2$ nuclei. Note that the same pattern is obtained whether the larger of the smaller coupling is considered first.

References

1.R. V. Parish, *NMR, NQR, EPR, and MÖSSBAUER Spectroscopy in Inorganic Chemistry*, Horwood, Chichester, 1990.

2. D. F. Shriver, P. W. Atkins, and C. H. Langford, *Inorganic Chemistry*, 2nd ed., Oxford University Press, Oxford, 1998.

APPENDIX 6 INTRODUCTION TO EPR SPECTROSCOPY

Electron paramagnetic resonance is the study of molecules and ions containing unpaired electrons by observing the magnetic fields at which they come into resonance with monochromatic radiation. It is electrons which are of interest rather than nuclei. The system examined must be paramagnetic; i.e. it is unpaired electrons which are important. EPR thus applies to compounds of the various transition series and to free radicals. It is a useful complement to NMR which cannot normally be used for paramagnetic samples. Unpaired electrons occur in the valence shell, e.g. the *d*-orbitals of transition metal ions, or in the uppermost molecular orbitals of paramagnetic molecules (radicals). In either case, there is a series of excited electronic states with energies spread over large ranges, 5000-40000 cm^{-1}. Transitions between these levels are the province of UV or visible spectroscopy. However, if a magnetic field is applied, the ground electronic state can split into a set of closely spaced levels. The spacing depends on the strength of the applied field, but quite modest field lead to transition energies of a few GHz.

There is a considerable parallel between EPR and NMR. Both depend on the magnetic moment associated with spinning particles, either an electron or a nucleus. For a spin of 1/2, the two states produced by interaction with a magnetic field, B, differ in energy by

$$\Delta E = g\mu B$$

where the value of g depends on the identity of the particle, and μ is its magnetic moment. For a free electron, g is 2.0023, while for a proton it is 5.5856. The basic magnetic moment of nuclei and electrons differ considerably because of the dependence on mass, which enters as a reciprocal

$$\mu = eh/4\pi m$$

so that μ_B for the electron (the Bohr magneton) is 9.274×10^{-24} J T^{-1}, while μ_N for the proton (the nuclear magneton) is 5.051×10^{-27} J T^{-1}. It is these factors that are primarily responsible for the difference in characteristic of the two magnetic resonance methods.

EPR spectra depends on determining the *g*-values for the unpaired electrons in the sample, which differ from those free electrons and are sensitive to the chemical environment of the paramagnetic atom. This is normally done by using a fixed frequency, usually 9 GHz, and varying the applied field. Some spectrometers operate at about 36 GHz, but they are experimentally more difficult to use.

1. *g*-value

For a free electron in a vacuum, $g = 2.0023$. In a chemical system, the unpaired electron occupies an orbital, which may be more or less localized on a single atom or may be heavily delocalized across a molecule or radical. The *g*-value now reflects the nature of this orbital. In the free radical case, *g* remains close to the free electron value. In other cases there may be a considerable contribution to the magnetic moment of electron from its orbital motion. The value of *g* may then be quite different from 2.0; it seldom falls much below this figure, but may reach 9.0 or more. Orbital contribution arises most commonly in systems containing transition metal ions. In addition there is an indirect effect which renders the *g*-value different from 2.0, even in the absence of a direct orbital contribution. When a substance containing unpaired electrons is placed in a magnetic field, the motion of the unpaired electrons is affected so that the magnetic moment so induced opposed the applied field (this is the origin of magnetic susceptibility). The simplest way to describe this effect is in terms of the system gaining

some of the characteristics of the excited state. It usually happens that the excited states have an orbital momentum and, to the extent that they got 'mixed in' to the ground state description via spin-obit coupling, so the magnetic moment and g depart from the spin-only value. The extent of this mixing is inversely related to the energy of the excited state.

2. Fine structure

A species with spin S has total $2S+1$ energy states characterized by the quantum numbers M_S. In the absence of a magnetic field states with $M_S \neq 0$ are expected to remain doubly degenerate. However, these doublets are usually separated from each other by the electric field produced by the other atoms, which acts *via* spin-orbital coupling, etc. The application of a magnetic field removes the remaining degeneracy and transitions may be observed between adjacent states, following the selection rule $\Delta M_S = \pm 1$. In principle, then, $2S$ transitions can occur, their separations representing the extent of zero-field splitting (Figure A6.1). The appearance of more than one line (when $S > ½$) is known as fine structure of the spectrum. Whether or not all or any of the transitions can be observed, and what their g-values are, depends on the electron configuration and the zero-field splitting and, of course, on the magnetic field range of the spectrometer.

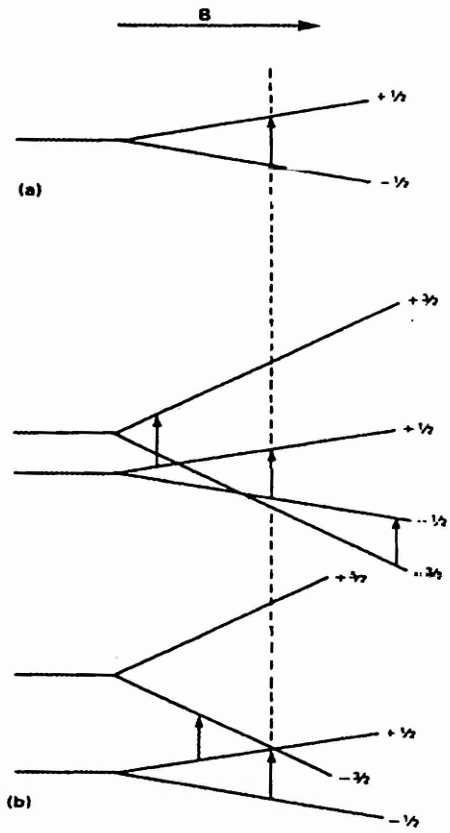

Figure A6.1 Energy level diagrams: (a) S =1/2; (b) S =3/2 for two different zero-field splittings.

3. Anisotropy

Many systems do not have cubic symmetry and g-values depend on the direction between the magnetic field and the principal (z) axis of the systems. It often happens that the symmetry of the system is axial, i.e. the x- and y-direction are equivalent but different from z. Many copper (II) complexes have tetragonal symmetry and then there are two principal g-values associate with them; $g_{//}$ and $g_{\perp}$. When the field and molecule axis are parallel, it appears at $g_{//}$; when they are perpendicular, it appears at $g_{\perp}$. If the sample is a single crystal in which all the molecules are oriented similarly with their axes at an angle θ to the magnetic field, the observed g-value is given by

$$g^2 = g_{//}^2 \cos^2\theta + g_{\perp}^2 \sin^2\theta.$$

If the symmetry is even lower, three principal g-values are needed and the observed g-value for an arbitrary orientation is

$$g^2 = g_x^2 \cos^2\theta_x + g_y^2 \cos^2\theta_y + g_z^2 \cos^2\theta_z$$

where the angles are those between the field and the molecular axes.

In a solution, the molecules are continuously tumbling, usually at rates considerably greater than the frequency of spectrometer. Any anisotropy is then averaged to zero during the time required to excite the system.

When the solution is frozen, or if the sample is a powdered solid, all possible orientations still occur randomly, but the molecular positions are fixed. Each molecule with a particular orientation has its own g-value and the observed spectrum is the sum over all the molecules. On a purely statistical basis, there will be very few molecules with principal axes parallel to the field, and far more perpendicular. This fact combines with angle-dependence of intensity to give the distribution of intensities shown in Figure A6.2. In the derivative spectrum it is usually possible to recognize the two principal g-values, though the resolution depends critically on the difference between $g_{//}$ and $g_{\perp}$. For many rhombic systems ($x \neq y \neq z$), the difference between g_x and g_y is not great and the spectrum appears to have an asymmetry in '$g_{\perp}$' line. If the three principal g-values are appreciably different, three major lines appear in the spectrum.

4. Hyperfine structure

An EPR spectrum may show additional fine structure when the atom on which the unpaired spin is centered has a nuclear spin. In a manner exactly analogous to that in NMR spectroscopy, a nucleus of spin I gives rise to a splitting of the EPR line into $2I$

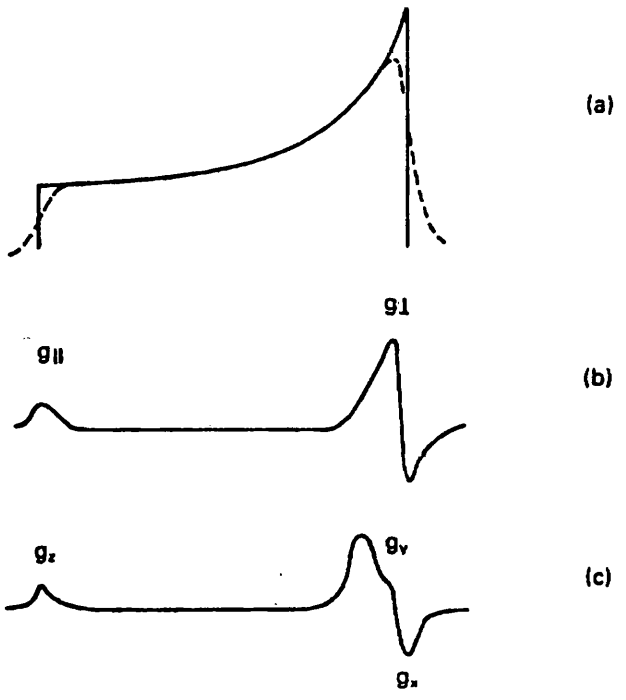

Figure A6.2 Typical shapes of EPR spectra for powders or frozen solutions containing anisotropic species with $g_{//} > g_{\perp}$. (a) and (b) are for an axial system (tetragonal) in the absorptive and first-derivative form, (c) is the first-derivative form for a rhombic system.

+1 components, all of equal intensity separated by the coupling constant, A. That is, in the presence of the magnetic field, the nucleus can adopt any one of the $2I+1$ orientations, each of which produces a different local magnetic field at the electron. Each energy level is thus split into $2I+1$ components for any given value of the applied field, and the energy depends on the product of M_s and m_I, resulting in $2I+1$ lines in the spectrum (Figure A6.3). This is known as hyperfine structure. In some cases, the unpaired electrons are delocalized over several identical atoms, e.g. in polynuclear metal

complexes or organic radicals. The splitting is then into $2nI + 1$ lines (n = the number of equivalent nuclei).

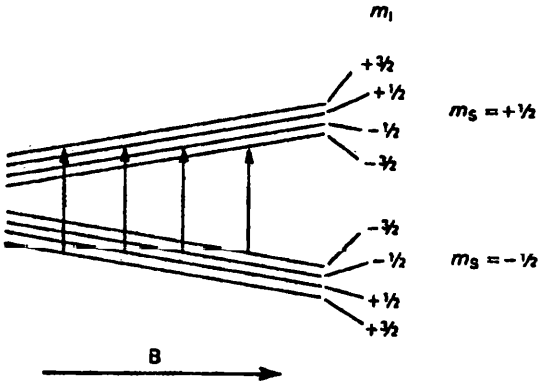

Figure A6.3 Hyperfine splitting of the m_s = -1/2 → +1/2 transition due to interaction with a nuclear spin I = 3/2. The four resulting transitions are equally spaced.

The value of the hyperfine coupling constant, A, depends on the amount of interaction which occurs between the unpaired electron and the nucleus. There are three major factors which control the magnitude of A: Fermi-contact term, spin-polarization exchange effects, and the coupling between the magnetic moments of the nucleus and the unpaired electrons. The last factor depends not only on the distance between the two magnets but also on their relative orientations. The orientation of the nuclear spin is governed by the applied field, while that of the unpaired electron depends on which orbital it occupies and on the orientation of the molecule relative to the applied field. The effect is therefore anisotropic; there are two (or three) principal values, $A_{//}$ and $A_{\perp}$ (or A_z, A_y, and A_x).

The observed A-value is the sum of all these contributions, and its magnitude depends on the relative magnitudes and signs of the various components:

$$A_{obs} = A_{iso} + A_{aniso}$$

Where A_{iso} is the sum of the Fermi-contact and polarization terms, and A_{aniso} is the relevant anisotropic term for the particular orientation concerned. If the system is anisotropic, the coupling constant will obviously vary with the orientation of the molecule. Thus, for a single crystal, A will change with orientation, just like g, with extreme values $A_{//}$ and $A_{\perp}$ For powders and frozen solutions all orientations are possible, but the principal A-values will be associated with the corresponding g-value. Thus, for an axial system, the $g_{//}$ line will appear to be split into $2I + 1$ components separated by $A_{//}$, and $g_{\perp}$ line will be similarly split with separation $A_{\perp}$. The full structure of the spectrum may not be resolved; sometimes all that can be seen is a broadening of the lines. For solutions, the anisotropic effects are averaged to a zero by the rapid tumbling of the molecules, and only A_{iso} remains. It is therefore follows that

$$A_{iso} = (A_{//} + 2\,A_{\perp})/3.$$

References

1.R. V. Parish, *NMR, NQR, EPR, and MÖSSBAUER Spectroscopy in Inorganic Chemistry*, Horwood, Chichester, 1990.

2. P. W. Atkins, *Physical Chemistry, 6th ed., Oxford University Press*, Oxford, 1998